# CONTROLLABLE ADHESION IN A BIO-INSPIRED FILM-TERMINATED FIBRILLAR SURFACE

A Dissertation

Presented to the Faculty of the Graduate School

of Cornell University

In Partial Fulfillment of the Requirements for the Degree of

Doctor of Philosophy

by

Nichole Kristina Nadermann

August 2012

# CONTROLLABLE ADHESION IN A BIO-INSPIRED FILM-TERMINATED FIBRILLAR SURFACE

Nichole Kristina Nadermann, Ph. D.

Cornell University 2012

In this dissertation we present work on the development, characterization, and analysis of an easy-to-fabricate, reusable bioinspired switchable adhesive that consists of a film-terminated fibrillar layer atop a substrate. We use a dynamic rod model and stability analysis to define and analyze the buckling of a fibril subjected to a prescribed shear displacement and a constant normal compressive force. Following this analysis, we present work on the switchable adhesive: a film-terminated fibrillar interface with two metastable states. In the first state, a thin film spanning the fibrillar surface results in strongly enhanced adhesion due to crack-trapping. In the second state, the thin film collapses onto the substrate between fibrils and resembles a rough surface. We perform indentation experiments (pull-off and adhesion hysteresis), which demonstrate differences in the adhesive response of the two states. We show that the adhesive state has a pull-off load up to 70 times higher than the non-adhesive state and has up to 20 times larger adhesion hysteresis. Friction experiments show that in the collapsed state there is no static friction peak and that even in sliding friction, which is not enhanced for the adhesive state over the control samples (flat, unstructured PDMS), the collapsed state exhibits much lower sliding friction forces. We determine the pressure-to-collapse the thin film to switch from the adhesive to the non-adhesive state using hydrostatic pressure experiments. Finally, we perform both linear plate and

von Kärman plate analyses on the thin film as it deforms under an applied pressure to gain insight into both bistability and the pressure required to collapse the thin film and in doing so, turn off the adhesion. We find that the von Kärman plate theory more accurately captures the pressure required to initiate collapse of the thin film onto the substrate, most likely because of the large deflections taking place during collapse. To account for pressurization that occurs in our sealed samples during hydrostatic pressure experiments, we model the rate dependence in the hydrostatic pressure experiments. Pressurization and diffusion of gas through the thin film reduces the dependence on interfibrillar spacing.

# BIOGRAPHICAL SKETCH

Nichole Nadermann was born in Alexandria, Virginia on December 6, 1984. After completing high school in Fitchburg, Massachusetts, she studied at Syracuse University and graduated with a Bachelor of Science degree in Aerospace Engineering in May 2007. In September 2007 she enrolled in the graduate school of Mechanical and Aerospace Engineering at Cornell University, and defended her Ph.D. dissertation on June 12, 2012.

To my family and friends for their support and love

# ACKNOWLEDGMENTS

First of all, I would like to thank my advisers, Professor Chung-Yuen Hui and Professor Anand Jagota, for not only providing me with guidance and support during my dissertation work, but also for sharing with me their wisdom, curiosity, and appreciation for what they do. Additionally, seeing them work on and being a part of various collaborations across great distances was a wonderful new experience. Having them as advisers was an opportunity greater than any I could have hoped for and they will continue to be a source of inspiration and motivation for me.

I would also like to thank Professor Subrata Mukherjee and Professor Delphine Gourdon for serving on my special committee. Professor Mukherjee's role as an engaged and insightful teacher and a caring mentor during my graduate work will remain a bright area in my memories. Also, I greatly appreciate my discussions with Professor Gourdon over the course of my time at Cornell as she always brought with her a great deal of curiosity and insight.

In addition to my committee, I have been fortunate to work within a great research group and with many wonderful scientists, including Professor Sachin Goyal, Professor Rong Long, Dr. Shilpi Vajpayee, and Dr. Ajeet Kumar. Thanks are also due to my fellow group members, Jing Ning, Congrui Jin, Abhishek Srivastava, and Xinzeng Feng.

I would like to take this opportunity to thank my family and friends. I thank my father, David, for the curiosity he fostered in me and my mother, Maria, for the drive she strived to instill in me. To my siblings, Michelle, David, and Andrew: we have been through so much together and the future is looking ever brighter. I would not be here if it were not for your love. To my friends, Casy, Chris, Jim, Jon, Marian,

Shannon, and more, I thank you from the bottom of my heart for how much you have added to my life.

Lastly, I would like to acknowledge several sources of financial support during my five years at Cornell. I am grateful to the Sibley School of Mechanical and Aerospace Engineering for providing me with a fellowship during my first year of study as well as a year of funding through a teaching assistantship. Also, this journey has been greatly facilitated by means of a fellowship from the National Science Foundation Graduate Research Fellowship Program.

TABLE OF CONTENTS

LIST OF FIGURES

# CHAPTER 1

# INTRODUCTION

In nature, fibrillar structures are found on the contact surfaces of many lizards and insects, conferring several remarkable properties, such as the ability to repeatedly adhere to a variety of surfaces and to self-clean [1][2][3][4]. For example, the hierarchical design features on gecko feet allow the animal to move with speeds of over 1 m/s, switching between adhesive and non-adhesive states rapidly and repeatedly.

A recent paper by [5] reviews different mechanisms observed in contacting surfaces in nature as well as many of the derived biomimetics. The first problem, shown in Chapter 2, studies a particular aspect of the gecko adhesive system: the stability of an initially straight elastic fibril clamped at one end, while the other end is subjected to a constant normal compressive force and a prescribed shear displacement. We found that the buckling load of a sheared fibril is always less than the Euler buckling load. Should the end of the fibril lose contact, the buckling load can be considerably less. This study shows that, for microfibrillar arrays, the static friction decreases as the normal compressive load increases and that, in some cases, the friction force can actually become negative.

Inspired by nature's surfaces, several groups have designed and fabricated biomimetics with enhanced properties [6]-[13], using soft, dry adhesives using materials such as poly(dimethylsiloxane) (PDMS). While single level structures such as fibrils with flat ends have generally failed to achieve significant enhancement [14],

two- or multi-level structures have been shown to significantly improve adhesion over that of a flat, unstructured control [6][7][12][13][14].

Scanning electron micrographs (SEM) of the film-terminated fibrillar adhesive (FTFA) studied in Chapters 3 and 4 are shown in Figure 1.1(a) along with relevant parameters. The FTFA consists of a layer of fibrils atop a thick substrate and terminated by a thin-film. Adhesion enhancement in this architecture is obtained by means of a crack-trapping mechanism as there is a spatial variation in energy available to drive the contact edge (for a monotonically changing remote load). As the sample is separating from another surface, the variation of available energy causes the contact edge to propagate unstably, requiring a larger load than is necessary in a flat surface. This structure, in addition to enhancing adhesion, avoids lateral collapse and buckling of fibrils by means of the terminal thin-film [9][14].

In recent years, interest has arisen in exploiting other properties observed in nature, including controllable adhesion, self-cleaning, and directional adhesion. Controllable adhesion has been of particular interest because of its practical uses in applications such as wall-climbing robots [15], micromanipulators [16], MEMS switching [17]. Several different approaches have been taken to produce gecko-inspired adhesives with controllable adhesion. In [18] light-sensitive photoresist was embedded in microchannels to allow samples to “memorize” shapes imposed on them.

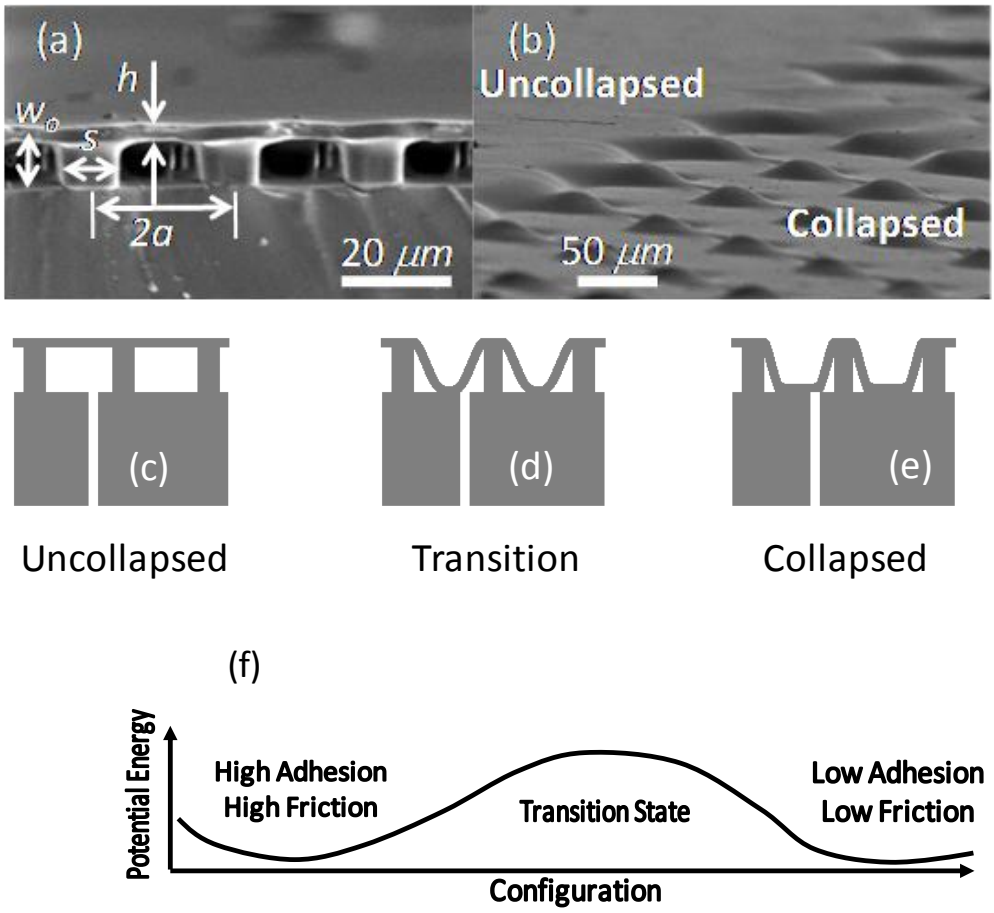


**Figure 1.1 Film-terminated fibrillar surfaces (FTFA) can be bistable. (a) A typical structure in its as-processed state (described on page 85). (b) A partially collapsed state in which much of the terminal film is adhered onto the lower surface (below the bumps are the fibrillar posts). (c) Side-view schematic diagram of (a). (d) Transition state in which potential energy has increased (e) adhesion causes collapse of the terminal film onto the lower surface, and (f) Schematic plot of potential energy versus configuration of the terminal film, depicting bistability.**

Some groups have controlled adhesion with samples that have a lower adhesion along a single axis, either by angled fiber tips or offset fibril caps [20]. In [21], a phase-change material was used in the backing of the adhesive structure that allowed variable stiffness of the substrate. Some other active methods include magnetic manipulation of cantilever structures [22], shape-memory polymers that deform and restore fibers to a default adhesive condition [23], thermally responsive polymers that change both surface energy and mechanical properties [24], and polymer nanofibrillar structures that are shape tunable by means of electron beam radiation [25]. In [26] and [27], PDMS sheets were pre-strained to introduce wrinkling into surfaces that can be controlled mechanically to modulate the adhesion. In [28], fibril buckling was utilized to switch a fibrillar layer from an adhesive state to a non-adhesive state.

While the FTFA had exhibited enhanced adhesion and friction, a question was whether the FTFA could exhibit controllable adhesion and self-cleaning properties. As the adhesion enhancement mechanism for the FTFA is unlike other biomimetics, the methods used to control the adhesion would not be applicable. In Chapter 3, we show that for certain architectural parameters such as interfibrillar spacing, fibril length, and film thickness, the FTFA had a second stable state exhibiting much lower adhesion (see Figure 1.1(b)). As mentioned earlier, the first state, in which the film lies on top of the fibrillar layer, enhanced adhesion and static friction compared to an unstructured flat control. In the second state, the film collapses onto the substrate between fibrils and is held up (away from the substrate) at the fibrils, resulting in a surface with a periodic array of bumps and a much reduced adhesion. Surfaces with this second stable state are referred to as bistable. Pull-off forces, as a measure of

adhesion, were reported and a simple model where the film is modeled as a linear plate was used to analyze the switching mechanism and bistability.

In CHAPTER 4, we characterize the adhesion hysteresis and friction response of the bistable FTFA. We also experimentally determine the required pressure to collapse the thin film in order to switch from the adhesive to the non-adhesive state. Finally, to gain insight into the switching mechanism and bistability, we present a more representative, large deflection, adhesive contact mechanics model of the thin film collapsing onto the substrate.

In the final chapter, we present a summary of the work as well as a discussion of avenues for future work.

# CHAPTER 2

# BUCKLING OF SHEARED AND COMPRESSED MICROFIBRILS[1]

## *2.1 Introduction*

Many small animals and insects use fine hairs on their feet to climb and to stick to surfaces. Inspired by these micro- and nano-structures, many research groups have fabricated synthetic mimics using various polymers or carbon nanotubes to create arrays of micro-fibrils. Typically, fibrils in these arrays are terminated with either a thin film or a spatula to enhance contact and adhesion [6][12][13][23][30]-[33]. These fibrils are part of a backing layer that is made up of the same material, typically a soft elastomer such as PDMS or polyurethane. These biologically inspired surfaces have adhesion considerably greater than that of a flat surface of the same material [14]. More recently, the friction behavior of these micro-fibril arrays has been investigated by different research groups, e.g., [33]-[43]. In this chapter, we focus on synthetic bio-inspired surfaces instead of the fibrillar structures seen in small animals such as geckos. Natural systems are more complex (e.g. fibrils have natural curvatures and exhibit directional adhesion and friction properties). Readers interested in these systems should refer to [44] and [45] and the references therein.

Figure 2.1 shows the schematics of a typical experiment to measure static and sliding friction. A hard and smooth surface, such as the surface of a spherical glass indenter, is brought into contact with the surface of the micro-fibril array by the application of a normal compressive force. In a typical friction test, this compressive

[1] Nadermann, N., Kumar, A., Goyal, S. and Hui, C.-Y., J. R. Soc. Interface, 2010

force is *kept constant* as a shear displacement is applied to move the indenter horizontally.

A difficulty with interpreting experimental results is that fibrils tend to buckle and collapse during experiments. While buckling increases compliance, it reduces adhesion by breaking contact between fibril ends and the indenter [46]. As a result, fibril buckling is usually detrimental to adhesion, as demonstrated by the experiments in [47]. In some cases, collapsed fibrils can lead to greater contact and can increase adhesion and friction; see for example [51].

To avoid buckling of fibrils, many shear experiments are carried out with a fixed normal indenter displacement [35][44]. These experiments show very high "static" friction (friction between two objects that are not moving relative to each other). Typically, in these experiments, a very small compressive force is applied to bring the fibrils into good contact with the indenter, and in contrast to the experimental procedure described earlier, then the fibrils are sheared *keeping the indenter's normal displacement fixed*. As a result, the longitudinal force along the fibril changes from compression to tension. In these experiments, the normal force acting on the fibril array changes during shear. These behaviors are quite different from a friction test where the normal force is maintained to be constant throughout; in this case, common sense suggests that buckling of fibrils will play an important role in the static friction behavior of these arrays. For example, the experiments of [40] clearly show initial buckling of fibrils when the indenter is displaced laterally at fixed normal load. It is interesting to note that this difference between normal displacement controlled and

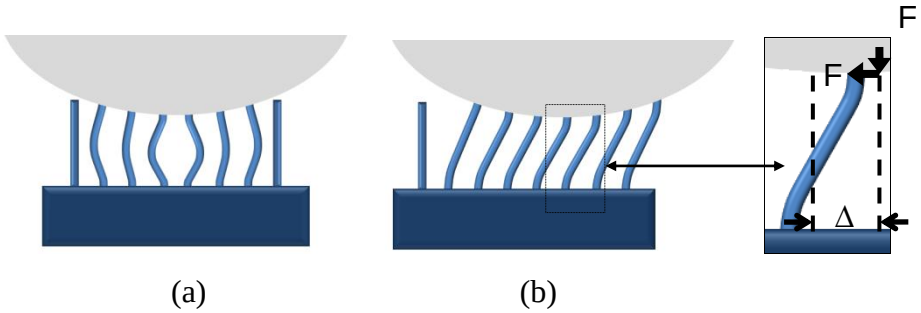


**Figure 2.1. Schematic of a typical indentation and friction experiment. (*a*) A rigid, smooth, spherical indenter is brought into contact with a microfibril array. The compressive force is sufficiently large to cause fibrils in the contact zone to buckle. (*b*) A smaller compressive force is applied to the indenter, which is sheared to the right, causing the fibrils attached to the indenter to shear. For a sufficiently large compressive force, the shear force at the ends of a fibril acts in a direction opposite to the imposed shear displacement.**

normal force controlled friction test is much less significant for typical structural materials where the surfaces are non-fibrillar. This motivates us to analyze fibril buckling as a step towards developing contact and friction models for bio-inspired fibrillar structures.

Intuitively, it is easy to understand why fibrils tend to collapse in shear experiments even though the compressive force is below the buckling load - a sheared fibril bends readily. However, it is non-trivial to calculate the deflection of a buckled fiber and to determine how the buckling load is affected by shear. Since classical buckling theory deals with buckling about an *initially* straight state (straight fibril in our case), a question arises as to how one defines the buckling load of a sheared fibril. This question will be addressed both numerically and theoretically in this work.

Fibrils under combined normal and shear loads can exhibit very counter-intuitive behavior. In [40], it was observed that during a shearing test, the fibrils shear in the direction *opposite* to the shearing force, as shown schematically in the inset in Figure 2.1(b). Note that this behavior occurs initially during the test. We will demonstrate that this counter-intuitive behavior can occur under low applied compressive loads in systems with weak adhesion.

In our previous works [40][48], we have successfully used a nonlinear rod theory where the rod can stretch and bend (but cannot shear) to study deformation of typical fibrils in an array subjected to shear and normal loads. Nonlinear rod theory is also required to study the post-buckling behavior. As is well known, the governing equations for *static* equilibria of a nonlinear rod can have many solutions corresponding to the same loading and boundary conditions. These equilibrium

solutions have different deformed shapes which correspond to different energy states, many of which are stable. A difficulty with the static equilibria calculations is that it is not easy to identify which one of these stable states the rod will converge to. A simple way to circumvent this difficulty is to use a dynamic rod model to compute the deformation of a fibril. In this work, both approaches are used.

The plan of this chapter is as follows. The dynamic rod model is briefly summarized in Section 2.2. The numerical results and the results of the stability analysis are given in Section 2.3. In Section 2.4, we discuss and summarize our results.

### *2.2 Dynamic Rod Model*

The undeformed rod is assumed to be straight and the arc length coordinate of a material point on the centerline of the undeformed rod is specified by *s* (see Figure 2.2). The position vector of the material point *s* after deformation (at time *t*) is denoted $\boldsymbol{r}(s,t)$. A local coordinate system with orthornormal basis vectors $\{\hat{a}_i\}$ is attached at each cross-section, with $\hat{\boldsymbol{a}}_3$ aligned with the centerline tangent, while the other two vectors are aligned with the principal flexure axes. This body-fixed frame describes the orientation of a cross-section with respect to the inertial frame, $\{\hat{\boldsymbol{e}}_i\}$. The dynamic state of a rod's cross-section is represented by four field variables: linear velocity$(\boldsymbol{v})$, angular velocity$(\boldsymbol{\omega})$, curvature$(\boldsymbol{\kappa})$, and force$(\boldsymbol{f})$, defined along the rod's centerline. All field variables are functions of both *s* and *t*. The angular velocity $\boldsymbol{\omega}$ of a cross-section is defined as rotation of body-fixed frame $\{\hat{a}_i\}$ per unit time relative to the

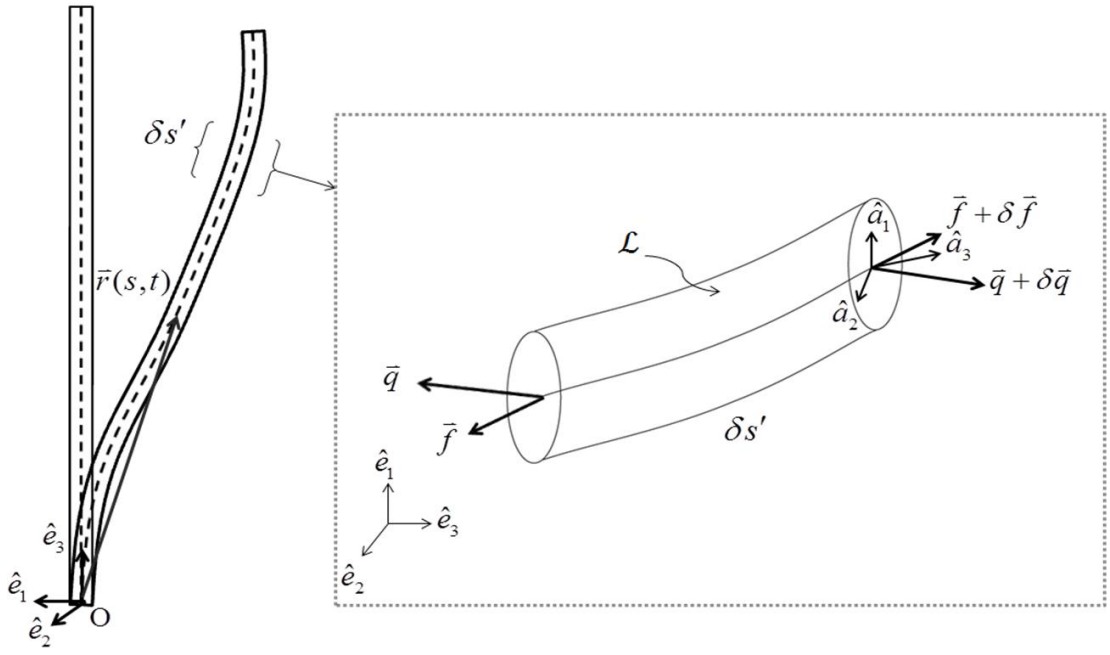


**Figure 2.2. Undeformed and deformed fibril in the inertial reference frame. The insert shows a free body diagram of an infinitesimal element, $\delta s'$ .**

inertial frame $\{\hat{\boldsymbol{e}}_i\}$, i.e.

$$\left(\frac{\partial \hat{\boldsymbol{a}}_i}{\partial t}\right)_{\{\hat{\boldsymbol{e}}_i\}} = \boldsymbol{\omega} \times \hat{\boldsymbol{a}}_i \tag{2.1}$$

where the subscript $\{\hat{\boldsymbol{e}}_i\}$ specifies that the derivative is taken relative to the inertial frame. Similarly, the curvature vector $\vec{\kappa}$ is the rotation of the body-fixed frame per unit arc length relative to the inertial frame,

$$\left(\frac{\partial \hat{\boldsymbol{a}}_i}{\partial s}\right)_{\{\hat{\boldsymbol{e}}_i\}} = \boldsymbol{\kappa} \times \hat{\boldsymbol{a}}_i \tag{2.2}$$

The internal moment $\vec{q}$ is related to the curvature by a constitutive law for bending. For this work, the initial rod curvature is zero and we use the standard linear relation:

$$\boldsymbol{q}(s,t) = \boldsymbol{B}\boldsymbol{\kappa}(s,t) \tag{2.3}$$

Since we have chosen $\{\hat{\boldsymbol{a}}_i\}$ to coincide with the principal torsion-flexure axes of a cross-section, the torsion-flexure stiffness tensor $\boldsymbol{B}$ is diagonal with respect to the body-fixed frame.

Extensibility of the centerline is added to the field equations by means of a kinematic relationship between $\delta s$, the length of an infinitesimal undeformed material element and $\delta s'$, the same element after extension as $\delta s' = \lambda\, \delta s$, where $\lambda$ represents the longitudinal stretch ratio. A nonlinear constitutive model is used to relate $\lambda$ to the

longitudinal force $f_3$ by assuming that the material is neo-Hookean. Under uniaxial tension, the engineering stress, $\sigma$ and the stretch ratio $\lambda$ satisfies

$$\sigma_{33} = \frac{E}{3}\left(\lambda - \frac{1}{\lambda^2}\right) \tag{2.4}$$

It can be shown that there is only one positive real root for $\lambda$ in (2.4). The longitudinal force $f_3$ is thus given by:

$$f_3 = \frac{EA_o}{3}\left(\lambda - \frac{1}{\lambda^2}\right) \tag{2.5}$$

where $A_o$ is the undeformed cross-sectional area of a fibril.

Vector quantities such as $\boldsymbol{f}$ can be expressed in terms of their components once we fix the basis. In the following, quantities such as $\vec{f}, \vec{v}, \vec{q}, \vec{\omega}, \vec{\kappa}$ are 3-tuples consisting of the three components of these vectors with respect to the body fixed frame $\{\hat{\boldsymbol{a}}_i\}$. In the body-fixed reference frame, the linear momentum and the angular momentum balance equations for an extensible rod are [49]:

$$\frac{\partial \vec{f}}{\partial s} + \vec{\kappa} \times \vec{f} = m\left(\frac{\partial \vec{v}}{\partial t} + \vec{\omega} \times \vec{v}\right) \tag{2.6}$$

$$\frac{\partial \vec{q}}{\partial s} + \vec{\kappa} \times \vec{q} = \boldsymbol{I}\frac{\partial \vec{\omega}}{\partial t} + \vec{\omega} \times \boldsymbol{I}\vec{\omega} + \lambda \vec{f} \times \vec{a}_3 \tag{2.7}$$

where $\vec{a}_3 = (0,0,1)$. In (2.6) and (2.7), $m$ is the mass per unit arc length and $\boldsymbol{I}$ is the mass moment of inertia matrix per unit arc length with respect to the body fixed frame.

Additionally, we have the following equation enforcing unshearability, i.e., line elements perpendicular to the centerline remain so even when the rod is deformed:

$$\frac{\partial \vec{v}}{\partial s} + \vec{\kappa} \times \vec{v} = \vec{a}_3 \frac{\partial \lambda}{\partial t} + \lambda \vec{\omega} \times \vec{a}_3 \tag{2.8}$$

and a compatibility condition between $\vec{\kappa}$ and $\vec{\omega}$ that enforces continuity of the body-fixed reference frame $\{\hat{a}_i\}$ along the arc length coordinate *s* and time *t*, i.e.,

$$\frac{\partial \vec{\omega}}{\partial s} + \vec{\kappa} \times \vec{\omega} = \frac{\partial \vec{\kappa}}{\partial t} \tag{2.9}$$

The deformation of the fibrillar array while undergoing indentation and friction tests is assumed to be planar, i.e., independent of the out-of-plane coordinate, $\hat{e}_2$. This is consistent with the loading conditions in shearing and indentation experiments. As a result of this simplification, $f_1, f_3, v_1, v_3, \omega_2, \kappa_2$ are the only non-zero physical quantities. Thus the angular moment balance reduces to a scalar equation and the only relevant element in the matrix $\boldsymbol{I}$ is $I_2$, which we denote simply as *I*. Furthermore, since in our case there is no rotation about the $\hat{a}_1$ and $\hat{a}_3$ axes, the only element of $\boldsymbol{B}$ that comes into play is the bending stiffness *EJ* about the principal flexure axis along $\hat{a}_2$. Here *E* is the small strain Young's modulus of the rod and *J* is the second moment of area. To damp out oscillations of elastic waves, we include the term $hv_i$ in the linear momentum balance equations. Here, *h* is the damping coefficient. The following six scalar equations survive from their three-dimensional, vector counterparts in (2.6) through (2.9).

$$\frac{\partial f_1}{\partial s} + \kappa_2 f_3 = m\left(\frac{\partial v_1}{\partial t} + \omega_2 v_3\right) + h v_1 \tag{2.10}$$

$$\frac{df_3}{ds} - \kappa_2 f_1 = m\left(\frac{dv_3}{dt} - \omega_2 v_1\right) + h v_3 \tag{2.11}$$

$$I\frac{\partial \omega_2}{\partial t} - \lambda f_1 = \frac{\partial q_2}{\partial s} \tag{2.12}$$

$$\frac{\partial v_1}{\partial s} + \kappa_2 v_3 = \lambda \omega_2 \tag{2.13}$$

$$\frac{\partial v_3}{\partial s} = \kappa_2 v_1 + \frac{\partial \lambda}{\partial t} \tag{2.14}$$

$$\frac{\partial \omega_2}{\partial s} = \frac{\partial \kappa_2}{\partial t} \tag{2.15}$$

We define the following normalized variables:

$$s = LS,\ t = \tau T,\ q_2 = \frac{EJ}{L}Q_2,\ f_i = \frac{EJ}{L^2}F_i, \tag{2.16}$$

$$\kappa_2 = \frac{K_2}{L},\ v_i = \frac{L}{\tau}V_i,\ \omega_2 = \frac{1}{\tau}\Omega_2 \quad i = 1,3$$

where $L$ is the length of the undeformed rod. Note that time is normalized by $\tau \equiv \sqrt{mL^4 / EJ}$, which is proportional to the time for a flexure wave to traverse the length of a rod. Also, with this normalization, the Euler buckling load for a non-stretchable clamped-clamped rod is $-4\pi^2$. Similarly, the Euler buckling load for a non-stretchable pinned-pinned rod is $-\pi^2$.

The normalized governing equations for an extensible rod are accordingly:

$$\frac{\partial F_1}{\partial S} + K_2 F_3 = \frac{\partial V_1}{\partial T} + H V_1 + \Omega_2 V_3 \tag{2.17}$$

$$\frac{\partial F_3}{\partial S} - K_2 F_1 = \frac{\partial V_3}{\partial T} + H V_3 - \Omega_2 V_1 \tag{2.18}$$

$$\alpha^2 \frac{\partial \Omega_2}{\partial T} - \lambda F_1 = \frac{\partial Q_2}{\partial S} \tag{2.19}$$

$$\frac{\partial V_1}{\partial S} + K_2 V_3 = \lambda \Omega_2 \tag{2.20}$$

$$\frac{\partial V_3}{\partial S} = K_2 V_1 + \frac{\partial \lambda}{\partial T} \tag{2.21}$$

$$\frac{\partial \Omega_2}{\partial S} = \frac{\partial K_2}{\partial T} \tag{2.22}$$

$$F_3 = \frac{A_o L^2}{3J}\left(\lambda - \frac{1}{\lambda^2}\right) \tag{2.23}$$

Note that these normalized equations are governed by two dimensionless parameters,

$$\alpha = \sqrt{\frac{I}{mL^2}} \quad \text{and} \quad H = \frac{hL^2}{\sqrt{mEJ}} \tag{2.24}$$

where $\alpha$ is the slenderness ratio defined as the ratio of the radius of gyration of the rod to its length and $H$ is the normalized damping coefficient. Since $H$ controls damping of oscillations, the equilibrium solution depends only on $\alpha$.

We employ a typical boundary condition that is encountered in shearing and indentation experiments. Specifically, the end of the fibril ($O$ in Figure 2.2), which is attached to the backing, is assumed clamped, whereas the end that is in contact with the indenter is constrained from rotation but allowed to shear. It is important to note that the last two boundary conditions are satisfied only for fibrils which are well adhered to the indenter. Most investigators use fibrils that have structures at their tips to improve contact and adhesion. For example, [13] and [39] used terminal contact plates, whereas [9] and [43] used a terminal continuous thin film. For these fibrils, it is expected that the aforementioned boundary conditions would be satisfied. However, these boundary conditions will not be met for fibrils with no special structures at their tips. The adhesion of these fibrils is found to be weak and they tend to buckle easily as their tips lose adhesion [46]. We will discuss this further in the discussion section.

To solve the nonlinear partial differential equations (2.17)-(2.23) for the unknowns $K_2$, $\Omega_2$, $F_1$, $F_3$, $V_1$, $V_3$, we use Keller's box method [50] to discretize the

equations in both space and time as well as numerically integrate them. This method has second order accuracy. The resulting nonlinear difference equations are implicit and their solution is required to satisfy the boundary conditions described above (see Figure 2.10 for some details).

### *2.3 Results*

The numerical results presented in this section are valid for fibrils of any dimension as long as they have the same slenderness ratio $\alpha$. To give an idea of typical dimensions, in the samples used by [51], the fibrils have a 10 μm × 10 μm square cross-section. Fibril heights range from 30 to 100 μm. Typical materials used to create these arrays are elastomers such as poly(dimethylsiloxane) (PDMS, Sylgard 184, Dow Corning) and polyurethane which has shear modulus on the order of 1 MPa. Thus, the slenderness ratio of the samples used by [51] is $1.054 \times 10^{-3}$. The numerical results below are obtained using this value.

To analyze the buckling behavior of a fibril subjected to a compressive normal force and a shear displacement at the top end, we prescribe normalized axial force $F_n$ (compressive in nature, negative) and normalized shear displacement $\Delta_s/L$ at the top end. The kinematic boundary conditions are imposed by enforcing zero linear and angular velocities at the bottom end of the fibril. In each case, the desired normalized shear displacement is simulated by prescribing a shear velocity at the top end (as shown in Figure 2.3). Simultaneously, we increase the normalized compressive force $F_n$ from zero to its maximum value using a hyperbolic tangent function. The notations $F_n$ and $F_s$ denote the values of $F_3$ and $F_1$, respectively, at the top end.

How does one define the buckling load of a sheared fibril? A zoom-in view of the variation of the normalized normal tip displacement with the compressive load for six fixed values of normalized shear displacement $\Delta_s/L$ is shown in Figure 2.4. For each $\Delta_s/L$, there is a distinct point at which the slope of the normal tip displacement curve changes abruptly, i.e., a cusp is formed. Figure 2.5 shows the shape of a fibril just before and after this cusp; the number of inflection points in the deformed shape changes from one to two as the cusp is reached.

As is well-known, a cusp is a bifurcation point at which multiple solutions exist; one of these solutions has to satisfy the condition of continuity of slope. In our case, this solution may be unstable. If this is the case, then this bifurcation point corresponds to buckling instability or fibril collapse. The existence of an unstable solution will be demonstrated in the next section. Assuming for now that an unstable solution does exist, we define the compressive force at this cusp point to be the buckling load of a sheared fibril.

We summarize our result in Figure 2.6 where the normalized compressive force at the cusp $F_n^*$ is plotted against the normalized shear displacement at the top end. As expected, $F_n^*$ decreases as the shear displacement at the tip is increased. The result of the dynamics analysis suggests the following quadratic dependence:

$$F_n^* = -0.00182\left(\Delta_s / L\right)^2 + 0.00232\Delta_s / L + 41.275 \qquad (2.1)$$

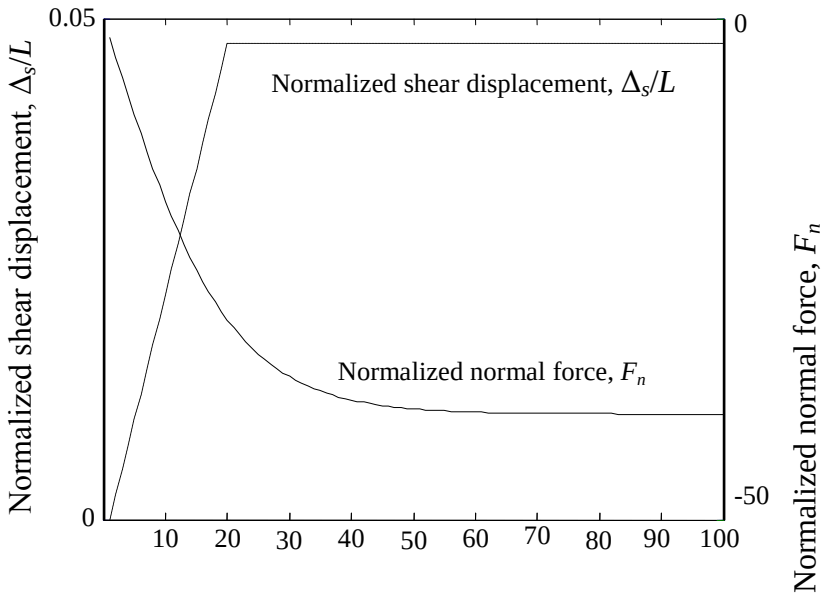


**Figure 2.3 Example of a loading history prescribed at the top end of a fibril in dynamic simulation with a final normalized shear displacement of 0.05 and a normalized (compressive) load of $-4\pi^2$.**

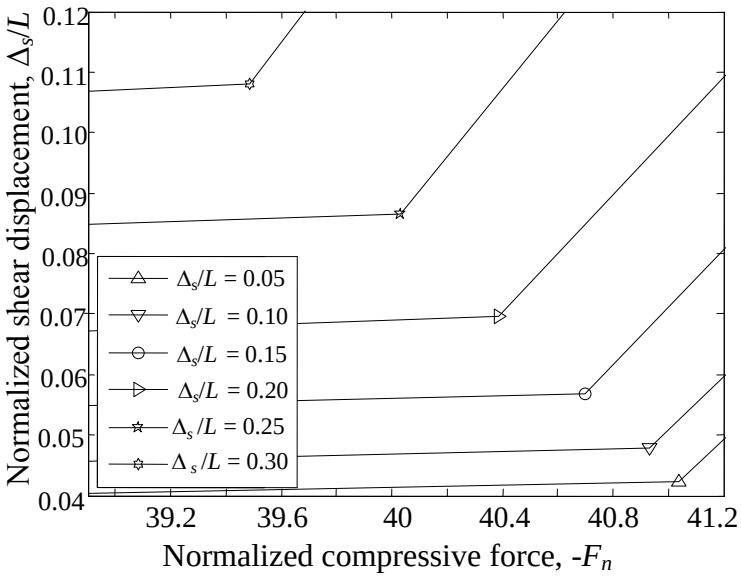


**Figure 2.4 Normalized normal tip displacement, $-\Delta_n/L$, plotted against the compressive load for six different values of $\Delta_s$. For each prescribed shear displacement, there is a cusp at which the slope is discontinuous.**

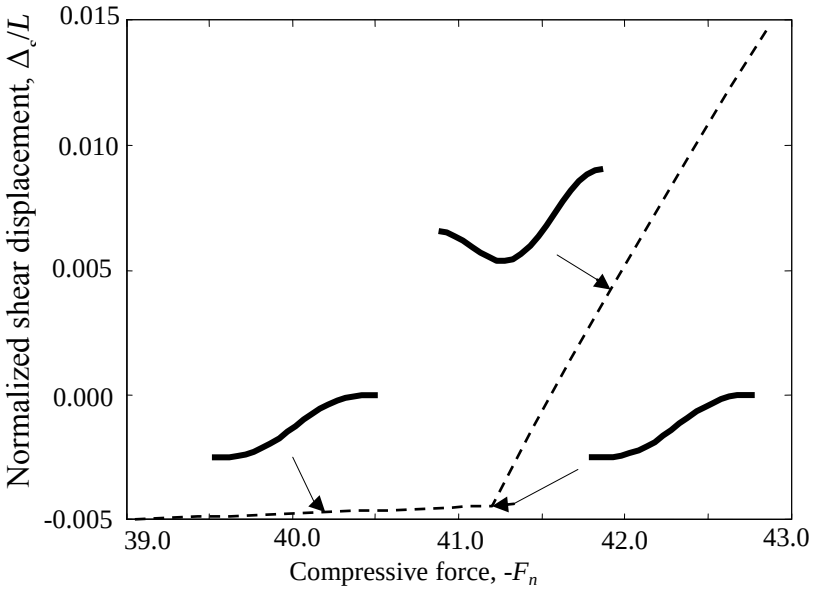


**Figure 2.5 Normal tip displacement (normalized by *L*) as a function of compressive force with a normalized shear tip displacement of 0.05. Note that the number of inflection points in the deformed shape changes from one to two as the cusp is reached.**

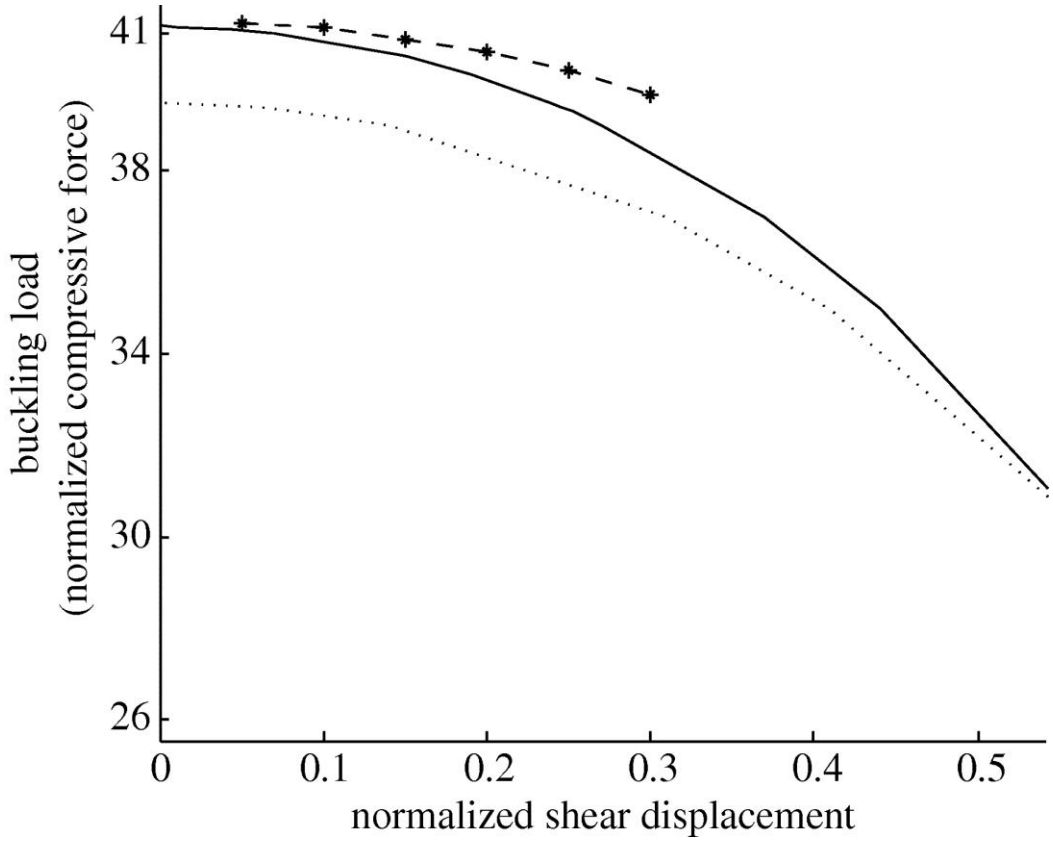


**Figure 2.6 Buckling load as a function of normalized shear displacement at the tip of a fibril for the nonlinear dynamic and stability analysis. Dashed line with asterisks, extensible–dynamic; solid continuous line, extensible–stability; dotted line, inextensible–stability.**

**Stability Analysis**

In the following, we analyze the stability of static equilibrium configurations of the sheared fibril as we vary the compressive load as well as the shear displacement. The stability analysis was performed by co-author Ajeet Kumar in [52]. Recall that the fibril is assumed to be stretchable but unshearable. To analyze the stability of a given configuration, the fibril must be perturbed about the given equilibrium configuration such that the perturbed configuration also satisfies the unshearability constraint. For a stable configuration, all "nearby" and admissible perturbed configurations will have a higher potential energy. Numerical determination of stability, especially in the presence of a point-wise unshearability constraint, is a non-trivial problem and was discussed in detail in the work of [53]. This work also shows that the minimum potential energy method is equivalent to the linearized dynamics stability criterion for conservative problems, as is the case here. Here we use their technique to determine whether a given configuration is stable or not.

**Shear Constraint Violation**

The dependence of shear force on shear displacement is particularly interesting. Figure 2.7 shows two different regimes. For normalized compressive forces less than $\pi^2$, the slope of the normalized shear displacement versus normalized shear force curve is positive. That is, the shear force increases in the same direction as the shear displacement. However, when the normalized compressive force is greater than $\pi^2$, the slope becomes negative, i.e., the shear force is in the *opposite* direction of the

shear displacement! This phenomenon is actually observed by the experiments of [51], as mentioned in Section 2.1.

The fact that the shear force is in the opposite direction of the shear displacement suggests that if a fibril were to overcome the shear constraint at the boundary (recall the fibrils are assumed to be adhered firmly to the rigid indenter), then the fibril would become unstable and collapse at a lower normalized compressive force of $\pi^2$. This loss of boundary constraint is illustrated schematically in Figure 2.8(a), (b) (see also caption for explanation). Physically, this means that sheared fibrils can collapse at much lower compressive loads if they are poorly adhered to the indenter.

Why does this instability occur at $F_n = -\pi^2$? Here we offer a simple physical explanation. Figure 2.8(b) shows that when the shear constraint is removed and the top end of the fibril is allowed to shear without friction, i.e., $F_s = 0$, the resulting structure becomes equivalent to the pinned-pinned configuration as shown in Figure 2.8(c). The normalized buckling load for this case is exactly $-\pi^2$. It is well known that fibrils without an attachment mechanism lose adhesion readily in *normal* indentation tests (no shear displacement applied) when they buckle. It has been shown experimentally and theoretically that buckling of the fibril causes the top end of a fibril which is attached to the indenter to rotate; as a result, it behaves as a pinned support instead of a clamped support when in contact with the indenter [46]. This experimental and theoretical result is consistent with the fact that the shear instability occurs at $F_n = \pi^2 EI / L^2$.

Figure 2.6 plots the results of the dynamics analysis (extensible rod) as well as the stability results based on static analysis for both an extensible and inextensible rod. This figure shows how the buckling load decreases as the fibril is sheared. Also, the buckling load corresponding to an inextensible fibril is lower than that for an extensible fibril. As expected, this difference becomes less pronounced as the normalized compressive load is reduced since the fibril starts to behave more as an inextensible rod. This indicates that extensibility does not affect the buckling load greatly. We mentioned that the dynamics result is slightly above the static result. We believe that the static result is more accurate since numerically it is more straightforward so finer discretization can be used without sacrificing computation time. Figure 2.7 shows the stability/ bifurcation diagram for an inextensible rod. All stable configurations are shown as solid black lines.

As discussed earlier and shown in Figure 2.7, shear force and shear displacement are of the same sign for compressive loads below $\pi^2$. Figure 2.7 also shows that all equilibrium solutions are stable for normalized compressive loads less than 30. This means that the change in sign of the shear force is not related to the onset of buckling for a rod whose tip is constrained against shear displacement. However, if this constraint is violated, the fibril will become unstable as was described in the previous section. By examining the energy landscape of the rods for the normalized compressive loads of 30 and 35, we found the rods lose stability at a critical value of shear displacement. These critical shear forces and displacements correspond to buckling points. The presence of multiple equilibria (bifurcation) is indicated by the

different dotted curves emitting from these bifurcation points. These bifurcated solutions are found to be unstable indicating the absence of a stable equilibrium configuration. Physically, this corresponds to collapse of fibrils in this regime which also confirms that the cusp observed in our dynamic simulation corresponds to the same bifurcation point.

### *2.4 Discussion and Summary*

Using dynamic rod model and stability analysis, we define and analyze buckling of a fibril that is subjected to prescribed shear displacement and a constant normal compressive force. Our result is summarized in Figure 2.6 which shows how buckling load decreases with prescribed shear displacement. The buckling load is bounded from above by the Euler buckling load of a clamped-clamped rod, $4\pi^2 EI / L^2$. It should be noted that our rod model allows for non-uniform stretching of the centerline of the rod. This feature is included since there are situations where fibril stretching is not negligible, e.g. when a fibril is sheared under a fixed normal displacement (see [35]). However, for the boundary conditions used in this work, extensibility plays a small role in the determination of stability, as shown in Figure 2.6.

What is unexpected is that instability can occur at or above a compressive load of $\pi^2 EI / L^2$ which is the Euler buckling load of a pinned-pinned rod. This load is exactly one fourth of the Euler buckling load of a clamped-clamped rod. Specifically, we found that when a fibril, subjected to a normal compressive load exceeding $\pi^2 EI / L^2$, is displaced laterally, the shear force acting on the fibril will be in the opposite direction as the imposed shear displacement. This has the following

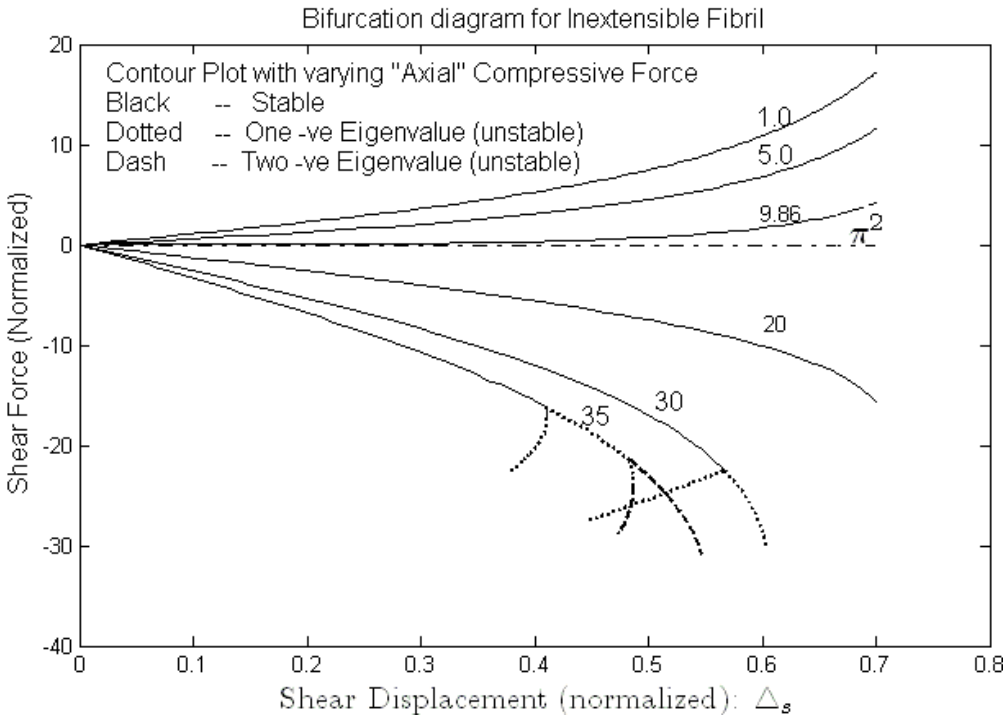


**Figure 2.7. Bifurcation diagram for an inextensible fibril as a function of normalized shear displacement.**

interesting implications. Consider the rigid indenter in Figure 2.1(b) which is perfectly adhered to a set of *m* identical fibrils. Assume the indenter has very large radius of curvature so it is effectively a flat block. If this block is subjected to a normal compressive force greater than $m \times \pi^2 EI / L^2$ (e.g. by adding weights on top of the block), then it is unstable in shear. This means that a fibrillar interface has negative friction coefficient and energy is transferred from the fibrils to the loading device. This prediction is actually observed by [51]. In the initial part of their experiment, they observed buckling of fibrils and that the slope of the shear force versus shear displacement curve under a fixed normal compressive load becomes negative (see Figure 11, [51]).

What happens if the applied normal compressive load is less than $\pi^2 EI / L^2$ ? In this case, the system is stable. However, intuitively, one expects that, for a fixed shear displacement, $\Delta_s$, the shear compliance of a fibril should increase with increasing normal load $F_n$. In other words, the shear force at a fixed $\Delta_s$ should decrease with increasing compression. Figure 2.9 shows this is indeed the case. Note that the compliance of the system is positive as long as $F_n > -\pi^2 EI / L^2$.

The fact that the shear force on a fibril decreases with normal load (for $F_n > -\pi^2 EI / L^2$) suggests that *static friction should also decrease with normal force* as long as the boundary constraints on the fibrils are maintained. It is important to note that static friction is defined in different ways in the literature. In this work,

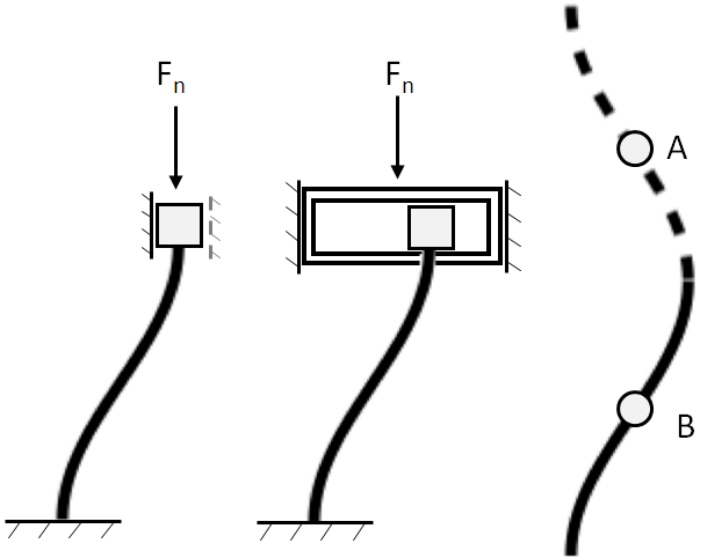


(a) (b) (c)

**Figure 2.8. Schematic (*a*) shows shear constraint on the upper end of the fibril; (*b*) shows an equivalent boundary condition for the critical condition when the shear force becomes zero. The buckling condition for schematic (*b*) is the same as that of the equivalent pinned-pinned rod between two points of inflection A and B as denoted in the schematic (*c*). In experiments, some fibrils have weak shear constraints. Violation of the right side shear constraint (dashed grey) in schematic (*a*) beyond a critical condition leads to dynamic collapse equivalent to that in schematic (*b*) or (*c*).**

static friction corresponds to maximum shear load when the block is subjected to a *fixed normal load*. Since the normal load is fixed as we shear a fibril, the vertical displacement of the fibril end is not constrained. For example, a rigid block resting on a fibrillar interface consisting of a uniform matt of identical fibrils will move vertically down as it is sheared. Note that the maximum shear load may occur after a buckling instability since it is possible that (1) the ends of the fibrils are still well adhered to the indenter, (2) collapsed fibrils can support more shear. Static friction is defined differently in the work of [35] and [44]. In their tests, the vertical displacement of the contactor is fixed during shear after a compressive preload is applied to bring the contactor into contact with the fibrils. In this set up, if the fibrils are well adhered to the contactor, they will be stretched and the normal load will change with shear and actually become tensile (see Figure 3 in [35]). In this case, static friction corresponds to adhesive failure of the fibril ends.

To summarize, assuming that fibrils in the array are identical and the number of fibrils do not change as we shear (e.g. the indenter is flat), our theory predicts the following:

- If the applied compressive $F_n$ on each fibril is less than $\pi^2 EI/L^2$ then static friction should decrease with increasing normal load.

- If the applied compressive $F_n$ on each fibril is greater than $\pi^2 EI/L^2$, then the friction force becomes negative if adhesion is weak resulting in the violation of shear constraint.

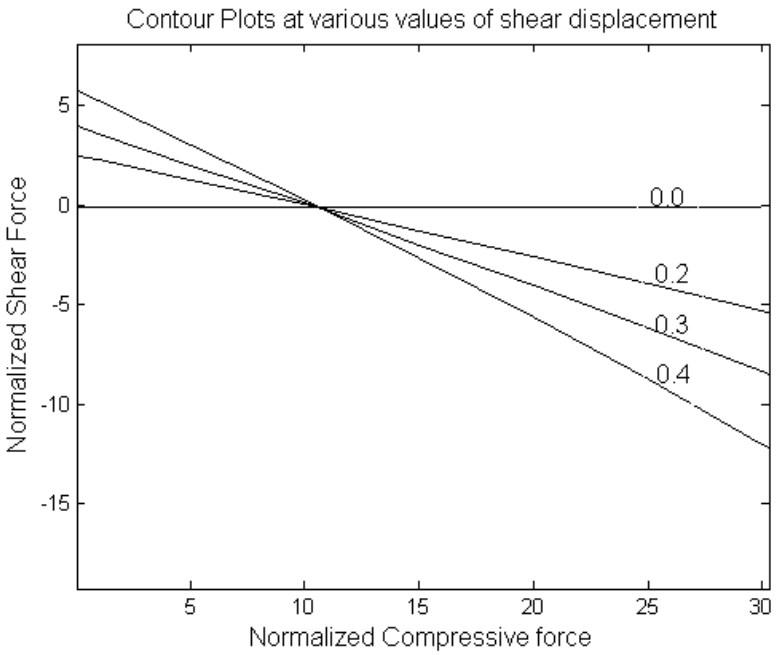


**Figure 2.9 Normalized shear force, $F_s$, versus normalized compressive force, $F_n$, for several normalized shear tip displacements, $\Delta_s$.**

### *2.5 Appendix: Numerical Methods*

Briefly, in Keller's box method [50], a rectangular grid is created along the space and time axis as shown in Figure 2.10 below. We discretize the differential equations by finite difference. For example, a dependent variable *u*, is approximated by its value at the midpoint of the box by:

$$u_{j-1/2}^{n-1/2} = \frac{1}{4}\left(u_j^n + u_j^{n-1} + u_{j-1}^n + u_{j-1}^{n-1}\right) \tag{2.2}$$

where *n* is the time index and *j* is the space index. Also, the partial derivatives of *u* with respect to *s* or *t* are given by:

$$\left(\frac{\partial u}{\partial s}\right)_{j-1/2}^{n-1/2} = \frac{1}{2}\left[\frac{u_j^{n-1} - u_{j-1}^{n-1}}{\Delta s}\right] + \frac{1}{2}\left[\frac{u_j^n - u_{j-1}^n}{\Delta s}\right] \tag{2.3}$$

$$\left(\frac{\partial u}{\partial t}\right)_{j-1/2}^{n-1/2} = \frac{1}{2}\left[\frac{u_{j-1}^n - u_{j-1}^{n-1}}{\Delta t}\right] + \frac{1}{2}\left[\frac{u_j^n - u_j^{n-1}}{\Delta t}\right] \tag{2.4}$$

Thus, a dependent variable and its partial derivatives are evaluated at the midpoint of the box in terms of two known nodal values (the dark circles in Figure 2.10) and two unknown nodal values (the open circles). Boundary conditions are imposed by specifying their nodal values at the boundary nodes. The resulting nonlinear algebraic equations can be solved using Newton's method.

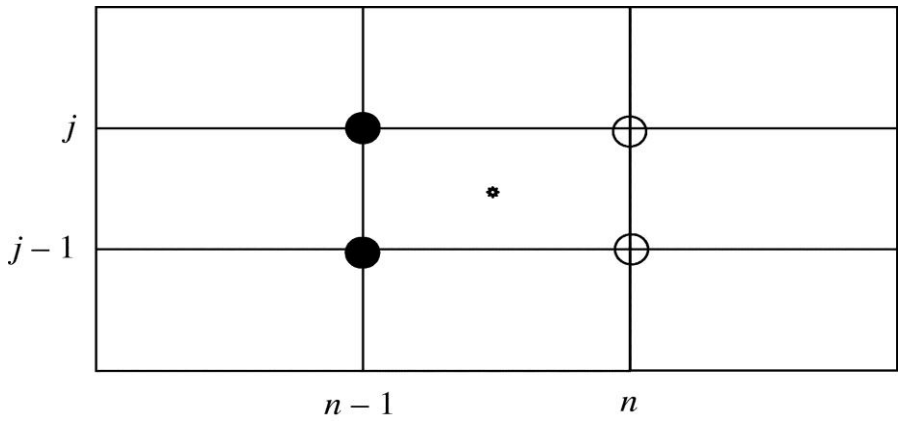


**Figure 2.10 Stencil for Keller Box method**

# CHAPTER 3

# ACTIVE SWITCHING OF ADHESION IN A FILM-TERMINATED FIBRILLAR SURFACE[2]

## *3.1 Introduction*

In this chapter, we show that the FTFA can be designed such that it has two metastable states. In the first state, the terminal film is stretched flat and held up by fibrils (see Figure 1.1(a)). The uncollapsed structure is inspired by adhesion enhancing structures seen in nature. The essential features borrowed from nature include the seta-like fibrils, which provide compliance, and a terminal thin film. In the second state, the terminal film adheres to the substrate between fibrils (Figure 1.1(b)) resulting in an overall bumpy surface and mimicking surfaces that lack adhesion due to the increased roughness and accompanying reduction in area. Previously, we have shown that the uncollapsed state has significantly enhanced adhesion compared to a flat control sample [14]. The collapsed state, on the other hand, resembles a rough surface (Figure 1.1(b)) and is expected to have low adhesion.

With a proper choice of architectural parameters, such as fibril height and spacing, and film thickness, this structure can remain indefinitely in either of two states: with uncollapsed and collapsed terminal film. In addition, it can be switched repeatedly between these two states by a simple external stimulus such as pressure, allowing its adhesion to be switched between "on" and "off".

[2] N. Nadermann, J. Ning, A.Jagota, C.-Y. Hui, *Active switching* of adhesion in a film-terminated fibrillar structure. Langmuir. 2010 Oct 5;26(19):15464-71

The remainder of this chapter is organized as follows. In the next section, we provide a description of the fabrication methods used to create the samples we have tested, followed by a description of the experiments to measure adhesion. In the subsequent section, we present a qualitative illustration of bistability and the resulting difference in adhesion between the collapsed and uncollapsed states, followed by results of quantitative measurements of the adhesion in the two states. We then present a simple model to explain how materials and geometrical parameters control bistability and, finally, we conclude with a summary of our findings.

## *3.2 Materials and Methods*

### *3.2.1 Fabrication*

The fabrication method for the structure shown in Figure 1.1(a) has been described elsewhere [14]. Briefly, fibrillar structures were fabricated by the molding of PDMS (Sylgard 184, Dow Corning, 1:10 ratio of cross-linker to prepolymer) using negative image silicon (Si) masters patterned by standard photolithography and deep reactive ion etching (DRIE) techniques. A hydrophobic self-assembled monolayer (SAM) of *n*-hexadecyltrichlorosilane was applied to the wafers to reduce their surface energy, enabling easy subsequent release of the molded PDMS. The liquid polymer precursor was flowed into the holes, cured, and peeled out of the master resulting in an array of PDMS posts (fibrils) on the sample surface. The cross-sectional geometry and spacing of the posts (fibrils) is identical to that of the array of holes on the master, and the post (fibril) height is equal to the depth of the hole. To provide access for the application of pressure to the space under the terminal thin film, which itself was attached in a later step, we molded tapered, polystyrene coated glass rods into the PDMS atop each of

the samples in the silicon mold. The tips of the glass rods range from 30-50 μm in diameter. An illustration of this process is given in Figure 3.1.

To attach the terminal film to the ends of the posts, a polymer precursor (again, PDMS) was first spin-coated on a hydrophobic substrate. Then, the array of posts was placed on the film while the film was still liquid. Bistability depends on several parameters (see theory section for details), one of which is fibril length. We found that to achieve the metastable collapsed state, it is necessary to either use shorter fibrils, thinner films, or larger interfibrillar spacings. However, shorter fibrils were more prone to wicking of the thin film, necessitating the partial pre-curing of the film prior to attaching the substrate and fibrillar layer. The optimal time of pre-curing (in this work, it is done at 40ºC) varies depending on the fibrillar spacing, height, and the thickness of the thin film. Except where noted differently, film thickness was 6 μm and fibrils had a square cross-section 100 $\mu m^2$ in dimension. The thin films were fabricated using a spin speed of 3,000 RPM for 10 minutes. The fibrils are distributed in a square pattern with minimum center-to-center spacings ranging from 20 – 125 μm. We report results for three different fibril lengths, $w_0$ = 10.6, 17.8, and 23.2 μm. For $w_0$ = 10.6 μm, we pre-cured the larger spacings (80 μm, 95 μm, 110 μm, and 125 μm) for 29 minutes and the smaller spacings (20 μm, 35 μm, 50 μm, and 65 μm) for 22 minutes. For $w_0$ = 17.8 μm, we pre-cured the thin film for 14 minutes for the smaller spacings and 17 minutes for the larger spacings. For $w_0$ = 23.2 μm, we pre-cured the thin film for 9 minutes for smaller spacings and 11.5 minutes for larger spacings. After partially pre-curing the thin film and placing the fibrillar samples onto

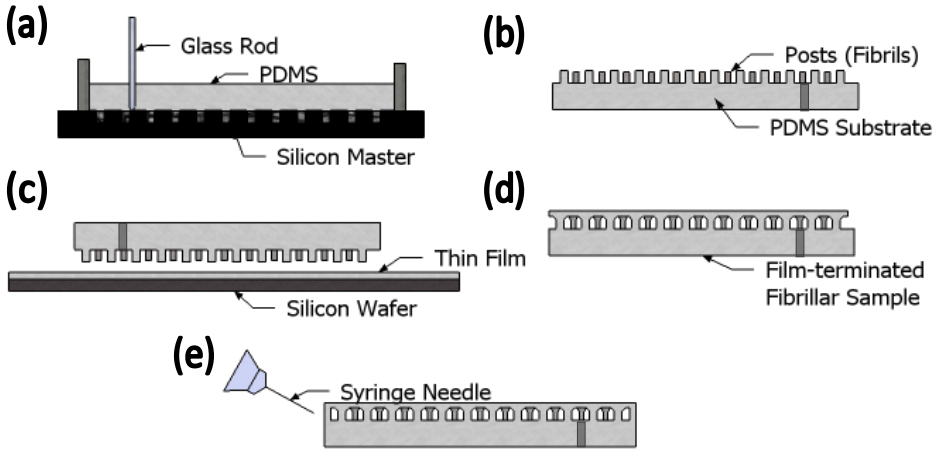


**Figure 3.1. Typical fabrication procedure of a FTFA. (a) First, liquid PDMS is poured into a Si master for molding; a glass rod can be used to provide access to the space under the terminal film. (b) The fibrillar sample is peeled from the Si mold. (c) The fibrillar sample is placed on a Si wafer with liquid PDMS spin-coated on top for cross-linking; the entire sample is cured for 1 hour at 80°C. (d) After removing the fibrillar sample and thin film from the Si wafer, one has a FTFA. (e) In some cases, a syringe needle is used to apply a PDMS seal to the sides of the sample. This allows one to control the internal pressure of the sample via the channel introduced in (a).**

the thin film, the liquid film partially wicked up the fibrils, cross-linked with the fibrillar sample, and was cured for 1 hour at 80ºC. The entire sample was removed manually from the substrate. An image of a typical final fibrillar structure is shown in Figure 1.1(a). For some samples, after removal from the Si wafer, liquid PDMS was applied using a syringe needle to seal the outer edges of the structure, so that the only access to the volume between the thin film and the substrate was the hole previously molded in through the bottom of the substrate in Figure 3.1.

Using microbore tubing (0.03″ diameter) (Cole-Parmer) inserted into the hole created in each sample by the glass rod, we were able to use a syringe pump (Chemyx Inc.) to control the flow of air into the sample. By these means we could collapse the terminal film by removing the air in the sample, thereby reducing the pressure in the cavity under the film. Conversely, to return the sample to the uncollapsed state, we increased the pressure in this cavity by pumping air into the sample. Alternatively, we were able to collapse the sample locally by pressing on the contacting surface with a spherical indenter coated with a silane monolayer or globally by pressing the surface through a nitrile glove. We were able to uncollapse the structure by pressing against the top surface by a slab of PDMS or another fibrillar sample, and peeling it off. Because of the way we collapsed and uncollapsed the specimens, at present the associated critical values of pressures are not known. We fabricated unstructured flat control samples following the same procedure, except that the PDMS film in the first step was cast against a polystyrene coated glass slide.

### *3.2.2 Measurement of adhesion and compliance*

Indentation experiments were performed to measure compliance and adhesion of the samples. A schematic drawing of the set-up is given in Figure 3.2. It consists of a precision vertical stage (Newport MFN25CC) attached to a load train containing a strain gauge type load cell (Transducer Techniques, 10g) in line with the spherical glass indenter with a radius of approximately 4 mm. To reduce interfacial rate effects, a *n*-hexadecyltrichlorosilane monolayer was deposited on the spherical glass indenter. To add the monolayer, the indenter was cleaned in a piranha solution (70% $H_2SO_4$, 30% $H_2O_2$) for 1 hour. Afterwards, it was rinsed with deionized water, dried with flowing $N_2$, and then cleaned with oxygen plasma. A few drops of the silane were placed on a leaf of Whatman 5 filter paper, which was suspended over the indenter for two hours in a sealed chamber. After two hours, the indenter was removed from the chamber and left to cure overnight.

The stage lowered the indenter at a speed of 1 μm/s into contact with the sample, which was supported on the microscope platform. The glass sphere was indented a prescribed 30 μm into the sample and then retracted at the same speed. As this took place, the load cell voltage (for force) and stage displacement were recorded by a computer data acquisition system and the contact area between the indenter and sample was viewed through the microscope. The maximum force supported by the indenter (positive numbers represent compression), the pull-off force, was our measure of adhesion. The computer used for data acquisition also recorded a direct digital streaming video of the corresponding contact evolution. After obtaining the

force-displacement data, we zeroed the force measurement using the first 150 points of data obtained when the indenter was not in contact with the sample.

### *3.3 Results and Discussion*

#### *3.3.1 Qualitative Comparison of Collapsed and Uncollapsed States*

For certain sample parameters (fibril spacing and height), we found that decreasing the pressure in the space between the thin film and the substrate can cause the thin film to collapse around the fibrils. An image of a sample showing this behavior is shown in Figure 1b, where part of the thin film has collapsed, showing distinct bumps, while the rest of the thin film smoothly spans the fibrils. The fact that the two regions can co-exist demonstrates the bistability of this sample. By adjusting the pressure in the space between the thin film and the substrate, we could advance or retreat the collapsed portion of the sample (see Figure 3.3).

Using spherical glass particles ranging 300-400 μm in diameter, we qualitatively tested the adhesive qualities of the uncollapsed and collapsed regions in a bistable sample, as shown in Figure 3.4. This size of the spherical glass particles is in the range of medium coarseness sand [54]. We chose this range for its closeness in size to dirt particles and also because the particles are large enough compared to characteristic length scales of our structure that the collapsed state appears as a bumpy, rough surface. Particles much smaller than the typical length scales of our structure, e.g., those with radii of a few microns, are expected to adhere equally well to both collapsed and uncollapsed samples. For each sample we first collapsed a certain region by applying pressure mechanically from above. Next, we poured glass

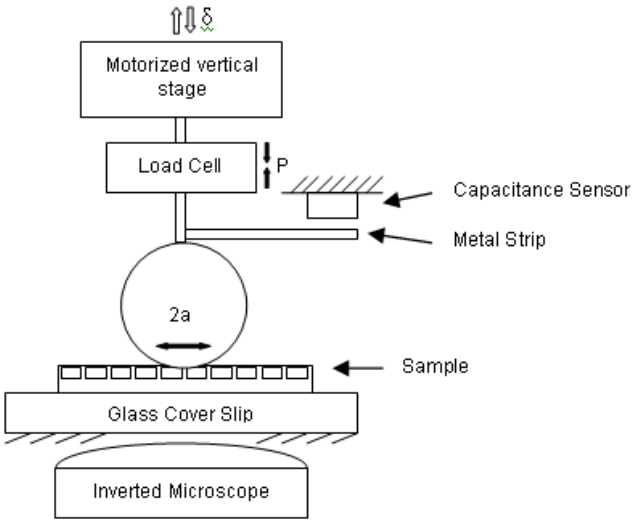


**Figure 3.2 Experimental set-up for the indentation experiments. A spherical indenter is lowered into the sample to a certain depth and then pulled out using a motorized stage. The load on the indenter, *P*, is measured using an in-line load cell, the indenter's vertical displacement, *δ*, is measured using a capacitance sensor, and the contact between the indenter and sample is obtained by recording its image through the inverted optical microscope.**

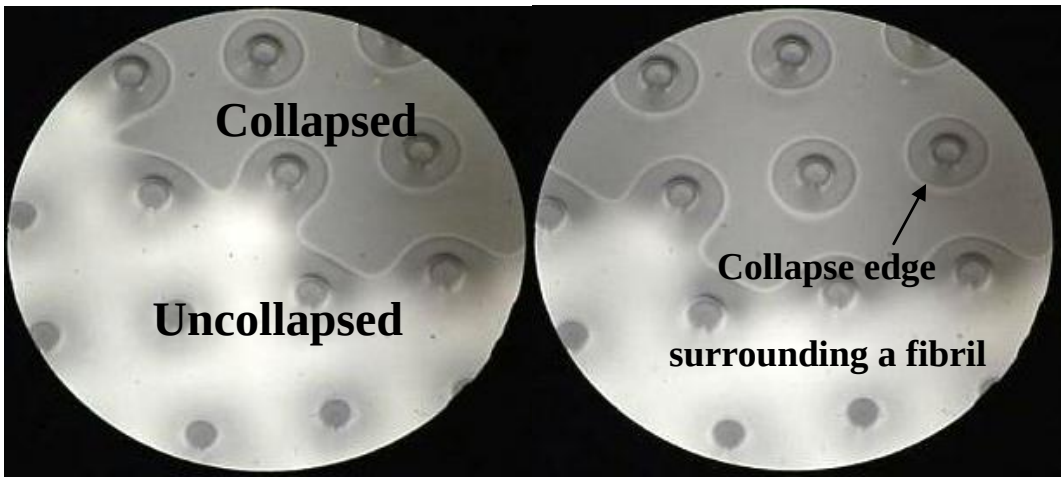


**Figure 3.3 Optical micrographs of collapsed and uncollapsed regions on a sample with 10.6 μm tall fibrils with an interfibrillar spacing of 65 μm. In the upper right parts of both micrographs, one can see the region over which the thin film has collapsed and is in contact with the substrate (the darker region with rings around the fibrils). A decrease in pressure between the left and right frames causes the collapsed region to advance into the uncollapsed region. The circles around the fibrils indicate where the thin film loses contact with the substrate; these are the bumps seen in Figure 1.1(b) of the main chapter.**

particles over the sample. After shaking the sample to remove any loose particles, we attempted to clean the surface in one of two ways. Firstly, we subjected it to a gentle flow of $N_2$ gas. Alternatively, we pressed a slab of *flat* PDMS into the sample two or three times. We found that in both cases, the particles deposited on the collapsed region were removed but those on the uncollapsed region were not. This demonstrates directly that particles that easily foul the uncollapsed region have much poorer adhesion compared to the uncollapsed region. It also shows that the uncollapsed region has stronger adhesion than the flat control while the collapsed region has weaker adhesion than it.

Figure 3.5 demonstrates the ability of this structure to undergo an uncollapse-collapse cycle. Starting with the uncollapsed state (Figure 3.5($a_1$) and ($a_2$)), by applying an external pressure we can collapse the structure over the entire sample (Figure 3.5($b_1$) and Figure 3.5($b_2$)). Then, we press on the collapsed top surface using a material with greater adhesion (usually another uncollapsed fibrillar material) and peel it slowly. Figure 3.5(c) shows that as we peel, two fronts sweep across the sample. The first one, captured in Figure 3.5($c_1$) is the boundary between collapsed and uncollapsed region. Ahead of the collapse-uncollapse front, the structure is collapsed; behind it, the structure is uncollapsed. A second front follows the first one (Figure 3.5(c2)), representing the peeling boundary. The structure between the two fronts is but still attached to the peel arm. After the second front has passed, the sample has returned to its starting state – compare Figure 3.5($d_2$) and ($a_2$). Later in the chapter we show that this cycle can be repeated many times.

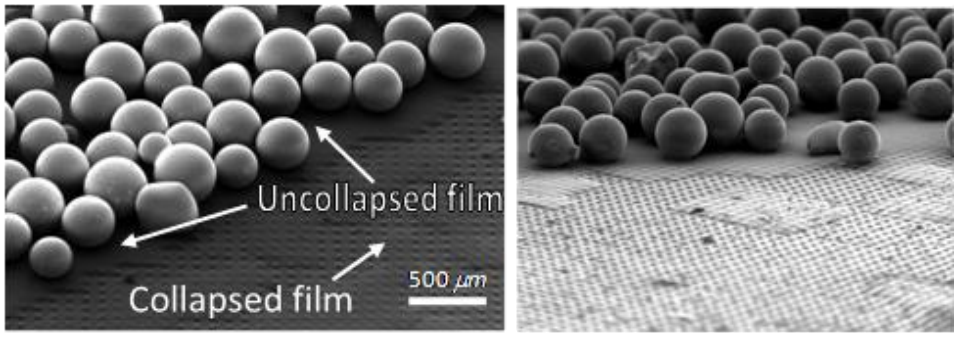


**Figure 3.4 Glass particles distributed on a sample with collapsed and uncollapsed regions demonstrate the adhesive differences between the two states. After the glass particles were adhered to the sample, a flow of $N_2$ was used to clean the fibrillar sample. It was effective in removing particles from the collapsed region but failed to do so from the uncollapsed region.**

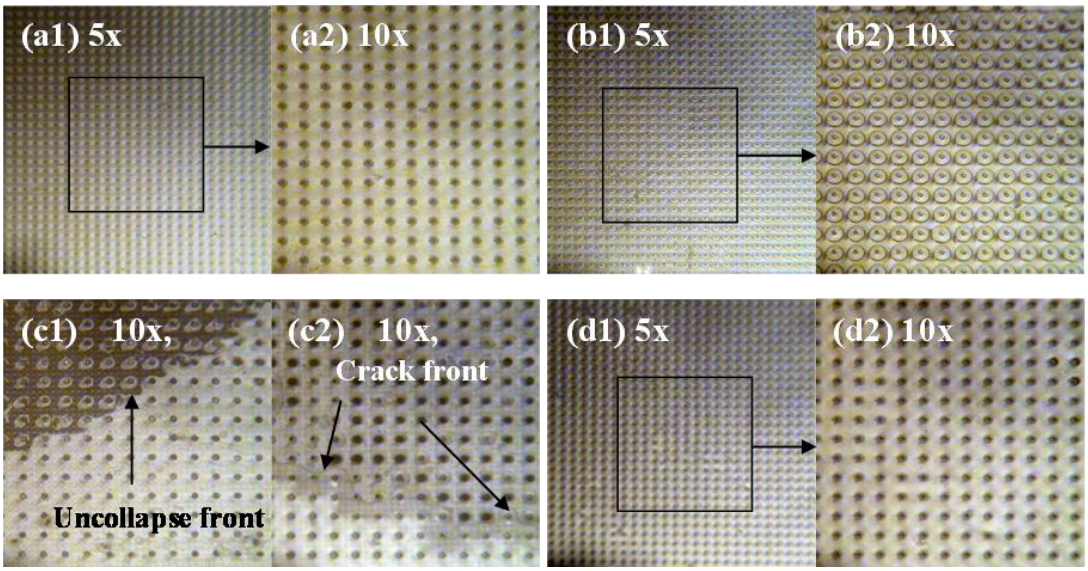


**Figure 3.5 Images from a sequence in which the entire sample begins in the (a) uncollapsed, adhesive state; ($a_1$) is the zoomed out image (5x magnification) while ($a_2$) is an image with 10x magnification in which the dark spots represent fibrils. (b) Next, the sample is switched to a collapsed, low-adhesion state. Again, two magnifications are shown, ($b_1$) and ($b_2$). The circles around the dark spots represent the boundary of the collapsed region around each fibril. We show that the collapsed state can be (c) easily uncollapsed. In (c) there are three distinct areas. In ($c_1$), the upper left corner (where it is dark) is the still-collapsed area. The uncollapsed front is the boundary between the collapsed and uncollapsed regions. In ($c_2$), we observe a crack front where the sample is separating from the second fibrillar sample being used to uncollapse it. (d) The sample has returned to its original adhesive state.**

The demonstrated bistability and clear differences in adhesive performance between the collapsed and uncollapsed states leads to two questions. How does the adhesion of the collapsed state compare quantitatively with that of the uncollapsed state and an unstructured control? Under what conditions do we achieve bistability? We address these questions in the next two sections.

### *3.3.2 Adhesion Measurements*

Indentation tests were performed on samples of three fibril lengths – 10.6 μm, 17.8 μm, and 23.2 μm – for eight fibril center-to-center spacings each, 20 μm, 35 μm, 50 μm, 65 μm, 80 μm, 95 μm, 110 μm and 125 μm. For each set of fibril lengths, for a certain range of inter-fibril spacing, the samples were found to have a second, metastable state in which the thin film, if brought into contact with the substrate by application of external load, would remain collapsed upon removal of the load. For shorter fibril lengths, the range of spacings that are collapsible increases while for longer fibril lengths, fewer samples were capable of achieving the second metastable state.

Figure 3.6(a) shows force-displacement results from a typical indentation test on a sample with 10.6 μm tall fibrils and 95 μm interfibrillar spacing. We first note that the pull-off force, our measure of adhesion, is much larger in the uncollapsed state than in the flat control sample. The collapsed state shows essentially zero adhesion. This is consistent with the results from the self-cleaning experiment in which the PDMS slab (similar to a control) was capable of removing the particles from the collapsed portion of the sample but not from the uncollapsed region. Secondly, the

uncollapsed state is significantly more compliant whereas the collapsed state is only marginally more compliant than the flat control. The results for the uncollapsed sample are very similar to those we have reported previously and demonstrate characteristics of adhesion enhancement by crack-trapping, such as intermittent crack advance and hysteresis [9][14]. For the collapsed sample, initially, contact is only partial and restricted to the tops of bumps. Eventually, in an inner region the indenter makes nearly full contact (see micrograph E in Figure 3.6(b)), but reverts back to partial contact everywhere on unloading (see micrograph F in Figure 3.6(b)). Pictures like E/F have also been reported by Crosby, *et al*. [55]. However, for taller fibrils, contact usually remained restricted to the tops of the bumps throughout the experiment. This partial contact is responsible for the drastic reduction in adhesion.

Figure 3.7 shows results from indentation experiments on samples for four different interfibrillar spacings for all three fibril heights, for both the collapsed and uncollapsed states. As expected, adhesion of the uncollapsed state is always significantly greater than that of the flat control. On the other hand, the adhesion of the collapsed states is generally very small. For samples that are marginally metastable in the collapsed state, we often observe that an initially collapsed state can be locally uncollapsed on retraction of the indenter. In these cases, we also measure some adhesion, for example, as seen in Figure 3.7(d), 65 μm spacing.

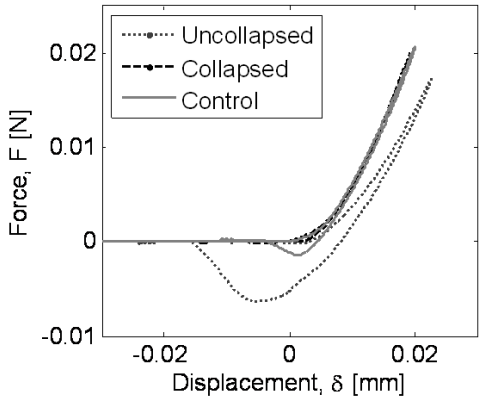


(a)

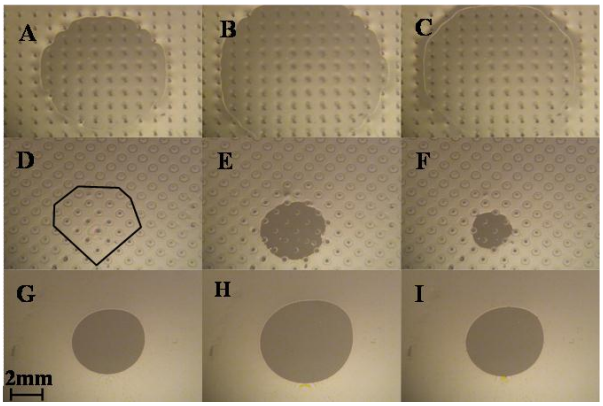


(b)

**Figure 3.6 (a) Force-displacement results from a typical indentation test on a sample with 10.6 μm tall fibrils and 95 μm interfibrillar spacing. Negative force indicates tension. Notice that in the uncollapsed state the pull-off load is much larger than in the control while in the collapsed state the pull-off load is vanishingly small. (b) Optical micrographs of the contact region halfway to maximum indentation (A, D, and G), at maximum indentation (B, E, and H), and halfway retracted from maximum indentation (C, H, and I) for the uncollapsed (A, B, and C), collapsed (D, E, and F), and control (G, H, and I) samples.**

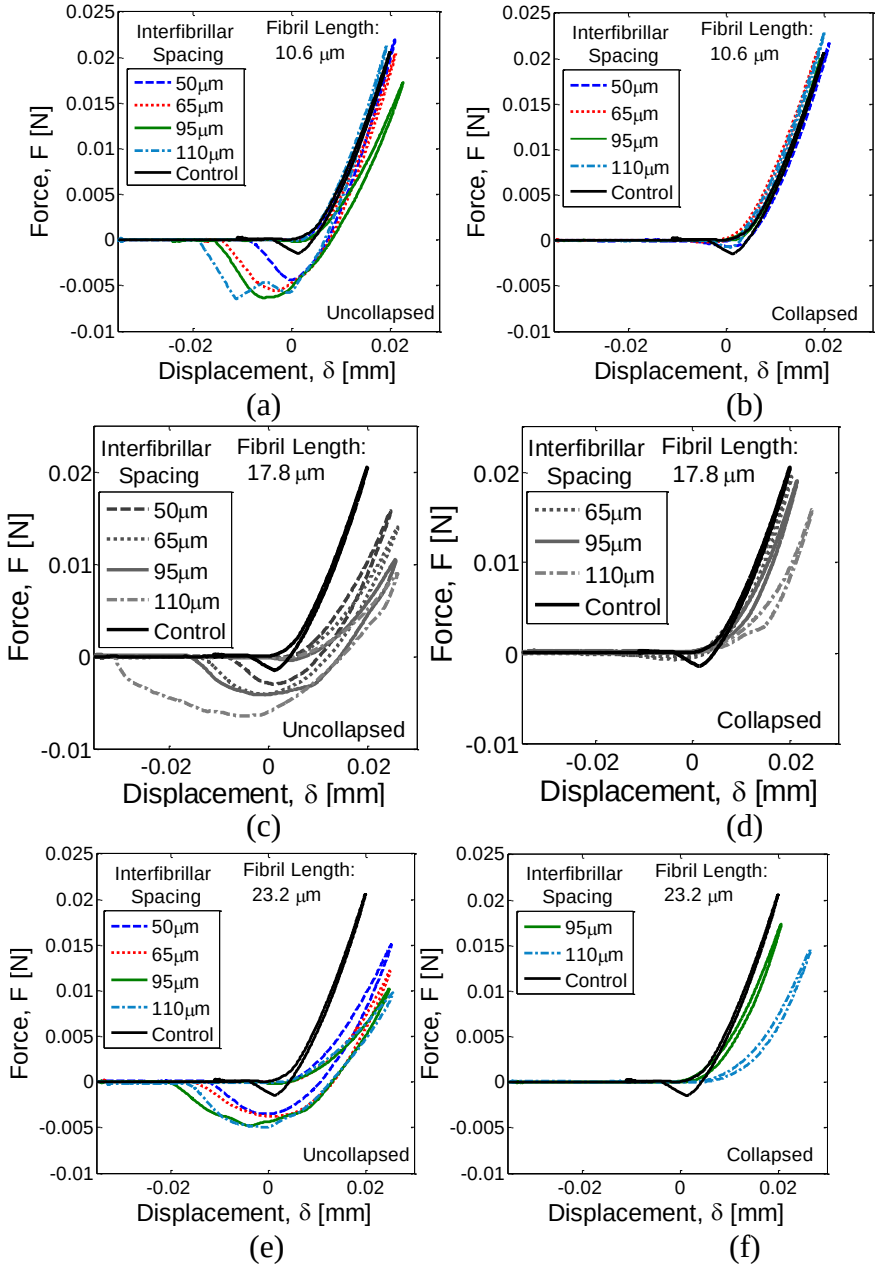


**Figure 3.7 Left column (a, c, e): Force vs. indenter displacement during indentation of uncollapsed samples for three different fibril lengths.; results from an unstructured control are also shown. Right column (b, d, f): Force-displacement measurements on the same samples in the collapsed state for three different fibril lengths.**

It is known that the work of adhesion between PDMS surfaces is rate-dependent [9][39]. Also, the rate dependence of the work of adhesion between the glass indenter and PDMS is different from that of the internal PDMS-PDMS surface. Matthew *et al*. 2006 [56] have previously used such differences to pick-up and place PDMS structures. We have observed that slow removal of the indenter leaves the structure in a collapsed state and that, if the removal of the indenter is rapid, uncollapses the sample. This presents another route to switch the adhesion on and off in the FTFA.

### *3.3.3 Compliance*

As observed previously, compliance of the uncollapsed samples increases systematically with spacing [57]. The maximum true indentation is lower than the nominal maximum displacement applied to the motor (30 μm) because of compliance in the load cell. As the sample compliance increases, the maximum indentation depth approaches the displacement applied to the motor, as can be seen in Figure 3.7.

For collapsed samples, the contact compliance is much smaller, similar to that of the flat control, particularly for samples with 10.6 μm and 17.8 μm long fibrils. As can be seen in the sequence of images in Figure 3.6(b) (D-F), for collapsed samples contact is initially partial as the indenter is supported only by the 'bumps'. For shallow indentation, the compliance is expected to be similar to that of the uncollapsed state for which, although the contact is continuous, vertical loads are supported primarily by the fibrils. With deeper indentation in the collapsed state (e.g. E in Figure 3.6(b)), the indenter makes nearly full contact with the substrate in an inner region

entered at the tip of indenter. For these cases, compliance is expected to decrease and approach that of the flat control. This transition from partial to full contact is more difficult to achieve with longer fibrils. Therefore, we find that samples with longer fibrils show an increase in compliance even in the collapsed state (see Figure 3.7(b)).

To understand more quantitatively how compliance varies, we utilize the model developed by [57] for indentation of a fibrillar structure by a flat punch of radius, *R*. During loading, the area of contact between the indenter and the sample grows steadily for all samples. However, during unloading, there is a period of time during which the contact is pinned. For the control and uncollapsed FTFAs, this is due to the adhesion. For the collapsed samples, as is explained in more detail later, the area remains constant for some period until the outline of contact jumps inward. In all cases, as the contact area remains constant immediately after the indenter begins retracting, we are able to compare the incremental compliance measured at that point to the predictions of the flat-punch model of Long *et al*. 2008 [57]. The experimental compliance was obtained by taking the inverse of the slope of the force-displacement curve immediately after unloading begins. Long's theory states that the compliance can be described by a single parameter, $\alpha^*$, which is determined by the stiffness of the fibrillar layer, $k = \rho EA/w_o$, the punch radius (identified here with the contact radius at maximum contact, *R*), and the Young's modulus of the material, *E*. The parameter $A = s^2$ is the cross-sectional area of a fibril, $w_o$ is the fibril length, and $\rho$ is the number of fibrils per unit area or the fibril density ($1/4a^2$). The compliance, *C*, of a fibrillar sample with a finite backing layer of thickness $T_s$ is given by,

$$C = \left(\frac{1}{k\pi R^2}\right)\left(\frac{\pi^2\alpha^{*2} + 46.4\alpha^* + 16}{4\alpha^* + 16}\right) \tag{3.1}$$

Here,

$$\alpha^* = \frac{\alpha}{1 + \chi\left(\eta = R/T_s\right)} \tag{3.2}$$

where $\alpha = 3kR/2\pi E$ and $\chi$ is defined by

$$\chi(\eta) = \left(1.095\eta + 1.3271\eta^2 + 0.1431\eta^3\right)/0.9717 \tag{3.3}$$

The compliance is normalized by that of a flat, circular punch of radius *R* indenting an elastic half-space, ($\overline{C} = C/C_B$, $C_B = 1/\left(2RE^*\right)$, $E^* = E/\left(1-\nu^2\right)$).

The contact area at maximum indentation was measured for the collapsed and uncollapsed samples. As shown in Figure 3.5(*b*) *D-F*, the indenter sometimes makes partial contact with the tips of the fibrils. In such cases, we take the edge of the contact area to be the convex hull of the set of fibrils in contact with the indenter (see Figure 3.5(*b*), *D* for an example.)

Note that as the fibril height, $w_o$, decreases, the compliance given by equation (3.1) approaches that of an unstructured layer with finite thickness, that is,

$$C = \frac{C_B}{1 + \chi(\eta)} \tag{3.4}$$

We extracted the Young's modulus of the PDMS by applying (3.4) to the measured compliance in a flat control sample upon initial unloading from maximum indentation and obtained a value of $E$ = 1.8 MPa.

Figure 3.8 shows the measured compliance in uncollapsed and collapsed samples for samples with 23.2 μm long fibrils, compared to the prediction from Long's model, (3.1). Results for samples with shorter fibrils are qualitatively similar. We find that the measured compliance is significantly smaller than that predicted by the model based on fibrils alone for both the uncollapsed and collapsed samples. For the uncollapsed samples, we attribute the difference to the load-bearing capacity of the terminal film, the effect of which has not been included in the model. One might expect the model to apply better in the case of the collapsed structure, since the terminal film has collapsed onto the substrate. However, we find that the discrepancy is even greater. This fact is directly related to the observation that during indentation of collapsed samples, the indenter makes contact with both the pillars and the substrate between pillars (see Figure 3.5) and thus the incremental compliance is not very different from that of a flat control.

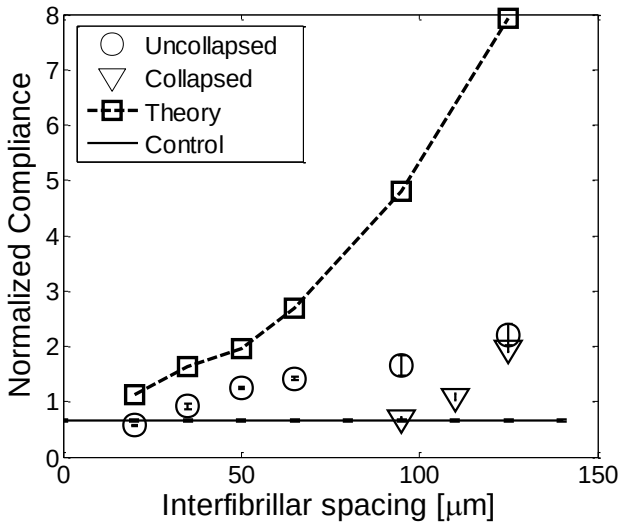


**Figure 3.8 Compliance normalized by $C_B = 1/2RE^*$ for samples with 23.2 μm long fibrils. The horizontal line represents measurements on a flat control. Circles and triangles represent compliance measured on uncollapsed and collapsed samples, respectively. The dashed line shows the compliance predicted theoretically by equation (3.4).**

In Figure 3.9, we plot the normalized pull-off load, $F_{max}$, for the eight different spacings and three different fibril heights for both the collapsed and uncollapsed states (the solid lines are drawn as guides to the eye). The loads are normalized by the average pull-off load for the flat control sample. It is clear that the adhesion for the uncollapsed samples is larger than that of the control, increases with fibril spacing and is relatively insensitive to the fibril height, which is characteristic of the crack-trapping mechanism [9][14][58]. On the other hand, the adhesion of the collapsed states is lower than that of the control, decreases strongly with increasing spacing, and is negligible or close to zero for several samples. That is, the structure can be designed such that the ratio of adhesion in the "on" or uncollapsed state and the "off" or collapsed state approaches two orders of magnitude. For example, we are able to achieve ratios of the pull-off force in the uncollapsed to collapsed state up to 70 for the for interfibrillar spacings of 110 μm and 125 μm.

Note that data on collapsed samples is presented for fewer spacings than for the uncollapsed samples. Whereas the uncollapsed state is always metastable, for a given fibril height, the collapsed state is metastable only for sufficiently large spacing between fibrils. The minimum spacing for bistability increases with increasing fibril height. In the theory section we provide a model to explain both of these experimental findings.

For structures whose pull-off is controlled by crack-trapping, as is the case for the uncollapsed samples, the adhesion energy enhancement is proportional to the fourth power of the interfibrillar spacing [41][48]. Consistent with this expectation, indentation experiments demonstrate a distinct increase in the pull-off load as the

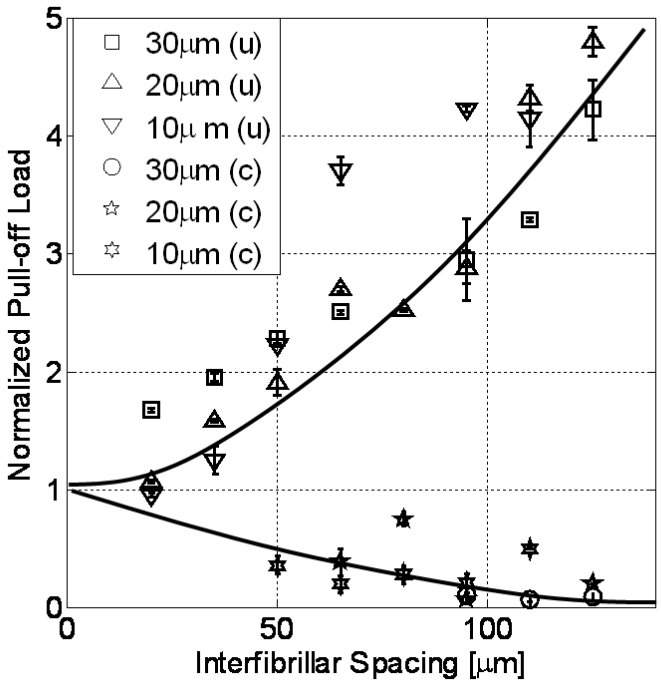


**Figure 3.9 Pull-off load (normalized by the maximum pull-off load for the flat control sample) for collapsed and uncollapsed samples. For the uncollapsed samples, the pull-off load is significantly enhanced over the flat control sample and increases with interfibrillar spacing while for the collapsed samples, the pull-off load remains low or negligible. In the legend, '(c)' represents the collapsed samples and '(u)' represents uncollapsed samples.**

interfibrillar spacings grow. Eventually, this growth is limited by factors such as cavitation under fibrils or damage to the structure.

To understand the effect of fibril spacing on adhesion of collapsed samples, we use the model described in Vajpayee, *et al.* [59]. That model treats the surface as an elastic spring foundation, neglecting the elasticity of the backing layer. Each fibril is assumed to detach at a critical stress, $\sigma_c$. Then, the pull-off force is given by

$$F_{pull-off} = -\pi\rho R\frac{\sigma_c^2 A w_o}{E} \tag{3.5}$$

i.e., it decreases inversely with the square of interfibrillar spacing since $\rho = 1/4a^2$. Thus, the model in [59] also predicts that adhesion of collapsed structures decreases with fibril density (increased interfibrillar spacing).

Finally, to ascertain the robustness of properties in the context of multiple switching between states, we cycled a sample (with 10.6 μm long fibrils, a 5 μm thin film, and inter-fibril spacing of 65 μm) 100 times between the collapsed and uncollapsed states. In Figure 3.10, we show that the surface compliance and adhesion of the two states remained substantially unchanged (within test-to-test variability). We see no reason why the material could not be cycled many more times between the two states.

### *3.3.4* Linear Theory of Plate Collapse

In the previous sections we established experimentally that, if the FTFA is designed appropriately, it can reside in one of two metastable states, one with a collapsed and an uncollapsed terminal film, and that these two states have markedly different adhesion.

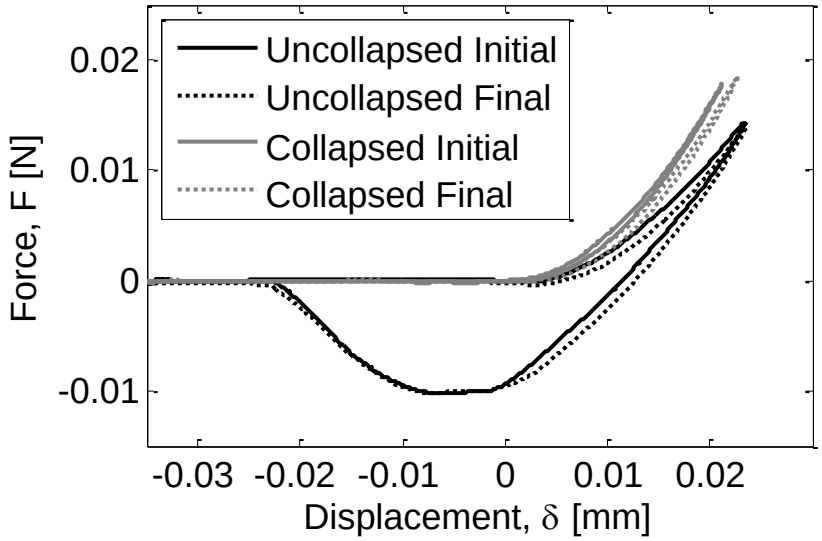


**Figure 3.10 A demonstration that properties remain substantially unaltered despite multiple switching between the two states: force-displacement data from a 65 µm sample with 10.6 µm fibrils and a 5 µm thin film. Indentation tests were initially performed on collapsed and uncollapsed areas. The sample was then collapsed by mechanical pressure from above and uncollapsed by peeling with a dry adhesive 100 times. Indentation tests were repeated and are shown as well. It can be seen that the sample can be repeatedly cycled between the collapsed (non-adhesive) and uncollapsed (enhanced adhesion) states without degradation of its properties.**

Therefore, an important question is: for what combination of parameters (material property and geometrical) can we expect the structure to be bistable?

In this section, we present a simple model to provide insight into this question of the collapse of the terminal thin film. The work on linear plate theory was done by co-author and labmate, Jing Ning. Related models have been developed to describe the pull-off of a clamped circular film adhered to a flat cylindrical punch [60][61]. The film is modeled as an elastic circular plate suspended at a height of $w_o$ above a rigid substrate, where $w_o$ represents fibril length. To simplify the problem, we neglect the deformation of the fibrils, represent the complex geometry of the terminal film by a circular plate, and assume that the plate is clamped at its boundaries. The plate is brought into contact with a rigid flat substrate by a uniform pressure $q$ as shown in Figure 3.11. The circular plate has thickness $h$, elastic modulus $E$, Poisson's ratio, $\nu$, and flexural rigidity $D$ given by:

$$D = Eh^3 \big/ 12\left(1-\nu^2\right) \tag{3.6}$$

The radius of the circular plate and contact radius between the plate and the substrate are denoted by $a_d$ and $c$ respectively; we equate the former to half the diagonal distance between fibrils in a square unit cell.

The differential equation for symmetrical bending of circular plates [62], using the coordinate system defined in Figure 3.11, is given by:

$$\frac{1}{r}\frac{d}{dr}\left\{r\frac{d}{dr}\left[\frac{1}{r}\frac{d}{dr}\left(r\frac{dw}{dr}\right)\right]\right\} = \frac{q}{D} \tag{3.7}$$

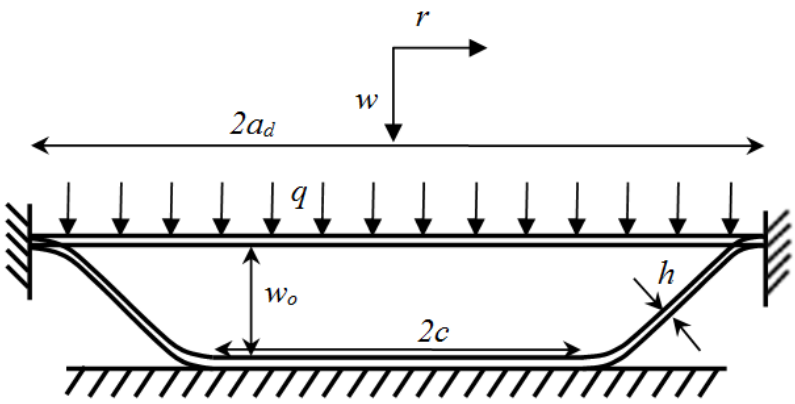


**Figure 3.11 Schematic drawing of a plate adhered to a rigid substrate under uniform pressure**

The boundary conditions are:

$$\begin{aligned} &w\left(r=c\right)=w_0 \\ &w'\left(r=c\right)=0 \\ &w\left(r=a_d\right)=w'\left(r=a_d\right)=0 \end{aligned} \tag{3.8}$$

We normalize the governing equation and boundary conditions as follows:

$$\overline{w}=\frac{w}{w_0},\ \overline{r}=\frac{r}{a_d}\ ,\overline{q}=\frac{qa_d^4}{Dw_0},\ \overline{c}=\frac{c}{a_d} \tag{3.9}$$

The general solution for the normalized deflection is:

$$\overline{w}=\frac{1}{64}\overline{r}^4\overline{q}+C_1\overline{r}^2\ln\overline{r}+C_2\overline{r}^2+C_3\ln\overline{r}+C_4 \tag{3.10}$$

Applying the boundary conditions in (3.8), we obtain four equations for five unknowns $C_i$ and $\overline{c}$ :

$$\begin{aligned} &\frac{1}{64}\overline{q}+C_2+C_4=0 \\ &\frac{1}{16}\overline{q}+C_1+2C_2+C_3=0 \\ &\frac{1}{64}\overline{c}^4\overline{q}+C_1\overline{c}^2\ln\overline{c}+C_2\overline{c}^2+C_3\ln\overline{c}+C_4=1 \\ &\frac{1}{16}\overline{c}^3\overline{q}+2C_1\overline{c}\ln\overline{c}+C_1\overline{c}+2C_2\overline{c}+\frac{C_3}{\overline{c}}=0 \end{aligned} \tag{3.11}$$

The additional equation which allows us to solve for the five unknowns is determined by energy balance; that is, the potential energy released by the system (plate + applied

pressure), $G$, to peel off a unit area of contact must be equal to the work of adhesion $W_{ad}$ of the surfaces in contact. This condition is (see for example, [63])

$$W_{ad} = G = \frac{D}{2}\left(w''\right)^2\Big|_{r=c} = \frac{Dw_0^{\ 2}}{2a_d^4}\left(\bar{w}''\right)^2\Big|_{r=\bar{c}} \tag{3.12}$$

Using (3.12), (3.10) is found to be:

$$\bar{W}_{ad} = \left(\frac{3}{16}\bar{c}^2\bar{q} + 2C_1\ln\bar{c} + 3C_1 + 2C_2 - \frac{C_3}{\bar{c}^2}\right)^2 \tag{3.13}$$

and we define:

$$\bar{W}_{ad} = \frac{2a_d^4 W_{ad}}{Dw_0^2} \tag{3.14}$$

as the normalized work of adhesion. The solution of (3.10) and (3.12) is:

$$C_1 = \frac{\left(-\bar{c}^2+1\right)\left[64+\bar{q}\left(\bar{c}^4-1\right)-4\bar{c}^2\bar{q}\ln\bar{c}\right]}{32\left[\left(\bar{c}^2-1\right)^2-4\bar{c}^2\left(\ln\bar{c}\right)^2\right]} \tag{3.15}$$

$$C_2 = \frac{\left(-\bar{c}^2+1\right)\left[-64+\bar{q}\left(\bar{c}^4-1\right)\right]+2\bar{c}^2\ln\bar{c}\left[64+\bar{q}\left(\bar{c}^2-1\right)^2+4\bar{q}\ln\bar{c}\right]}{64\left[\left(\bar{c}^2-1\right)^2-4\bar{c}^2\left(\ln\bar{c}\right)^2\right]}$$

$$C_3 = \frac{\bar{c}^2\left[\bar{q}\left(\bar{c}^2-1\right)^2+\ln\bar{c}\left(-64+\bar{q}-\bar{c}^4\bar{q}\right)\right]}{16\left[\left(\bar{c}^2-1\right)^2-4\bar{c}^2\left(\ln\bar{c}\right)^2\right]}$$

$$C_4 = \frac{\left(\bar{c}^2-1\right)\left[-64+\bar{c}^2\bar{q}\left(\bar{c}^2-1\right)\right]+2\bar{c}^2\ln\bar{c}\left[64+\bar{q}\left(\bar{c}^2-1\right)^2+2\bar{q}\ln\bar{c}\right]}{64\left[\left(\bar{c}^2-1\right)^2-4\bar{c}^2\left(\ln\bar{c}\right)^2\right]}$$

Substituting (3.15) into (3.13) gives the relationship between the applied pressure and the contact radius, i.e.,

$$\bar{W}_{ad} = \left( \frac{\left(\bar{c}^2 - 1\right)\left(-64 + \bar{q}\left(\bar{c}^4 - 4\bar{c}^2 + 3\right)\right) - 2\ln\bar{c}\left(-64 + \bar{q} + 2\bar{c}^2\bar{q} - 3\bar{c}^4\bar{q} + 4\bar{c}^4\bar{q}\ln\bar{c}\right)}{16\left[\left(\bar{c}^2 - 1\right)^2 - 4\bar{c}^2\left(\ln\bar{c}\right)^2\right]} \right)^2 \tag{3.16}$$

Using the expressions for constants $C_i$, we obtain the relationship between the applied pressure and the contact radius. We then solve for $\bar{q}$, which is:

$$\bar{q} = \frac{64\left(\bar{c}^2 - 1 - 2\ln\bar{c}\right) \pm 16\sqrt{\bar{W}_{ad}}\left[\left(\bar{c}^2 - 1\right)^2 - 4\bar{c}^2\left(\ln\bar{c}\right)^2\right]}{\left(\bar{c}^2 - 1\right)\left(\bar{c}^4 - 4\bar{c}^2 + 3\right) - 2\ln\bar{c}\left(1 + 2\bar{c}^2 - 3\bar{c}^4 + 4\bar{c}^4\ln\bar{c}\right)} \tag{3.17}$$

In (3.17) we see that there are two solution branches. Since the applied pressure to maintain a given contact area is always larger for the solution with the + sign, the negative sign should be chosen.

It is interesting to consider the dependence of the applied pressure on the contact radius in the limit of small contact. A straightforward calculation shows that,

$$\bar{q} \approx 64 + \frac{-64 + 8\sqrt{\bar{W}_{ad}}}{\ln\bar{c}} \tag{3.18}$$

for $\bar{c} << 1$. (3.18) shows that the pressure $q_o$ needed to bring the plate into contact with the substrate ($c = 0$) is

$$q_0 = \frac{64Dw_0}{a_d^4} \tag{3.19}$$

Since $D \propto h^3$, (3.19) suggests that collapse is extremely sensitive to the plate thickness.

Figure 3.12 plots the normalized pressure versus the normalized contact radius for different values of $\bar{W}_{ad}$. The slope of the pressure versus contact radius curve at $\bar{c} = 0$ can be computed using (3.18) and is:

$$\bar{q}' \approx \frac{64 - 8\sqrt{\bar{W}_{ad}}}{\bar{c}\left(\ln \bar{c}\right)^2} \tag{3.20}$$

(3.20) states that the pressure versus contact radius curve has an infinite positive slope for $\bar{W}_{ad} < 64$ and infinite negative slope for $\bar{W}_{ad} > 64$ (see inset in Figure 3.12). The transition occurs at $\bar{W}_{ad} = 64$. For small adhesion ($\bar{W}_{ad} < 64$), the system is stable, in the sense that increasing pressure is needed to increase contact radius. For $\bar{W}_{ad} > 64$, the pressure first decreases with $\bar{c}$, reaches a minimum $\bar{q}_{\min}$ at $\bar{c}_{\min}$, then increases. In this case, the system is unstable for small contact radius ($\bar{c} < \bar{c}_{\min}$) since pressure decreases with increasing contact. The stable solution branch occupies the interval $\bar{c} > \bar{c}_{\min}$. Note that $\bar{c}_{\min}$ increases with $\bar{W}_{ad}$ with $\bar{c}_{\min}(\bar{W}_{ad} = 64) = 0$. Physically, $\bar{c}_{\min}$ is the radius at pull-off and $\bar{q}_{\min}$ is the pull-off pressure.

The curve with $\bar{W}_{ad} = 314.6 \equiv \bar{W}_{ad}^*$ and $\bar{c}_{\min}^* = 0.176$ is particularly important, since the pull-off pressure is *negative* for any $\bar{W}_{ad} > \bar{W}_{ad}^*$. The significance of this is that it defines bistability, i.e., for $\bar{W}_{ad} > \bar{W}_{ad}^*$, once the plate collapses it remains stuck when

pressure is released and one has to apply a *reverse* pressure to revert it back to the initial state.

In Figure 3.13, we show a phase diagram of bistability for the different fibril heights and spacings. For greater spacings and shorter fibrils, bistability is easier to achieve, as expected. Parameters for our PDMS samples are:

$W_{ad} = 138 \text{ mJ/m}^2$
$E = 1.8 \; MPa$
$\nu = 0.5$
$w_o$ = 10.6 μm, 17.8 μm, 23.2 μm
$h$ = 6 μm
$2a$ = 20-125 μm (or $2a_d$ = 28-177 μm).

Filled circles represent combinations of fibril height and spacing that were metastable in the collapsed state; squares represent those that would not remain collapsed. The line represents the condition, $\bar{W}_{ad} = 314.6 \equiv \bar{W}_{ad}^*$; our model predicts that combinations to the right of the line have a collapsed metastable state. The model captures the observation that, for a given fibril height, a minimum interfibrillar spacing is required for the collapsed state to be metastable. It also captures correctly the fact that this minimum spacing increases with increasing fibril height. Given the simplicity of the model the quantitative agreement with experiment is quite good. We do note, however, that the model has several approximations – e.g., we have ignored the large deflections of the terminal film and have represented a square arrangement by an axisymmetric plate – and a better model will be needed for a more quantitative comparison with experiment. Nevertheless, we believe that the simple model captures the essential features of bistability.

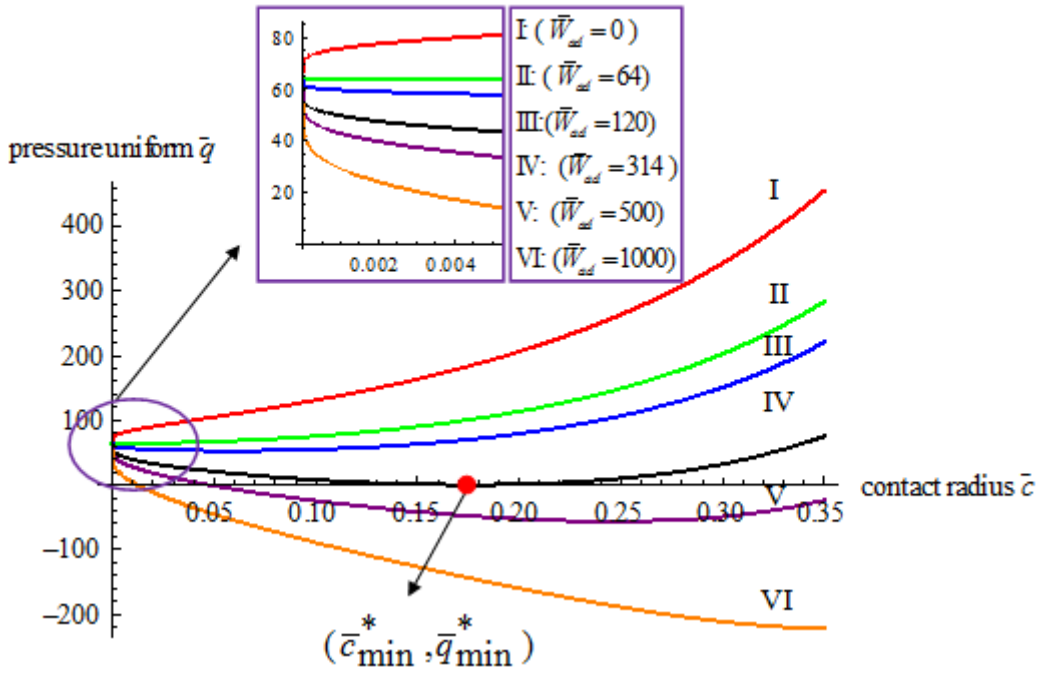


**Figure 3.12 Plot of normalized pressure versus contact radius for six $\bar{W}_{ad}$. In LPT, we define bistability as requiring a negative pressure to uncollapsed the FTFA, i.e., to reduce the contact area to zero.**

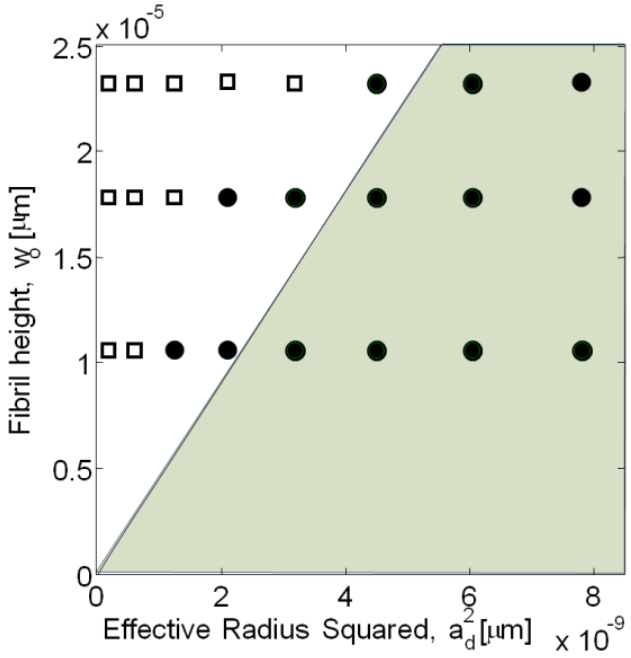


**Figure 3.13 Phase diagram of fibril spacing and heights for bistability from Linear Plate Theory. Filled circles represent combinations of fibril height and spacing that were metastable in the collapsed state; squares represent those that would not remain collapsed. The line represents the condition, $\bar{W}_{ad} = 314.6 \equiv \bar{W}_{ad}^{*}$; our model predicts that combinations in the shaded region to the right of the line have a metastable collapsed state.**

### *3.4 Summary and Conclusions*

We have demonstrated that a FTFA can have two metastable states. In the first metastable state, a thin film spanning a fibrillar surface results in strongly enhanced adhesion due to a previously studied crack-trapping phenomenon. For certain geometries of this first state, we can achieve a second state by bringing the thin film into contact with the substrate of the fibrillar structure. This second, collapsed state resembles a rough surface and has strongly reduced adhesion, even lower than that of a flat control.

A qualitative demonstration of the difference in adhesive properties of the collapsed and uncollapsed states was made by placing particles a few hundred microns in diameter over a sample that had part of its surface in the first metastable state and another part in the collapsed state. By using $N_2$ gas to blow particles off the sample as well as by using a PDMS slab to remove particles from the sample, we demonstrated that the adhesion of the uncollapsed state caused particles to be difficult to remove. However, particles were easily removable from the collapsed region. To illustrate the robustness of the sample, we showed that one can collapse and uncollapse the sample repeatedly (we repeated this one hundred times) with no significant change in properties.

To explain the phenomenon of bistability in this structure, we developed a simple theoretical model representing the thin film between four posts as a linear circular plate clamped at the edge. This model identifies a dimensionless combination of materials and geometrical parameters including work of adhesion, fibril height, film thickness, elastic modulus, and interfibrillar separation, such that bistability is possible

only when this parameter is sufficiently large. We find that the model captures the experimental findings reasonably well.

# CHAPTER 4

# ADHESIVE AND FRICTIONAL CHARACTERIZATION OF SWITCHABLE ADHESIVE

## *4.1 Introduction*

In this chapter, we present the results from a characterization of the adhesive and frictional behavior of the switchable film-terminated fibrillar architecture (FTFA) as well as a theoretical and experimental description of the switching mechanism. In Section 4.3.1, we discuss how cyclic indentation experiments are used to determine the interfacial hysteresis of both the highly adhesive and non-adhesive states of the bistable FTFA. We also characterize the frictional behavior of the two states. For both indentation hysteresis and friction experiments, we compare the performance of the switchable FTFA to control samples, which are fabricated in the manner similar to what is described in CHAPTER 3. In addition to characterizing the bistable FTFA, we determine the pressure to switch the FTFA from the adhesive to the non-adhesive state using hydrostatic pressure experiments. Finally, in Section 4.4, we present a large deflection, adhesive contact model of the sample as it undergoes switching.

## *4.2 Materials and Methods*

### *4.2.1 Fabrication*

The fabrication method for the FTFA is described in the Chapter 3 as well as [64]. To summarize, fibrillar structures were fabricated by the molding of PDMS using negative image silicon (Si) masters patterned by standard photolithography and DRIE techniques. Bistability depends on several parameters including fibril length, $w_0$,

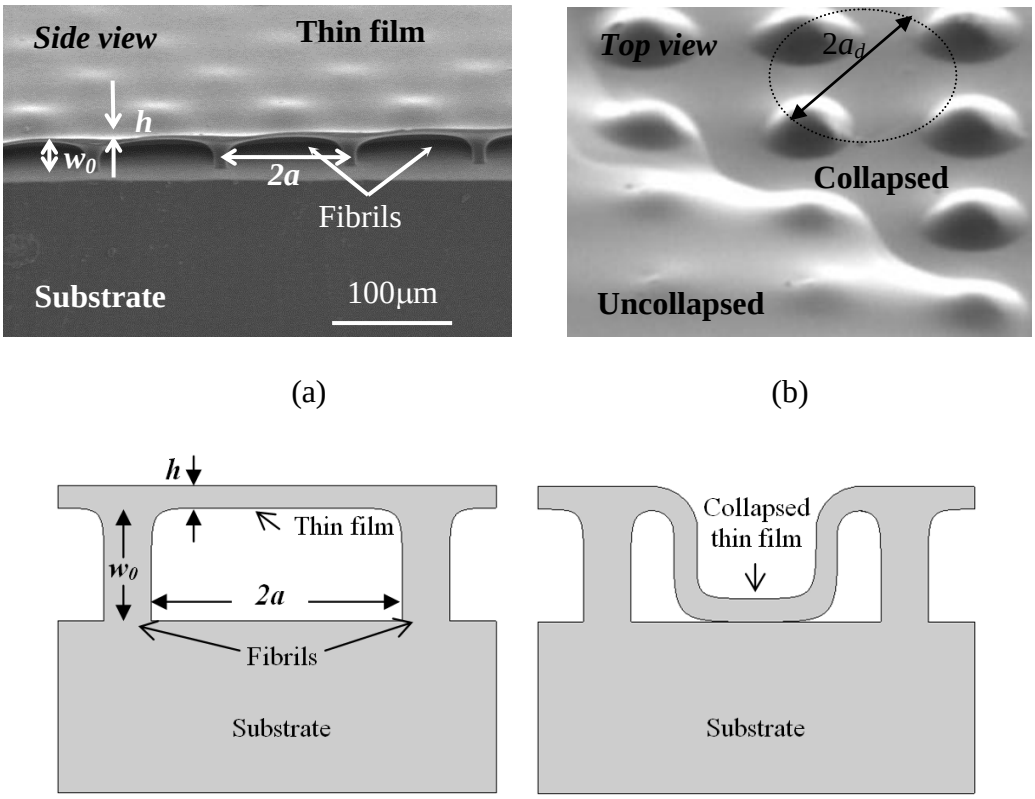


**Figure 4.1 (a) SEM image of the FTFA, shown from the side with sample dimensions noted: thin film thickness, *h*, fibril height, $w_0$, and interfibrillar spacing *2a*. The layer of fibrils is arranged in a square array and each fibril has a 100 μm$^2$ square cross-section. (b) SEM image from above of a sample with both the collapsed and uncollapsed states present. We denote the diagonal distance between two fibrils $2a_d$. In the lower, left-hand corner of the image, the thin film is *uncollapsed* and lies on top of fibrils while in the upper right-hand corner, the thin film has collapsed around the fibrils and is adhered to the substrate. (c) We provide a schematic of the FTFA in the uncollapsed state, with the same parameters shown in (a). In (d), we show a schematic of a cross-section of the FTFA in the collapsed state, corresponding to the collapsed region in (c).**

interfibrillar (center-to-center) spacing, 2*a*, thin-film thickness, *h*, and the effective work of adhesion, $W_{ad}$, as described in [64]. For this work, we used samples with interfibrillar spacings ranging between 20 μm and 125 μm and three fibril lengths: 10.6 μm, 17.8 μm, and 23.2 μm. The fibrils have a 10 μm × 10 μm square cross-section. The 5 μm thin films are fabricated using a spin speed of 3,000 RPM. Spacers were used to provide a 1 mm thick substrate to the fibrillar layer. To attach a terminal film to the ends of the posts, a polymer precursor (again, PDMS) is first spin-coated on a polystyrene-coated Si wafer. The fibrillar layer is then placed on the film while the film is only partially cured (to prevent wicking); together they are cured for 80°C for two hours. The entire sample is removed from the wafer manually.

### *4.2.2 Measurement of adhesion and friction*

#### *Adhesion*

Cyclic indentation experiments were performed to measure adhesion of the samples. Details of this experiment can be found in Noderer, *et al.* [14] and a schematic of the set-up is the same as shown in Figure 3.2. For these experiments, the 4 mm radius, SAM-coated glass sphere indents the sample to a prescribed maximum depth of 30 μm and then retracts to a specified minimum depth (that maintains contact); this loading cycle is repeated four times. The force on the indenter is recorded by a computer data acquisition system and the displacement is determined by the motorized vertical stage as well as a capacitance sensor. Contact between the indenter and sample is viewed through the microscope and direct digital streaming video of the corresponding contact

evolution is recorded. We perform the experiment three times on each sample and report the average value and standard deviation.

***Friction***

The apparatus used to measure the response of samples in the adhesive and non-adhesive states as they undergo shear displacement is shown in Figure 4.2. Details of the friction experiment can be found in [39][41]. Briefly, a SAM-coated glass indenter with a 4 mm radius is brought into contact with a FTFA sample on a glass slide using the minimum possible normal load to maintain contact via a mechanical balance (Ohaus 310D). The samples were displaced laterally with a variable speed motor (Newport ESP300) at a fixed velocity of 10 μm/s. The frictional force was measured by a load cell (Honeywell Precision Miniature Load Cell model 31-50) attached on the balance arm in the direction parallel to the sliding motion. We perform the experiment three times on each sample and report the average value and standard deviation.

## *4.3 Results*

### *4.3.1 Interfacial hysteresis results*

In Chapter 3, the maximum measured tension experienced by the indenter upon retracting from the sample, $F_{pull\text{-}off}$, was presented as a measure of adhesion of the FTFA in the collapsed and uncollapsed states. While this is a widely used measure, the pull-off load can change significantly with increasing maximum indentation to some saturated value. Schargott, *et al*. [65] determined the minimum compressive preload required to reach this saturated value for a spherical indenter on a spring foundation

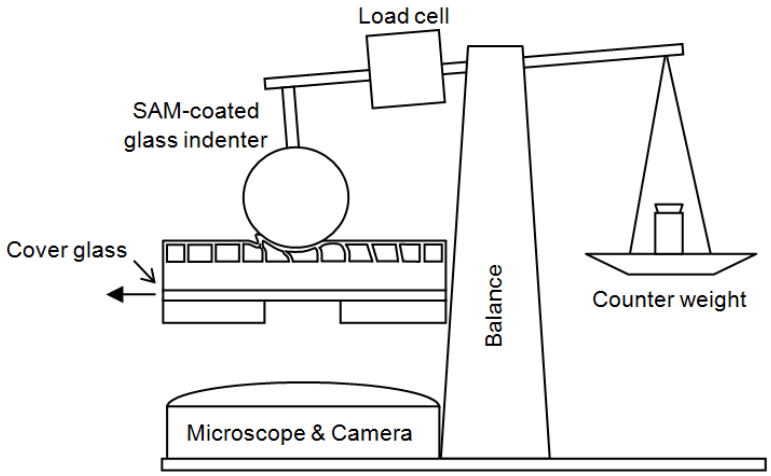


**Figure 4.2 Experimental set-up for the friction experiments. A SAM-coated spherical indenter with a 4 mm radius is brought into contact with the sample. The sample is driven at a constant rate using a motorized stage. The shear force on the indenter is measured using an in-line load cell and the contact between the indenter and sample is obtained by recording its image through the inverted optical microscope.**

atop a rigid backing layer. In Long, *et al.* [57] the elasticity of the substrate for a fibrillar layer was accounted for in the case of a cylindrical punch indenter. Presently, there is no analytical or numerical solution for the case of a spherical indenter on a fibrillar surface with finite or infinite backing. Thus, care must be taken either to specify the indentation depth/maximum load or to indent sufficiently to ensure the pull-off load no longer depends on indentation depth.

Alternatively, if there is no bulk dissipation, cyclic indentation experiments can be used to extract interfacial hysteresis as a measure of adhesion in a completely model-independent manner [39]. In a simplified version of this theory, interfacial hysteresis is calculated by:

$$\Delta W \equiv \frac{\oint P d\delta}{\Delta A} \tag{4.1}$$

The integral in the numerator is the net area under the force-displacement curve during a loading cycle and $\Delta A$ is the difference between the contact areas at maximum and minimum indentation. $\Delta W$ is the work done per unit area to make or break contact. Force-displacement data for this experiment is shown in Figure 4.3. In previous papers, it has been shown that the hysteresis for the FTFA comes from the process of separation and not the bulk material properties [14].

During the cyclic loading, contact between the glass indenter and FTFA sample grows and shrinks from the edge of contact. As described in CHAPTER 3, we can think of the contact edge as an edge crack and, in turn, think of the increasing contact between the indenter and the sample as a crack that is healing and shrinking contact between the indenter and sample as a crack opening.

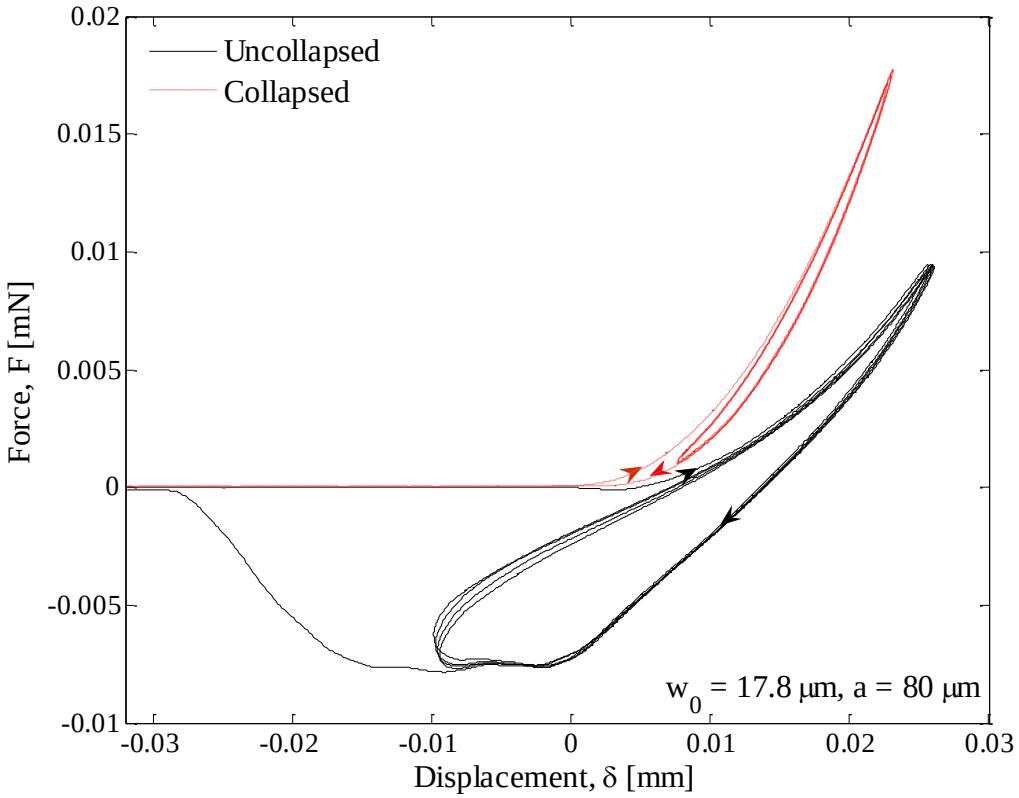


**Figure 4.3 Force-displacement data from a cyclic indentation experiment on a sample ($w_0$ = 17.8 μm, $2a$ = 80 μm). Positive forces indicate compression and negative forces indicate tension. Arrows on the plot indicate the glass indenter is compressing and retracting from the sample.**

In many situations, it is possible to define a work of adhesion for crack opening, $W^+$ as well as for crack healing, $W^-$, respectively, and write (4.1) as:

$$\oint P d\delta \approx \left(W^+ - W^-\right)\Delta A \tag{4.2}$$

If $W^+ \gg W^-$, the hysteresis per unit area is well-approximated by $W^+$. However, if $W^+ \approx W^-$, then the hysteresis per unit area vanishes. For the collapsed samples, there is not enough hysteresis for us to reasonably make the approximation for $W^+$, so we report the interfacial (adhesion) hysteresis, $\Delta W$.

The adhesion hysteresis in the uncollapsed samples is up to four times greater than the control samples; these results are shown in Figure 4.4. In [41], it was shown that the adhesion enhancement is due to a crack-trapping mechanism that arises from the variation in strain energy present within the sample available to drive the crack.

For the collapsed samples, the adhesion hysteresis is even lower than the hysteresis for the control samples. In addition to having no adhesion enhancement from the crack-trapping mechanism, contact for these samples is (at least initially) reduced by the bumps on the surface. For shorter fibrils, the indenter comes into contact with the substrate in the center of contact.

### *4.3.2 Friction Results*

In Figure 4.5, we show the force-displacement response for both collapsed and uncollapsed samples with $w_0$ = 10.6 μm from the friction experiment. For uncollapsed samples, there is initially no relative movement between the sample and the indenter at the interface. During this period the measured shear force on the indenter increases to

a peak value. After the peak friction force is reached, the sample transitions to steady sliding and exhibits a much lower shear force. For the collapsed samples, there is no observable static friction peak; instead, the sample slides steadily throughout.

It has been shown previously on the uncollapsed FTFA that the static friction increases systematically with interfibrillar spacing [51], implying the enhancement is due to the enhanced adhesion. As in [51], we observed a significant increase in the peak friction force in uncollapsed FTFA samples over the control up to an intermediate spacing (in Figure 4.5 this is $2a$ = 95 μm). For larger spacings, the sample is damaged during the experiment. In Figure 4.5, one can see that the measured shear force drops dramatically once the sample is damaged.

In Shen, *et al*. [40], an unstable release of the shear strain in the contact region between the indenter and the sample occurs at the static friction peak, resulting in a dramatic drop in the shear force. After the instability takes place, the sample begins sliding with respect to the indenter. Additionally, the shear force is independent of spacing and identical to that of the flat control. This was attributed to the fact that in sliding friction the normal load is supported by the tension in the thin film as the sheared fibrils have very little stiffness.

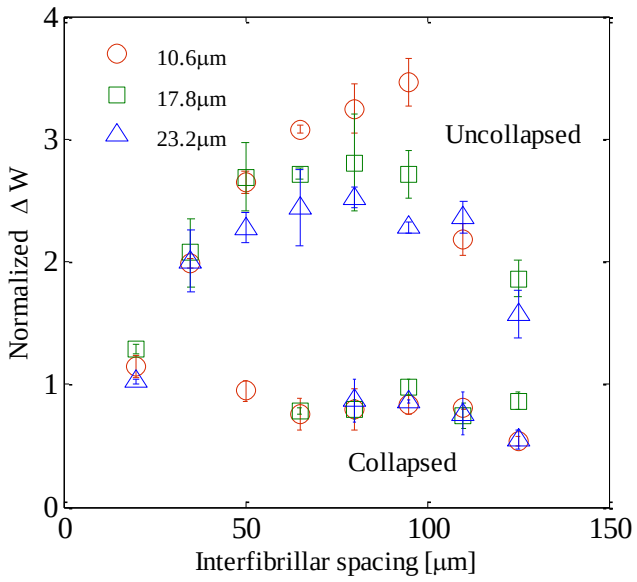


**Figure 4.4** $\Delta W = W^+ + W^-$ **normalized by** $\Delta W$ **for the control sample. Results from the interfacial hysteresis experiments are shown for collapsible samples with** $w_0$ **= 10.6, 17.8, and 23.2 μm and 2***a* **= 20 – 125 μm.**

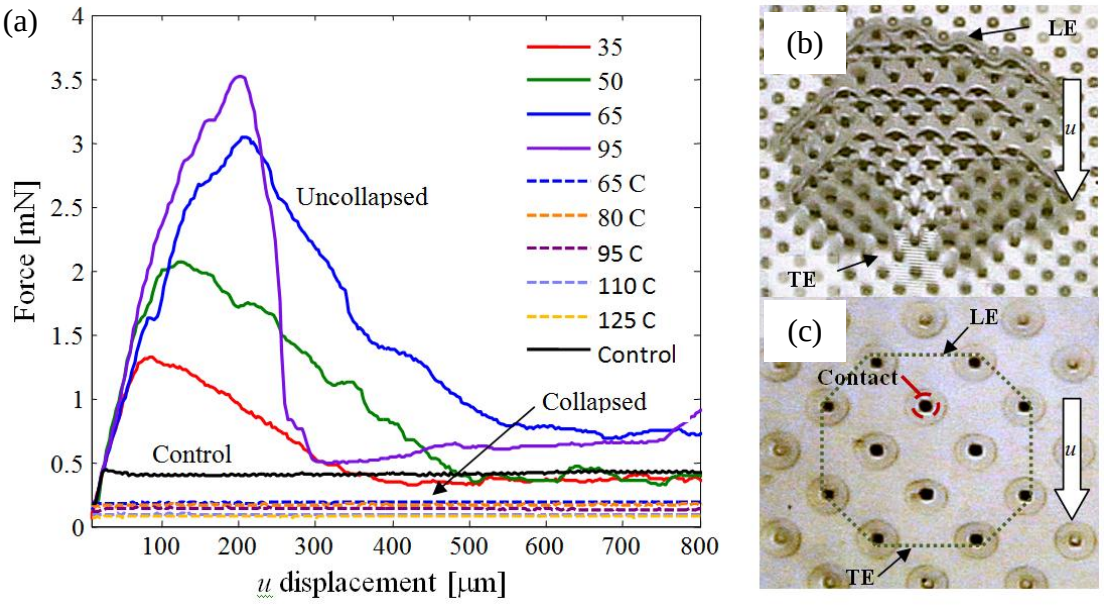


**Figure 4.5 (a) Shear force as a function of sample displacement, *u*, for experiments on samples with $w_0$ = 10.6 μm in both uncollapsed (2*a* = 35 μm, 50 μm, 65 μm, 95 μm) and collapsed states (2*a* = 65 – 125 μm and denoted by 'C'). For 2*a* = 95 μm and more, the thin film tears for the uncollapsed samples at the peak friction force. For the collapsed samples, spacings reported are limited to bistable FTFAs. (b), (c) Micrographs showing the contact between the indenter and the sample during the experiment (for the uncollapsed, it is during steady sliding). Arrows indicate the motion of the sample and 'LE' and 'TE' point to the leading edge and trailing edge of contact, respectively. In (b), $w_0$ = 10.6 μm, 2*a* = 50 μm in the uncollapsed state, there is a large area of contact between the indenter and the sample, while for (c), $w_0$ = 10.6 μm, 2*a* = 80 μm in the collapsed state, the contact is restricted to the tips of the bumps, which occupy the region outlined by an octagon.**

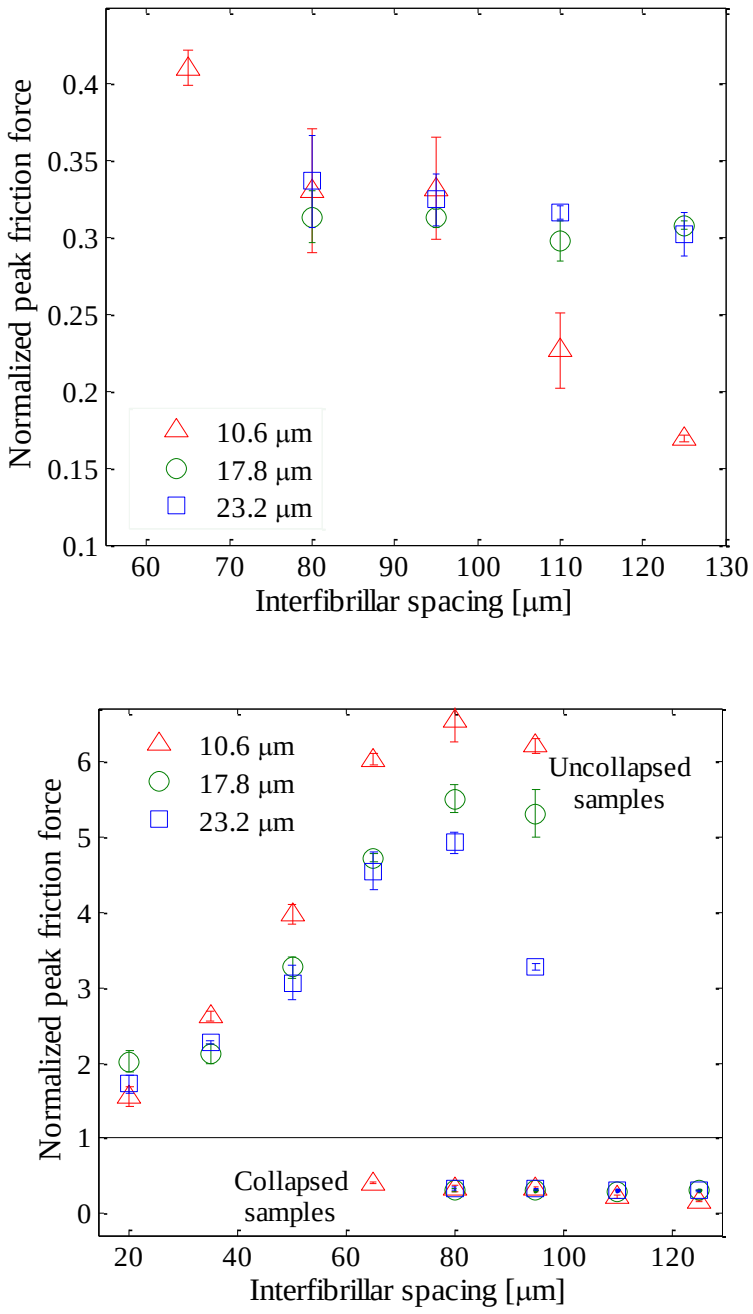


**Figure 4.6 *Top*: The peak friction force for three different fibril heights and for spacings from 20-125 μm normalized by sliding friction of the flat control. *Bottom*: Normalized maximum friction forces recorded for collapsed samples.**

For the uncollapsed FTFA studied in this work the sample *gradually* shifts to steady sliding after the static friction peak. Additionally, the shear force during sliding depends on the interfibrillar spacing as well as the fibril height. The differences in the shear response between the samples in this work and [41] are attributed to the different lengths of fibrils in the two studies. For one, in all FTFA samples, the thin film at the leading edge of the contact region buckles as the sample is displaced. For samples with shorter fibrils, the thin film makes contact with and adheres to the substrate, producing a locally collapsed region, as shown in Figure 4.7, micrograph 2.

Another, more significant difference takes place in the center of the contact region. As mentioned above, in [41] (for longer fibrils) the fibrillar layer does not support the indenter. As the sample is displaced, the fibrils do not lose contact with the indenter. Thus, we assume the sheared fibrils buckle as described in CHAPTER 1. For samples with shorter fibrils, the indenter compresses the fibrils like springs, with the greatest compression at the center of contact (see Figure 4.7, micrograph 1). The stiffened fibrils, and the thin film above them, rotate when sheared and lose contact with the indenter (Figure 4.7, micrograph 3).

For both the fibrils at the leading edge and inside the contact region, the thin film closer to the leading edge has lost contact with the indenter while the thin film behind the fibril (closer to the trailing edge) remains in contact. As the sample continues to be displaced, the detached thin film folds under the sheared fibrils, forming a crescent-shaped contact with the substrate, as shown in Figure 4.7(b).

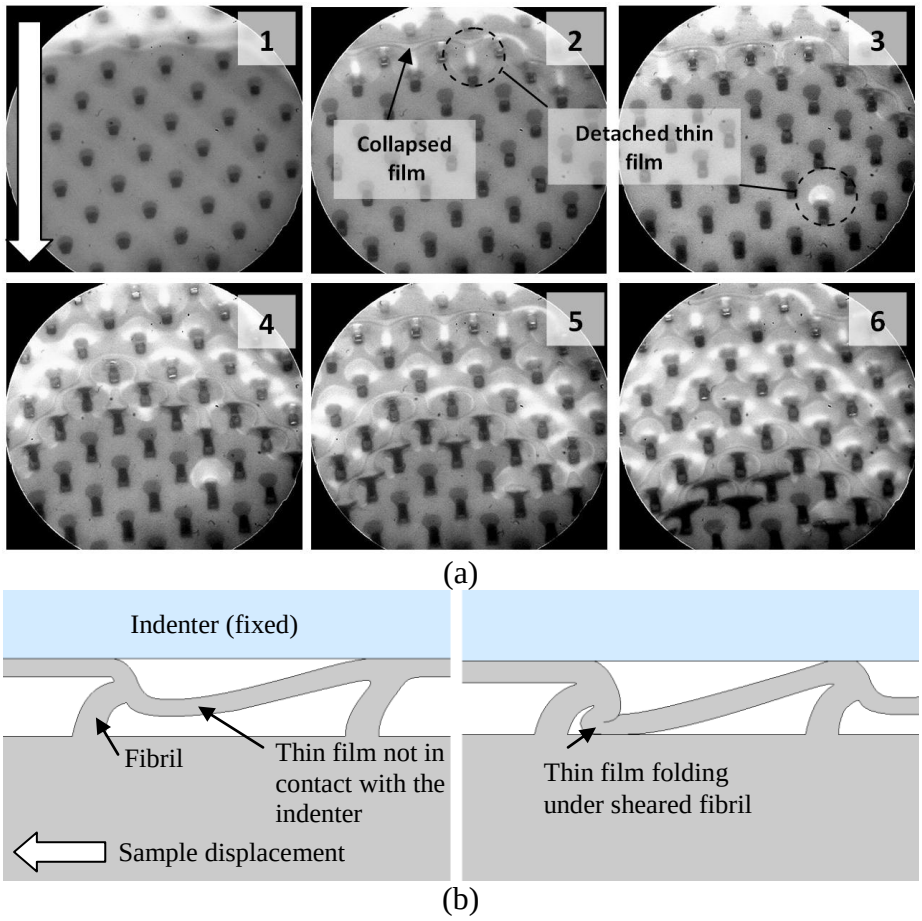


**Figure 4.7 (a) Transition from static to sliding friction in uncollapsed FTFA samples ($w_0$ = 17.8 μm). (1) Contact between the fixed indenter and sample; sample is displaced downward (in the direction of the arrow) (2) Thin film at the leading edge buckles downward into contact with the substrate. The fibrils bend and the thin film above them detaches from the indenter (as depicted in micrograph 3 and (b)). (3) Sample detaches from the indenter inside of the contact region above a compressed and sheared fibril. (4) In locations where the thin film has detached from the indenter ahead of a fibril that remains in contact, the detached thin film folds under the sheared fibril, forming a crescent-shaped contact with the substrate. This can be seen in the lower part of micrograph 6 and a schematic of this is shown in (b) as well.**

Outside of the center region and the leading edge, the contact area is reduced as the sample transitions from static to sliding friction via an instability in a manner similar to what was observed in [41].

For fibrils that partially lose contact with the indenter as described above, movement between the indenter and sample does not occur until the shear strain in the thin film behind the fibril becomes large enough to initiate an unstable release. The indenter continues to move relative to the sample in this manner.

For the collapsed samples, there is obviously no benefit from the crack-trapping mechanism, and therefore we do not find static friction enhancement. Indeed, for a sufficiently small normal load, contact between the indenter and the sample is limited to the tips of the bumps (for a large enough normal load, the indenter comes into contact with the substrate in the center of the region of contact). In Figure 4.8 it is shown that the sliding friction force of the collapsed samples is approximately one third or less than that of the flat control sample. The friction force on collapsed samples reduces monotonically with fibril density for $w_0$ = 10.6 μm while. For longer fibrils this is not the case because the bumps for these samples are much more compliant as they are typically bent or buckled underneath the thin film. Consequently, as the fibril density decreases the contact grows on each fibril. In Figure 4.11, a micrograph (and schematic) of a partially collapsed sample ($w_0$ = 17.8 μm) shows the contact between the side of the fibril and the substrate.

To support this explanation, we compare the frictional force to the area of contact and find that $F_s = \tau_f A$, where $\tau_f \approx 1.2512 \times 10^5$ kPa, which is consistent with values reported by Chateauminois and Fretigny [42]. We plot the average shear stress for each fibril height and spacing in Figure 4.9.

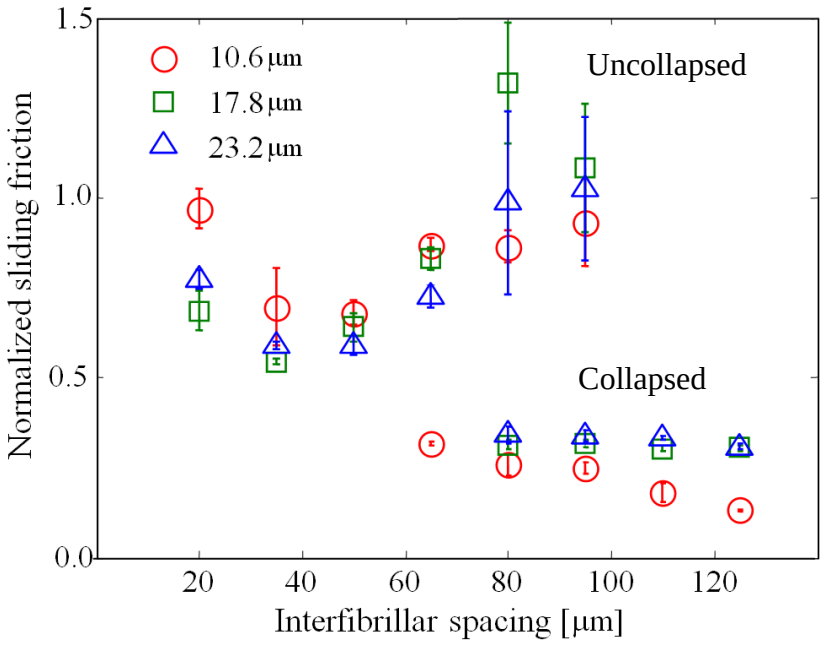


**Figure 4.8 Sliding friction results from experiments for both collapsed and uncollapsed samples. The friction force for the uncollapsed samples is dependent on spacing, unlike observations in previous friction experiments on FTFA samples with longer fibrils. This dependence is due to the indenter locally collapsing the thin film during shear; the severity of this is dependent on fibril height and interfibrillar spacing.**

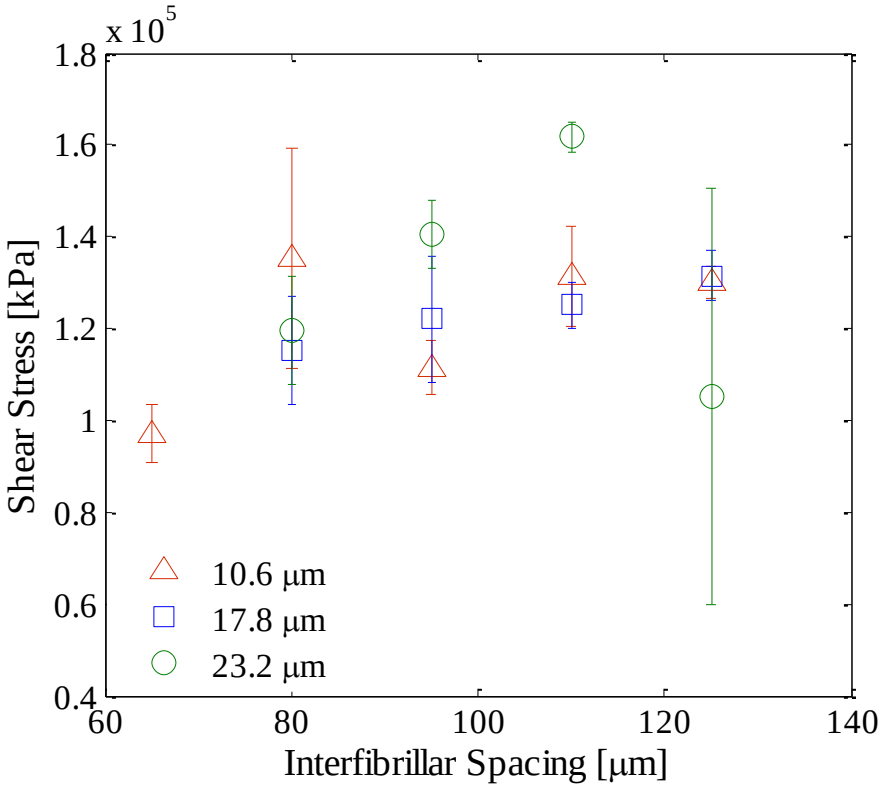


**Figure 4.9 The sliding friction is lower for *collapsed* samples, which we believe is due to reduced contact area. Here we plot the friction stress, assuming it behaves according to $F_s = \tau_f A$ [42], and find it to be approximately independent of spacing and fibril height and comparable to previously reported values for PDMS [42].**

### *4.3.3 Pressure-to-Collapse Experiments*

The pressure required to initiate and propagate collapse of the thin film onto the substrate, thereby switching a sample from the adhesive state to the non-adhesive state, was quantified using hydrostatic pressure. Samples were sealed at the edges between the thin film and substrate with PDMS to prevent water from entering the gap. They were then placed inside of a 1 m column, as illustrated in Figure 4.10, and water was supplied to a column using a peristaltic pump (Fisher Scientific Medium Flow Peristaltic Pump). The experiments were performed at two rates: $\dot{p} = 2.9$ Pa/s and $\dot{p} = 9.4$ Pa/s.

As pressure on the sample increases, the thin film between fibrils deflects towards the substrate and the fibrils begin to compress under the applied pressure. In a typical experiment, the thin film initially collapses in one location and the collapsed region propagates outward (see Figure 4.10). The initial location where the structure collapses is somewhat random and likely caused by variability in the fabrication process. For example, in the linear plate model of the thin film [64], collapse was found to be very sensitive to the film thickness, so film thickness variability could greatly influence the location of initial collapse. We refer to the pressure at which the thin film collapses somewhere on the sample as the pressure-to-collapse (PTC) and subsequently measure the area of collapsed thin film on a given sample as a function of applied pressure. In Figure 4.11, we plot the experimentally observed PTC for three fibril heights for $\dot{p} = 2.9$ Pa/s. Results are reported for interfibrillar spacings and fibril lengths that are bistable.

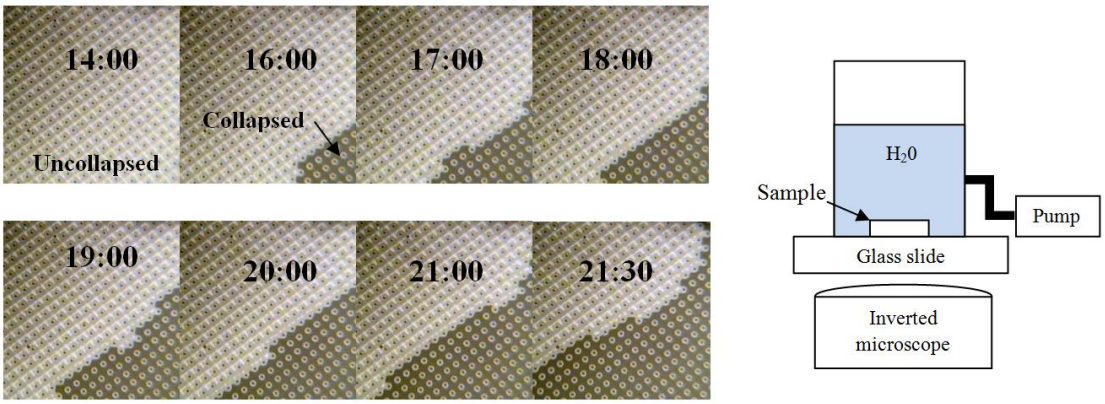


**Figure 4.10 *Left*: Micrographs from a hydrostatic pressure experiment on a 17.8 µm fibril length with a 110 µm interfibrillar spacing. The pressure on the sample increases as a function of time, which is indicated on the micrographs. Here, collapse has begun somewhere off-screen and is propagating across this region as the pressure increases. *Right*: Schematic of set-up for the hydrostatic pressure experiments. FTFA samples are sealed at the sides and placed inside of a 1m tall column. A peristaltic pump adds water to the column at a constant rate and pressure is applied by the water. The collapse of the thin film is recorded by a camera through an inverted optical microscope.**

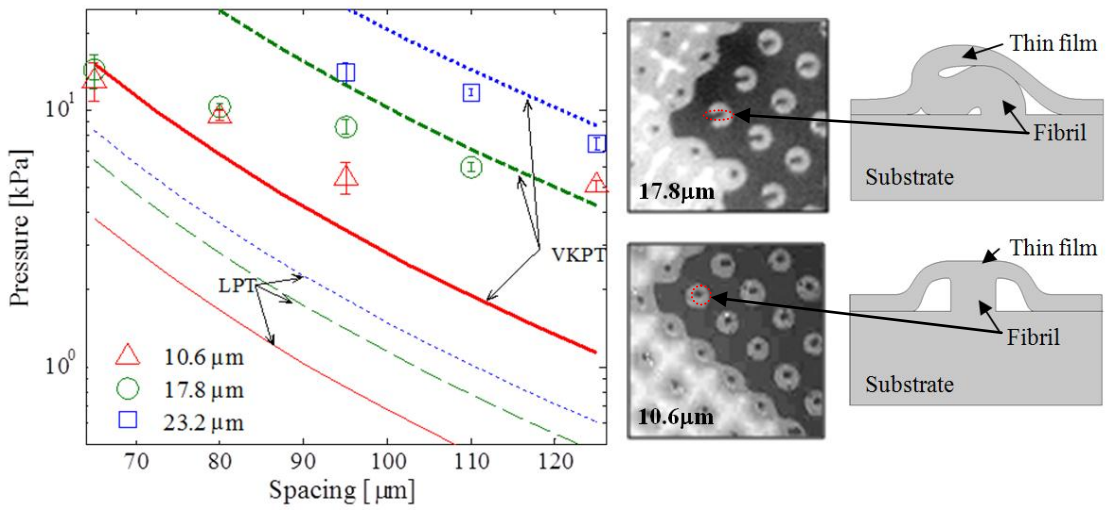


**Figure 4.11 *Left*: Experimentally observed pressure required to initiate collapse (or "pressure-to-collapse", PTC) for samples with fibril lengths of 10.6 μm, 17.8 μm, and 23.2 μm. We also show the predicted PTC from linear plate theory (LPT) and von Kärman plate theory (VKPT). The PTC decreases with increasing interfibrillar spacing in the experiments as well as in both plate theories. LPT underestimates the PTC while VKPT underestimates the PTC for $w_0$ = 10.6 μm and overestimates the PTC for the taller fibrils. For $w_0$ = 17.8 and 23.2 μm, this is due to fibril bending and/or buckling under the applied pressure, effectively reducing $w_0$. Experimental observations supporting this are shown in the micrographs and a schematic of what this looks like from the side is provided on the right. For the 10.6 μm long fibrils, the fibrils appear to be upright as the micrograph shows only the bottom of the fibril in contact with the substrate, while for the 17.8 μm long fibrils, it appears the lateral side of the fibril has come into contact with the substrate, suggesting the fibril has bent over.**

During our experiments, we observed a strong dependence, for both the PTC as well as the area of collapsed thin film, on the rate at which pressure was applied (see Figure 4.12). This rate dependence is due to the pressurization of the air inside the sealed sample as the thin film deflects and the internal volume decreases. The increase in internal pressure results in some gas components of air diffusing through the PDMS thin film into the water. To confirm the hypothesis that diffusion is reducing the pressurization inside the sealed samples, we performed the hydrostatic pressure experiment on a scaled up (sealed) sample with and without an outlet. The scaled up sample had a 78 μm circular thin film with a 1 cm diameter. The distance between the thin film and the substrate was approximately 1 mm. The hydrostatic pressure experiment was performed once with no outlet and again with an outlet (using microbore tubing) to avoid pressurization. In the latter case, we found that the PTC for the higher ( $\dot{p}$ = 9.4 Pa/s) pressure application to be 2559 Pa while for the lower ( $\dot{p}$ = 2.9 Pa/s) pressure application rate, the PTC was 2520 Pa, as shown in Figure 4.13. In comparison, the PTCs for the corresponding rates with no outlet were 8520 Pa and 6070 Pa. Additionally, for the experiment with an outlet, the contact radius between the thin film and the substrate was independent of rate and depended only on the applied pressure.

### *4.4 von-Kärman plate contact problem*

In the previous chapter, we presented a linear plate theory to obtain insight into the bistability of the FTFA. Here, we present a large-deflection adhesive contact model describing the thin-film as the sample switches from the adhesive to the non-adhesive state under an applied pressure. We also consider compression in the fibrils due to the

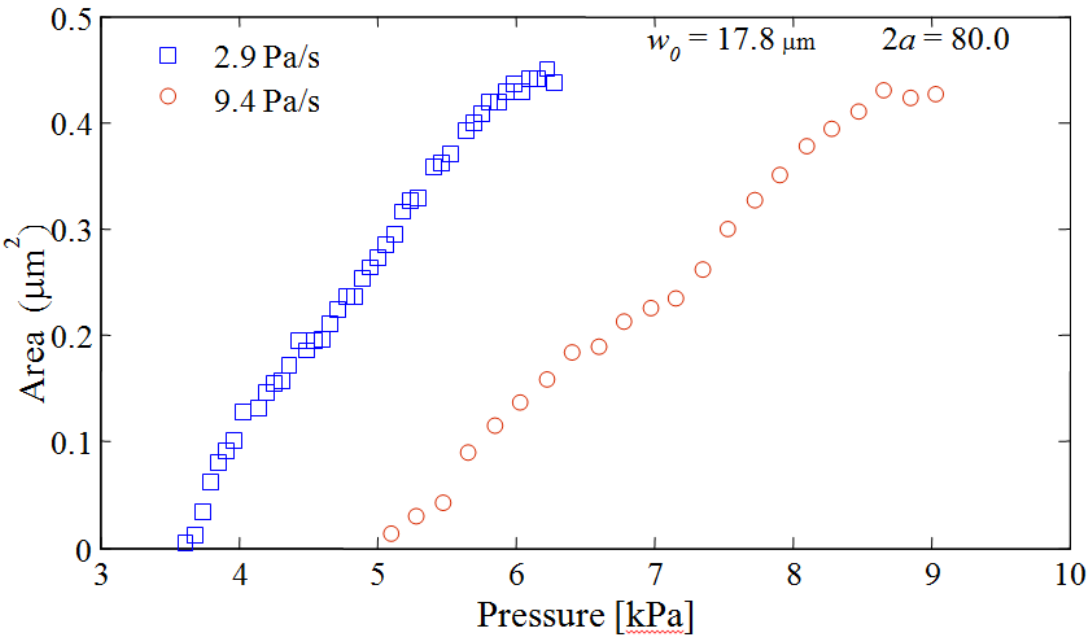


**Figure 4.12 At the higher rate (9.4 Pa/s), the sample first begins collapsing at a pressure approximately 1.5 kPa *higher* than at the lower rate (2.9 Pa/s). Once it begins collapse, the rate at which it collapses is slower as well. We found that this rate dependence was due to diffusion of the gas through the PDMS film, discussed in more detail in the next section.**

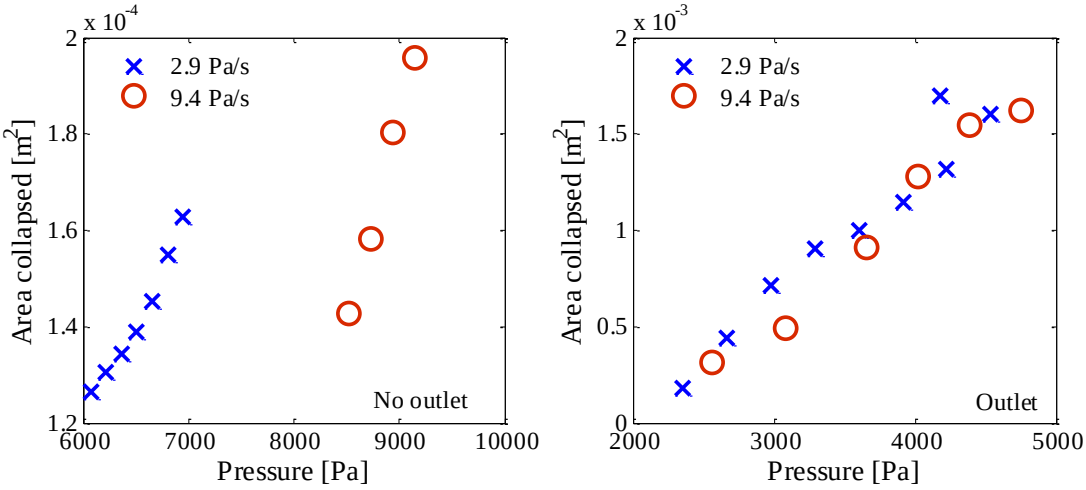


**Figure 4.13. Comparison of pressure-to-collapse for a scaled-up sample with an outlet and without an outlet. The sample was scaled up to have dimensions of $h$ = 78 μm, $2a_d$ = 1 cm, and $w_0$ = 1 mm so that a microtube outlet could be used to avoid pressurization. In the samples with no outlet, we observed the expected dependence on pressure application rate while for the samples with an outlet, both PTCs were similar and the subsequent collapse data overlapped.**

applied pressure. Finally, we model the pressurization and diffusion of air inside sealed samples that occurs during the hydrostatic pressure experiments.

In our PTC experiments, the thin film atop the fibrillar layer deforms between the fibrils until it collapses on and adheres to the substrate. As this occurs throughout the sample, we simplify the problem by looking at the deflection of the thin film between any four fibrils (fibrils are arranged in a square array). For our fibril lengths, the maximum deflection can be up to five times the thickness of the thin film. When the deflections are no longer small compared with the thickness of the plate, membrane effects which arise from stretching of the mid-plane must be considered. To include this effect, we use the well-known von Kärman plate theory. To further simplify the problem, we approximate the thin film held up by four fibrils as a clamped, circular plate whose diameter is equal to the diagonal distance between fibrils.

We describe the deformation of the plate and its subsequent contact behavior with the substrate in three stages. In the first stage, the thin film deforms freely in accordance with the von Kärman plate governing equations. In the second stage, the pressure is large enough for the plate to come into (no-slip) adhesive contact with the substrate. In the third stage, the applied pressure is reduced and the contact decreases until eventually the plate detaches from the substrate.

It should be noted that in our model, we consider the compression (or extension) of the fibrils due to the applied pressure. We assume fibrils are under uniaxial compression and do not bend or buckle, which is consistent with experimental observations for $w_0 = 10.6$ μm, though this is not always the case for longer fibrils. We

model fibrils as springs with spring constant, $k_{fibril} = EA_f / w_0$, where $A_f = 100\ \mu m^2$ is the area of the (square) cross-section of the fibrils.

We only consider diffusion when determining the PTC. While it could be extended to stages two and three of our model, in the experiments the problem is much more complicated. It is reasonable to assume the thin film deforms similarly throughout the FTFA. In the experiments, once the applied pressure is large enough, the thin film jumps into contact somewhere and the collapsed thin film propagates from that location. When collapse occurs the volume between the thin film and substrate shrinks and the internal pressure increases throughout the sample. Consequently, in stages 2 and 3 the internal pressure depends on the history of the entire sample, which we do not consider in our model.

First, we describe the experimental parameters used in our contact mechanics model, illustrated in Figure 4.14. This will be followed by a discussion of the boundary conditions and numerical methods used in each stage of this model. In this section, we do not account for the effects of pressurization and diffusion. In Section 4.4.4, we discuss the diffusion model and present results from model showing the effect of rate on the PTC.

The location of a material point on the plate is denoted by *r*. The plate has a radius $a_{d,}$ defined in the same manner as in the linear plate theory in Section 3.3.4. The vertical deflection is denoted by *w*, with a maximum deflection of $w_0$ (fibril length), and the radial displacement is denoted by *u*. Note that $w_0$ is not constant since we take into account the compression of the fibril. The applied pressure is denoted by *q*. These quantities are non-dimensionalized as follows:

$$r = a_d \eta \qquad w = \frac{h}{\sqrt{1-\nu^2}}\bar{w} \qquad u = \frac{h^2}{a_d}\bar{u} \qquad \bar{q} = \frac{q a_d^4}{4Dh} \tag{4.3}$$

Here, $\nu$ is Poisson's ratio and $E$ is the Young's modulus of the plate, $h$ is the plate thickness, and $D = Eh^3/(1-\nu^2)$ is the bending rigidity of the plate. In a similar approach to what is found in [62], we obtain the governing equations for the von Kärman plate. In von Kärman plate theory, the strains in the radial and tangential directions are [62]:

$$\varepsilon_r = \frac{du}{dr} + \frac{1}{2}\left(\frac{dw}{dr}\right)^2 \qquad \varepsilon_t = \frac{u}{r} \tag{4.4}$$

The corresponding tensile forces (per unit length) are:

$$N_r = \frac{Eh}{1-\nu^2}\left(\varepsilon_r + \nu\varepsilon_t\right) = \frac{Eh}{1-\nu^2}\left[\frac{du}{dr} + \frac{1}{2}\left(\frac{dw}{dr}\right)^2 + \nu\frac{u}{r}\right] \tag{4.5}$$

$$N_t = \frac{Eh}{1-\nu^2}\left(\varepsilon_t + \nu\varepsilon_r\right) = \frac{Eh}{1-\nu^2}\left[\frac{u}{r} + \nu\frac{du}{dr} + \frac{\nu}{2}\left(\frac{dw}{dr}\right)^2\right] \tag{4.6}$$

Using these definitions in the sum of projections in the radial direction of all forces acting on an element in the plate, we obtain:

$$\frac{d^2u}{dr^2} + \frac{1}{r}\frac{du}{dr} - \frac{u}{r^2} = -\frac{1-\nu}{2r}\left(\frac{dw}{dr}\right)^2 - \frac{dw}{dr}\frac{d^2w}{dr^2} \tag{4.7}$$

We get another equilibrium equation by applying a moment balance with respect to the axis perpendicular to the radius:

$$\begin{aligned}\frac{1}{r}\frac{d}{dr}\left(r\frac{d}{dr}\left(\frac{1}{r}\frac{d}{dr}\left(r\frac{dw}{dr}\right)\right)\right) &= \frac{1}{Dr}\frac{d}{dr}\left(rN_r\frac{dw}{dr}\right) + \frac{q}{D} \\ &= \frac{1}{D}\left[\frac{1}{r}\left(N_r + r\frac{\partial N_r}{\partial r}\right)\frac{\partial w}{\partial r} + N_r\frac{\partial^2 w}{\partial r^2} + q\right]\end{aligned} \tag{4.8}$$

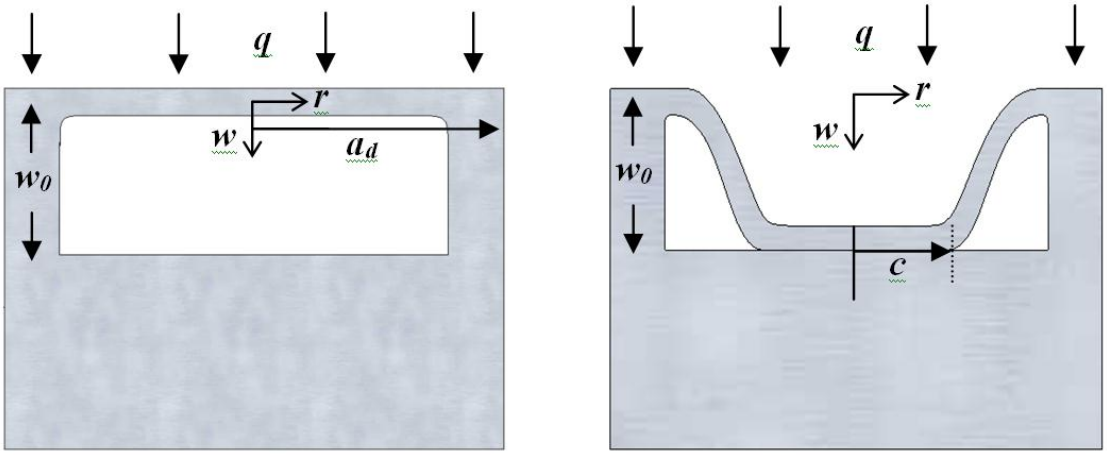


**Figure 4.14** ***Left*****: Schematic of VKPT adhesive contact mechanics model in uncollapsed state. We model the thin film between four fibrils as a circular plate whose diameter is the diagonal distance fibrils in a square array.** ***Right*****: Additional parameters for the collapsed state. The radius of contact with the substrate is denoted** ***c*****.**

We expand the LHS of (4.8) and rearrange the RHS to get:

$$\frac{d^4w}{dr^4}+\frac{1}{r^3}\left(2r^2\frac{d^3w}{dr^3}-r\frac{d^2w}{dr^2}+\frac{dw}{dr}\right)=\frac{1}{D}\left(\frac{N_r}{r}\frac{dw}{dr}+\frac{dN_r}{dr}\frac{dw}{dr}+N_r\frac{d^2w}{dr^2}\right)+\frac{q}{D} \tag{4.9}$$

Rearranging and normalizing (4.9), we obtain the following governing equations:

$$\begin{aligned}\bar{w}'''=12\bar{w}'&\left[\frac{\bar{u}'}{\eta}+\frac{1}{2\eta\left(1-\nu^2\right)}\left(\bar{w}'\right)^2+\bar{u}''+\frac{\bar{w}'\bar{w}''}{1-\nu^2}\right]\\&+12\bar{w}''\left[\bar{u}'+\frac{\left(\bar{w}'\right)^2}{2\left(1-\nu^2\right)}+\nu\frac{\bar{u}}{\eta}\right]+4\bar{q}\sqrt{1-\nu^2}-2\frac{\bar{w}'''}{\eta}+\frac{\bar{w}''}{\eta^2}-\frac{\bar{w}'}{\eta^3}\end{aligned} \tag{4.10}$$

$$\bar{u}''=-\frac{1}{\eta}\bar{u}'+\frac{\bar{u}}{\eta^2}-\frac{1-\nu}{2\eta}\left(\bar{w}'\right)^2-\bar{w}'\bar{w}'' \tag{4.11}$$

where $\bar{w}'=d\bar{w}/d\eta$. These equations describe the deformation of the plate due to the normalized applied pressure, $\bar{q}$.

*Stage 1: Non-contact deformation*

For values of $\bar{w}$ insufficient to bring the plate into contact with the substrate, the plate is freely deforming. We assume that the plate is clamped at $\eta=1$ and that, by symmetry, the radial displacement and slope are zero at $\eta$ = 0. Equations (4.10) and (4.11) are solved numerically with the following boundary conditions:

$$\begin{aligned}&\bar{w}'\left(\eta=1\right)=0 \qquad \bar{w}\left(\eta=1\right)=0 \qquad \bar{u}\left(\eta=1\right)=0\\&\bar{w}'\left(\eta=0\right)=0 \qquad \bar{u}\left(\eta=0\right)=0 \qquad \bar{w}'''\left(\eta=0\right)=0\end{aligned} \tag{4.12}$$

To solve the governing equations for these boundary conditions, we use the boundary value problem solver in MATLAB (*bvp4c*) to obtain the deformation as a function of pressure. To check our program, we compare it to Way's solution in [62] and

reproduce the loading-deflection curves for three different Poisson's ratios. The results of the VKPT in stage 1 are shown in the appendix (Section 4.6).

As mentioned earlier, we account for fibril compression due to the applied pressure. In stage 1 this is straightforward as we prescribe the pressure and can determine the change in length directly from the force on the fibril, so that the maximum deflection is $\bar{w}_0 - \bar{w}_c$, where $\bar{w}_c$ is the change in length and is calculated as,

$$\bar{w}_c = \frac{\sqrt{1-\nu^2}}{h}\frac{qA_s}{k_{fibril}} \tag{4.13}$$

*Stage 2: No-slip, adhesive contact*

At some critical pressure the plate comes into contact with the substrate. As the plate is deformed beyond the point of initial contact, the contact between the thin film and the substrate begins to grow. We assume that, once a region of the plate comes into contact with the substrate, there is no slip between the plate and the substrate. The location of the contact edge is denoted by $\eta^*$. At the outer edge of the plate, we have clamped boundary conditions:

$$\bar{w}(\eta=1)=0 \qquad \bar{w}'(\eta=1)=0 \qquad \bar{u}(\eta=1)=0 \tag{4.14}$$

At the contact edge, we have a clamped plate:

$$\bar{w}(\eta=\eta^*)=\frac{\sqrt{1-\nu^2}}{h}w_0 \qquad \bar{w}'(\eta=\eta^*)=0 \tag{4.15}$$

Again, we must determine $w_0$ as a function of the applied pressure. However, because we prescribe $\eta^*$ and $w_0$ in the *bvp4c* solver (and not $q$), this is not as

straightforward as it is in stage 1. Using (4.13), we obtain the fibril length due to compression under the applied pressure. Beginning with the contact edge location in question and assuming an uncompressed $w_0$, the applied pressure will initially predict a shorter fibril than the prescribed $w_0$. Thus, we incrementally decrease $w_0$ (for a given $\eta^*$) until the applied pressure predicts the prescribed fibril length.

Finally, the curvature, $\bar{w}''$ at $\eta^*$ is determined by the adhesion between the plate and the substrate. To model adhesion we view the process of making and breaking contact between the plate and the substrate as an external crack. In stage 2, the pressure applied to the plate increases its contact with the substrate: the crack heals and adhesion energy is released into the system. In stage 3, the pressure is reduced, the crack opens, and elastic energy is released by the system to create the new surfaces. The energy released by the elastic system per unit contact area change (as the crack advances or retreats) is called the energy release rate, $G$ and the condition for making or breaking contact is,

$$G = W_{\text{ad}}, \tag{4.16}$$

where $W_{\text{ad}}$ is the effective work of adhesion of the interface. This condition will be used as a boundary condition to determine the size of the contact zone.

The derivation of our expression for the energy release rate for detaching a von Kärman plate from a rigid substrate is based on the work of R. Long, *et al.* [67] and details, including a schematic of the geometry, are provided in Section 4.4.1. For no-slip adhesion, the potential energy released by the system, $G$, to peel off a unit area of contact is:

$$G = -\frac{EI}{2}\left(w''\right)^2 - \frac{N_r^+ \varepsilon_r^+}{2} - \varepsilon_r^- \left(\frac{N_r^-}{2} + N_r^+\right) \tag{4.17}$$

Here, *EI* is the bending rigidity of the plate, $N_r^+$ and $N_r^-$ are the radial forces immediately ahead of and behind the crack tip, respectively, and similarly, $\varepsilon_r^+$ and $\varepsilon_r^-$ are the radial strain immediately ahead of and behind the crack tip. Comparing this expression for energy release rate to the same term in linear plate theory [64], we see and additional term is due to the difference in radial strain across the crack tip. This term does not contribute to the energy release rate unless there is hysteresis in the system. In Section 4.6, we show the contact area as a function of applied pressure for the case with hysteresis using values for $W^+$ and $W^-$ for bulk PDMS from [66].

We normalize the work of adhesion as:

$$\bar{W}_{ad} = \frac{2a_d^4}{Dw_0^2} W_{ad} \tag{4.18}$$

Rearranging and normalizing (4.17) and using the relation between the in-plane radial force and radial strain, (4.17) can be re-written as:

$$\left.\frac{d^2\bar{w}}{d\eta^2}\right|_{\eta^*} = \left(\frac{w_0^2\left(1-\nu^2\right)}{h^2}\left(\bar{W}_{ad} - \frac{12a^2}{w_0^2}\underbrace{\left(\bar{u}_+' - \bar{u}_-'\right)}_{=0}\left[\bar{u}_+' - \bar{u}_-' + \nu\bar{u}\right]\right)\right)^{\frac{1}{2}} = \frac{w_0}{h}\sqrt{\left(1-\nu^2\right)\bar{W}_{ad}} \tag{4.19}$$

Note that as long as contact is growing, the radial strain is continuous across the contact edge, so $\bar{u}_+' = \bar{u}_-'$. We once again use Matlab's *bvp4c* solver to obtain the deflection and the stretch of the plate as the pressure and contact area increase. To

check our results, we compare them with the analytical solution from linear plate theory in the small deflection regime $W_{ad} = 0$. This is included in Section 4.6.

*Stage 3: Detachment*

Finally, to determine bistability, we examine the evolution of contact as the applied pressure is reduced. To solve for the location of the contact edge, we note that in general, contact remains pinned at $\eta^*$ until the following condition is satisfied:

$$\bar{G} = \frac{h^2}{w_0^2\left(1-\nu^2\right)}\left(\frac{d^2\bar{w}}{d\eta^2}\right)^2 + \frac{12a^2}{w_0^2}\left(\bar{u}'_+ - \bar{u}'_-\right)\left(\bar{u}'_+ - \bar{u}'_- + \nu\bar{u}\right) = \bar{W}_{ad} \tag{4.20}$$

Crack pinning occurs in systems with interfacial hysteresis because the free-standing thin film can stretch independently of the adhered thin film and, due to the no-slip condition, the $\bar{u}'_+ - \bar{u}'_-$ is no longer zero. As the pressure is reduced, the energy release rate, *G*, at the crack tip increases. When Equation (4.16) is satisfied, the crack advances and the contact area is reduced until, eventually, the plate detaches from the substrate. The boundary conditions once again assume clamped conditions at the edge of the plate:

$$\bar{w}'\left(\eta = 1\right) = 0 \qquad \bar{w}\left(\eta = 1\right) = 0 \tag{4.21}$$

At the contact edge, the boundary conditions are:

$$\bar{w}'\left(\eta = \eta^*\right) = 0 \qquad \bar{w}\left(\eta = \eta^*\right) = \frac{\sqrt{1-\nu^2}}{h} w_0 \tag{4.22}$$

We assume the $W_{ad}$ is the same in loading and unloading, so that the strain will remain continuous across the contact edge during unloading. If the system does exhibit hysteresis, this is not the case. For a given $W_{ad,}$ we use the *bvp4c* solver to determine the deformation as a function of the reducing pressure. As we do so, we evaluate the energy release rate and allow the crack to propagate when it equals the work of adhesion.

### *4.4.1 Energy release rate*

We assume perfect bonding (no slip inside the contact zone) between the plate and the substrate. In Figure 4.15, a schematic of the reduction of the contact is shown as an infinitesimal area initially in contact with the substrate, *da* ('part 2' in Figure 4.15), detaches from the substrate. The plate outside of the original contact region is called part 1. Then the external work required to detach a unit area of contact, *da*, is:

$$2\pi a\left[M_r\underbrace{\left(-w''da\right)}_{-d\theta}+N_r^+(\varepsilon_r^- -\varepsilon_r^+)da-Q_r dw\right] \tag{4.23}$$

Here, $M_r = EIw''$ is the radial moment and $Q_r$ is the shear force, both at the contact edge, *c*. $N_r^+$ represents the radial force to the right of the contact edge (in tension) and $\varepsilon_r^+$ and $\varepsilon_r^-$ represent the radial strain to the right and the left of *c*, the normalized contact edge, respectively. These quantities are related to the displacements by:

$$\varepsilon_r^+ = u'\left(r=c^+\right)+\frac{1}{2}\left(w'\left(r=c\right)\right)^2 = u'\left(r=c^+\right),\quad w'\left(r=c\right)=0 \tag{4.24}$$

$$\varepsilon_r^- = u'\left(r=c^-\right)+\frac{1}{2}\left(w'\left(r=c\right)\right)^2 = u'\left(r=c^-\right),\quad w'\left(r=c\right)=0 \tag{4.25}$$

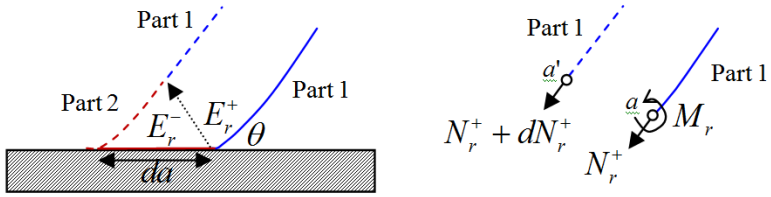


**Figure 4.15** ***Left*: The change in geometry during an infinitesimal shrinkage in contact line, *da*. The position of the edge of contact is located at the left hand side of part 1, which represents the plate not in contact with the substrate before detachment. Strain immediately to the left and right of the contact edge is denoted. Dashed lines indicate the shape of the plate after detachment. *Right*: Line tension and moments acting on part 1 before and after detachment at the contact edge.**

Similarly,

$$N_r = \frac{Eh}{1-\nu^2}\left(u' + \nu\frac{u}{r} + \frac{1}{2}\left(w'\right)^2\right) = \frac{Eh}{1-\nu^2}\left(u' + \nu\frac{u}{r}\right) \tag{4.26}$$

Consequently,

$$N_r^+ = \frac{Eh}{1-\nu^2}\left(u'\left(c^+\right) + \frac{\nu}{c}u\left(c\right)\right) \tag{4.27}$$

$$N_r^- = \frac{Eh}{1-\nu^2}\left(u'\left(c^-\right) + \frac{\nu}{c}u\left(c\right)\right)$$

Since $Q_r dw \approx O\left(da\right)^2$, this reduces the work to move $da$ to $da'$ to:

$$2\pi a da\left[EI\left(w''\right)^2 + N_r^+(\varepsilon_r^- - \varepsilon_r^+)\right] \tag{4.28}$$

The change in strain energy in part 2 is:

$$2\pi a da\left[\frac{EI\left(w''\right)^2}{2} + \frac{N_r^+\varepsilon_r^+ - N_r^-\varepsilon_r^-}{2}\right] \tag{4.29}$$

Therefore, the total change in potential energy $\Gamma$ is:

$$\begin{aligned} d\Gamma &= 2\pi a da\left[\frac{EI}{2}\left(w''\right)^2 + \frac{N_r^+\varepsilon_r^+ - N_r^-\varepsilon_r^-}{2} - EI\left(w''\right)^2{}_r - N_r^+(\varepsilon_r^+ - \varepsilon_r^-)\right] \\ &= 2\pi a da\left[-\frac{EI}{2}\left(w''\right)^2 - \frac{N_r^+\varepsilon_r^+}{2} - \varepsilon_r^-\left(\frac{N_r^-}{2} + N_r^+\right)\right] \end{aligned} \tag{4.30}$$

Finally, we get for the energy release rate:

$$G_{no-slip} = \frac{-d\Gamma}{2\pi a da} = -\frac{EI}{2}\left(w''\right)^2 - \frac{N_r^+ \varepsilon_r^+}{2} - \varepsilon_r^- \left(\frac{N_r^-}{2} + N_r^+\right) \tag{4.31}$$

### *4.4.2 $W_{ad}$ as a fitting parameter*

Typically in the pressure experiments, we apply hydrostatic pressure to the FTFA and measure the PTC and the collapsed area as the pressure is further increased. For sample geometries that do not lie on the cusp of bistability, the collapsed region does not return to the uncollapsed state when the pressure is reduced to zero. However, the contact area of the thin film in contact between any four fibrils does shrink as the pressure is reduced (see Figure 4.16). To estimate the $W_{ad}$, we use $W_{ad}$ to fit the contact radius predicted by the adhesive contact mechanics model to the experimental contact radius as a function of pressure. We use data from two samples, one with $w_0$ = 23.2 μm and $2a$ = 80 μm and the second with $w_0$ = 10.6 μm and $2a$ = 65 μm (shown in Figure 4.16). From these, we estimate a value for $W_{ad}$ = 0.3 J/m$^2$ that fits for both samples.

### *4.4.3 Bistability*

As shown in Figure 4.17 for $w_0$ = 10.6 μm, samples with $2a$ = 65 μm and greater, the contact mechanics model requires a negative applied pressure to reduce the normalized contact area from 0.5 to 0. As with LPT, these samples are termed bistable as a negative force is required to remove the thin film from its equilibrium state in

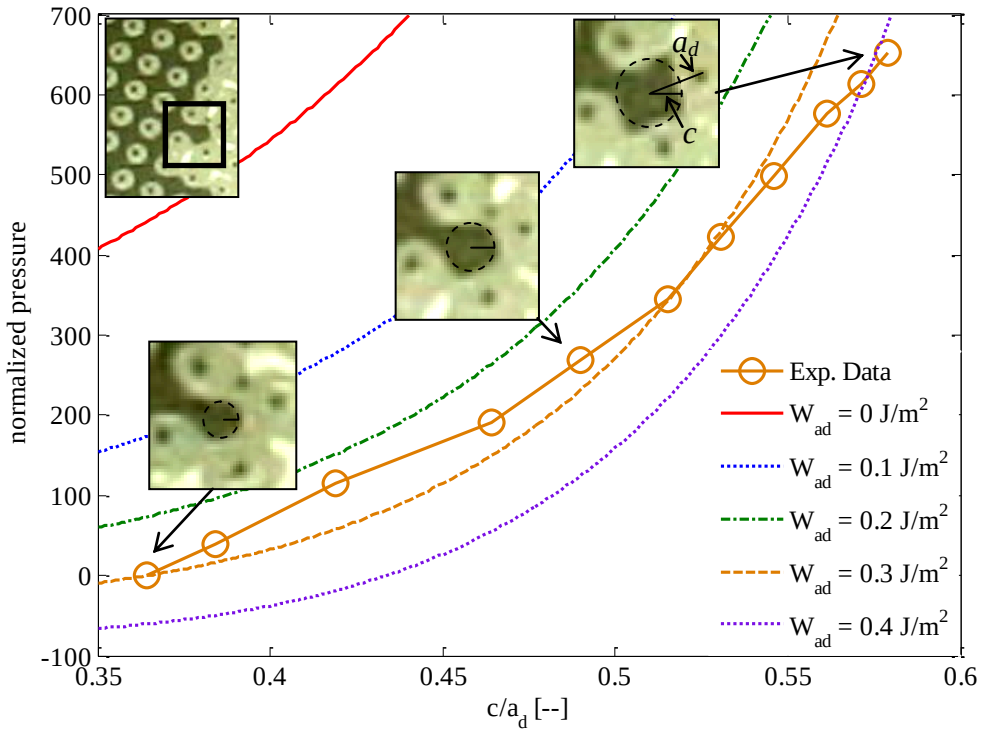


**Figure 4.16 To find a value to use for $W_{ad}$ in the VKPT contact mechanics model, we use $W_{ad}$ as a fitting parameter to fit VKPT to the experimental data. For a sample with $w_0$ = 10.6 μm and $2a$ = 65 μm, the experimental values for the contact radius as applied pressure is reduced were measured. This data is given by the orange line with circles. The lines without symbols show the contact radius as a function of reducing pressure for different $W_{ad}$. As is shown, the best fit was obtained for $W_{ad}$ = 0.3 J/m$^2$.**

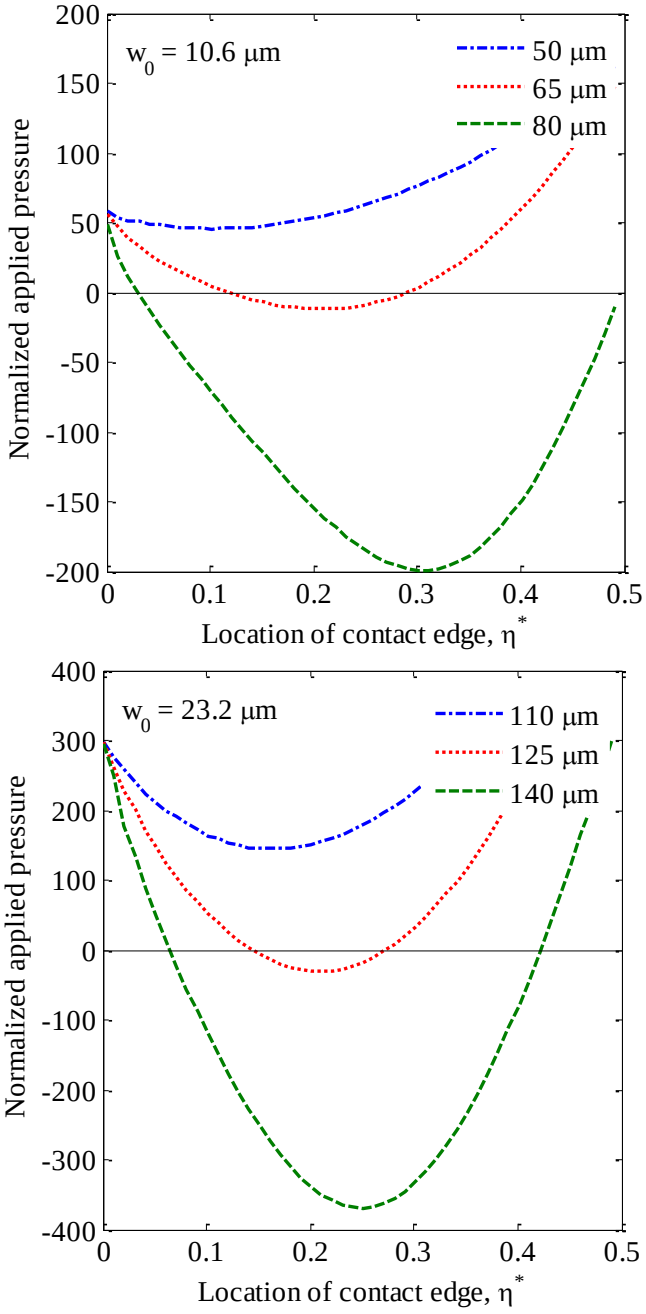


**Figure 4.17 Results for contact radius as a function of pressure from the VKPT contact mechanics model for $W_{ad}$ = 0.3 J/m$^2$. These figures do not incorporate pressurization and diffusion of the gas sealed in the samples (discussed in the next section), but does account for the compression in the fibrils.**

contact with the substrate. For $w_0$ = 23.2 μm, the model does not predict that any of the interfibrillar spacings used in our experiments will be bistable.

For all three fibril heights, VKPT overpredicts the interfibrillar spacing required for bistability compared to what is observed experimentally, particularly for longer fibrils. This is in part because we do not account for bent or buckled fibrils, which was experimentally observed for $w_0$ = 17.8 μm and $w_0$ = 23.2 μm. In Figure 4.11, we show micrographs of collapsed samples with short and intermediate fibril lengths; in the latter case, buckling is observable.

In Figure 4.18 we plot the geometries for which VKPT predicts bistability. We also plot bistability predicted using LPT for comparison. VKPT is more conservative than LPT because it accounts for the membrane forces in the plate as deflection becomes large relative to the plate thickness. It predicts more accurately the nonlinear dependence bistability has on interfibrillar spacing, although linear plate theory is more successful for shorter fibril lengths. For longer fibrils, it appears VKPT would be more suitable.

### *4.4.4 Pressure-collapse -- Diffusion*

As mentioned previously, the experimentally observed PTC is dependent on the rate at which the hydrostatic pressure is applied. In our hydrostatic pressure experiments, we increase the pressure on the sample at one of two constant rates $\dot{p}$ = 9.4 Pa/s, and $\dot{p}$ = 2.9 Pa/s. The difference between the applied external pressure and the pressure of the sealed gas inside the sample, $\Delta p = p_{\text{external}} - p_{\text{internal}}$ gives us the pressure on the thin film discussed in section 4.4. We assume that the thin film deflects in a similar manner

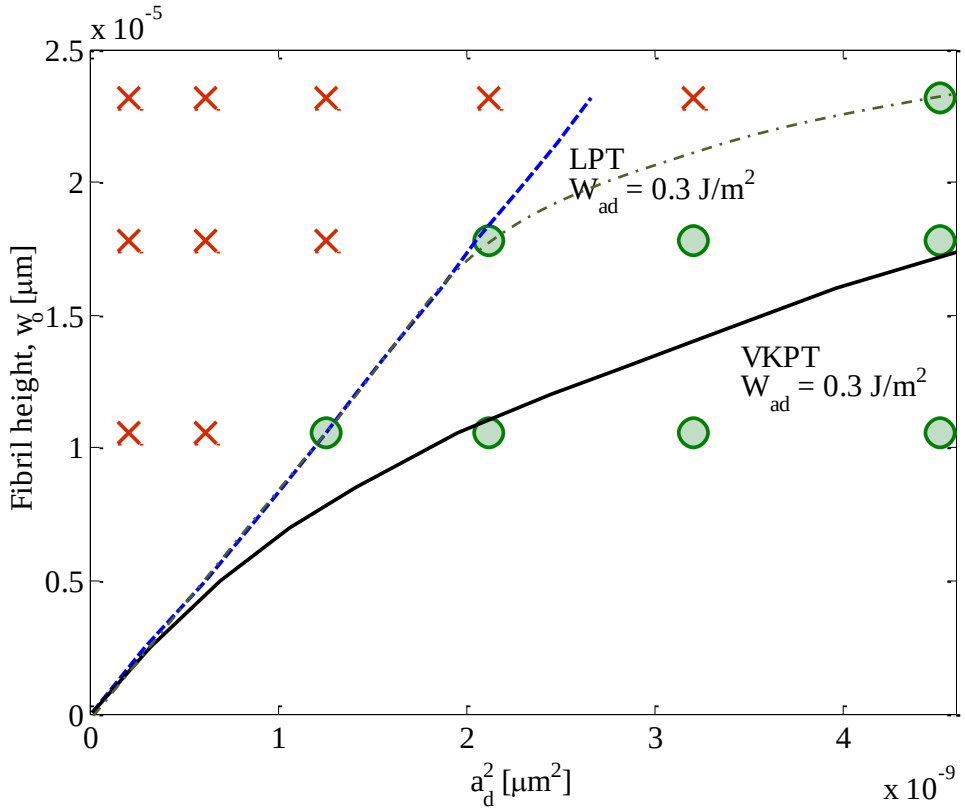


**Figure 4.18 Phase diagram indicating fibril heights and interfibrillar spacings for which FTFA samples possess both the adhesive and non-adhesive stable states. FTFA samples that, from experimental observation, *are* bistable are denoted with 'o' symbols while samples that *are not* bistable are denoted with 'x'. The '– - –' dashed green line follows the experimental data as a guide to the eye. The VKPT model predicts geometries (fibril heights and spacings) on and to the right of the solid black line are bistable while LPT predicts geometries on and to the right of the dashed blue line are bistable.**

between any four fibrils throughout the sample. Additionally, we assume that the air inside the sample is an ideal gas. With these assumptions, we can model the pressurization and diffusion of gas by looking at a unit cell of four fibrils.

The pressurization inside the sample increases the chemical potential of the gas inside the sample, resulting in the diffusion of gases through the thin film. If the thin film were impermeable, the pressure inside of the sealed sample would increase, reducing the pressure difference across the thin film. For example, for samples with $w_0$ = 17.8 μm the VKPT predicts the PTC to be 5 to 6 times larger than if diffusion does not occur, as shown in Figure 4.19 and compared to experimental data.

Due to the rate dependence, it is not possible to assign a unique value for the PTC. Approximately representing the composition of the air as 79% $N_2$ and 21% $O_2$, we utilize Fick's first law of diffusion to estimate the diffusion of different gas species, *i*, out of the sample.

$$J_i = -\frac{D_i}{RT}\frac{\mu_i^{ex} - \mu_i^{in}}{h}c_i \tag{4.32}$$

where $D_i$ is the diffusivity of a gas species in PDMS; for $N_2$ and $O_2$ in PDMS, $D_{N_2} = D_{O_2} = 3.4\times10^{-9}$ m$^2$/s [68]. $R$ is the ideal gas constant (8.314 JK$^{-1}$mol$^{-1}$), $T$ is room temperature (296 K). $c_i$ is the molar concentration ($= n_i/V$ mol m$^{-3}$, $n_i$ is the number of moles of gas *i* and $V$ is the total volume that the gas occupies, which will decrease as the thin film is depressed by the hydrostatic pressure). $\mu_i^{ex}$ and $\mu_i^{in}$ are the values of the chemical potential of the gases outside of the sample (in the water) and inside the space between the thin film and the substrate, respectively.

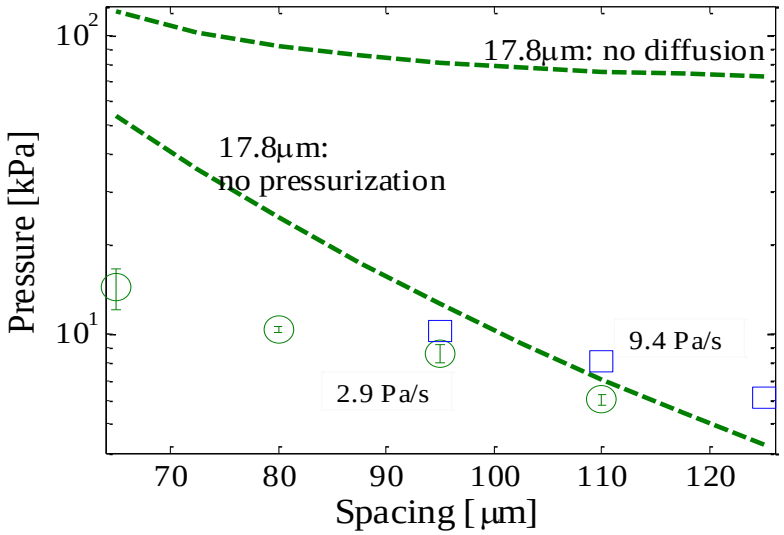


**Figure 4.19 In this figure we compare the PTC predicted by the VKPT model for a sample with no diffusion (full pressurization) as well as no pressurization and compare these results to the experimental data for PTC at the two different pressure application rates, 2.9 Pa/s and 9.4 Pa/s, indicated by the symbols. As is shown here (and as was observed experimentally), pressurization inside the sample can have a large impact on the PTC.**

Assuming an isothermal process, the chemical potential of the gases inside the sample as the gas is compressed is given by:

$$J_i = -\frac{D_i}{RT}\frac{\mu_i^{ex} - \mu_i^{in}}{h}c_i \tag{4.33}$$

$\mu_i^0$ is the chemical potential of pure species *i* in the reference state. $P_i^C$ is the partial pressure of component *i* of the compressed gas and $P^0$ is the pressure in the reference state. Thus, for each gas species, we get the following expressions for the chemical potential as the gas compresses:

$$\mu_{O_2}^{in} = \mu_{O_2}^0 + RT\ln\left(\frac{P_{O_2}^C}{P^0}\right) \qquad \mu_{N_2}^{in} = \mu_{N_2}^0 + RT\ln\left(\frac{P_{N_2}^C}{P^0}\right) \tag{4.34}$$

For the chemical potential of air above the thin film (in water), we can assume that because the air above the water and the water are in equilibrium, the chemical potential of the air in the water is the same as the chemical potential of the air above the water. The increase in the chemical potential due to the hydrostatic pressure is negligible; e.g., Enns, *et al*. [69] showed that for an aqueous solution in equilibrium with atmospheric air, hydrostatic pressurization on the partial pressure of dissolved gases increases it approximately 1.4% for every 1 MPa increase in external pressure. Therefore, the chemical potential of the gas in the water above the sample is:

$$\mu_{O_2}^{ex} = \mu_{O_2}^0 + RT\ln\left(\frac{P_{O_2}^{H_2O}}{P^0}\right) \qquad \mu_{N_2}^{ex} = \mu_{N_2}^0 + RT\ln\left(\frac{P_{N_2}^{H_2O}}{P^0}\right) \tag{4.35}$$

where $P_i^{H_2O}$ is the partial pressure of gas component *i* in $H_2O$ and is equal to $\chi_i P_{atm}$, where $\chi_i$ is the molar fraction of species *i* in air. The difference between the chemical potential of the air in the water and the compressed gas inside of the sample is obtained by subtracting equation (4.34) from equation (4.35):

$$\Delta\mu_i = \mu_i^{ex} - \mu_i^{in} = RT\ln\left(\frac{P_i^{H_2O}}{P_i^C}\right) = RT\ln\left(\frac{\chi_i P_{atm}}{\chi_i P^C}\right) = RT\ln\left(\frac{P_{atm}}{P^C}\right) \tag{4.36}$$

As shown in equation (4.36), the $\Delta\mu$'s for $N_2$ and $O_2$ are equal as the molar fractions cancel out. Along with the equivalent diffusivities of both gases, we can use equation (4.17) to re-write our expression for the molar flux as:

$$J = J_{N_2} + J_{O_2} = -\frac{D}{RT}\frac{\Delta\mu}{h}\left(c_{N_2} + c_{O_2}\right) = -\frac{D}{RTh}\frac{n}{V_c}\Delta\mu \tag{4.37}$$

where *n* is the total number of moles ($n = n_{O_2} + n_{N_2}$). Using equation (4.37) the molar amount of gas component *i* diffused through the membrane per unit time $n_f$ is:

$$n_f = -\frac{DA_p}{RTh}\frac{n}{V_c}\Delta\mu \tag{4.38}$$

where $A_p$ is the projected surface area of the deformed thin film. Accounting for the reduced molar amount inside the sample, the internal pressure is now:

$$P_i = \frac{\left(n - n_f\right)RT}{V_c} \tag{4.39}$$

By accounting for the pressurization and diffusion, we are able to use the VKPT contact mechanics model to determine more accurately the actual pressure on the thin film in VKPT.

As shown in Figure 4.20, the faster the rate at which pressure is applied, the higher the predicted PTC. Because of the log-term in (4.36), diffusion occurs more rapidly for larger pressure differences. As a result, for larger spacings (for which the PTC is much lower), the duration over which diffusion takes place is shorter. This means the effect of pressurization is much more pronounced for larger spacings. Conversely, for smaller spacings, the duration of time over which the thin film deforms to the point of contact with the substrate is much longer. For a long enough duration, the diffusion can negate the effects of pressurization. In summary, pressurization reduces the effect of interfibrillar spacing on PTC. With this accounted for, the VKPT more accurately models the dependence of PTC on interfibrillar spacing.

### *4.5 Summary*

In this chapter, we characterize the adhesive and shear response of a switchable FTFA as well as develop a VKPT adhesive contact mechanics model to describe the behavior of the thin film as the sample switches between adhesive and non-adhesive states. The VKPT model more accurately describes the pressure required to collapse the thin film than linear plate theory and describes bistability more accurately for longer fibrils.

We observed rate dependence in the hydrostatic pressure experiments when determining the pressure required to collapse the thin film. We confirmed that the gas inside the sealed samples pressurizes during these experiments and that the rate at which gas diffuses out of the sample determines both the pressure required to initiate

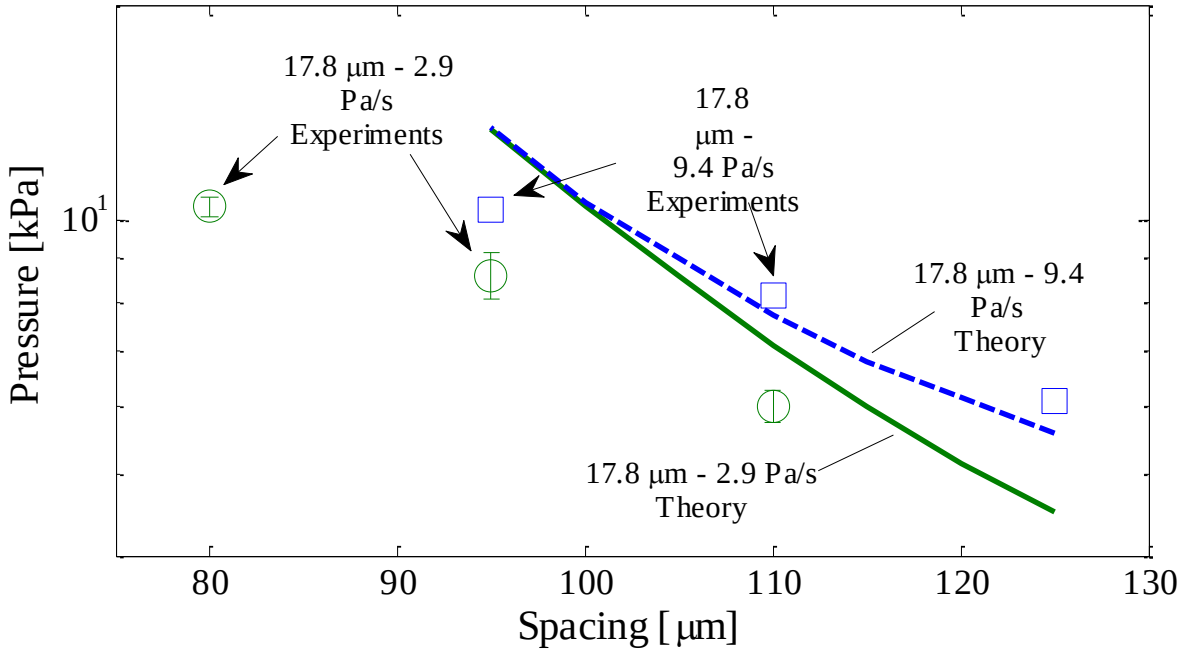


**Figure 4.20 Predicted PTC from the VKPT model accounting for pressurization and diffusion in our samples for $w_0$ = 17.8 μm. The results from the model are compared with experimental results, denoted by the symbols. For lower loading rates, diffusion reduces more of the pressurization, and the PTC approaches the theoretical PTC for samples with no pressurization.**

collapse as well as the rate at which collapse propagates through the sample. By incorporating diffusion into VKPT model, we show that the rate at which pressure is applied affects the PTC and reduces the dependence of PTC on interfibrillar spacing. Taking this into account, the model is more consistent with what is observed experimentally.

## *4.6 Appendix*

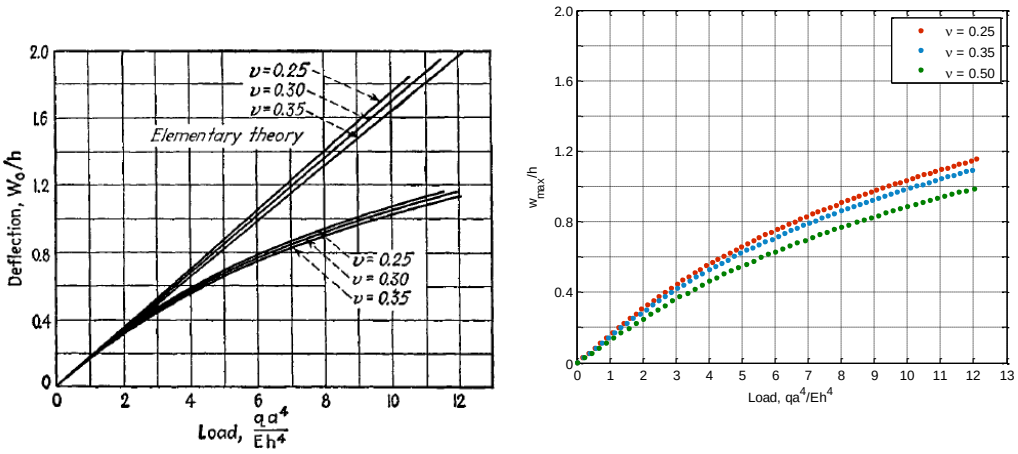


**Figure 4.21 von Kärman plate theory for Stage 1 for three Poisson's ratios. Way's solution from [62] is included on the left. Results from *bvp4c* included on the right.**

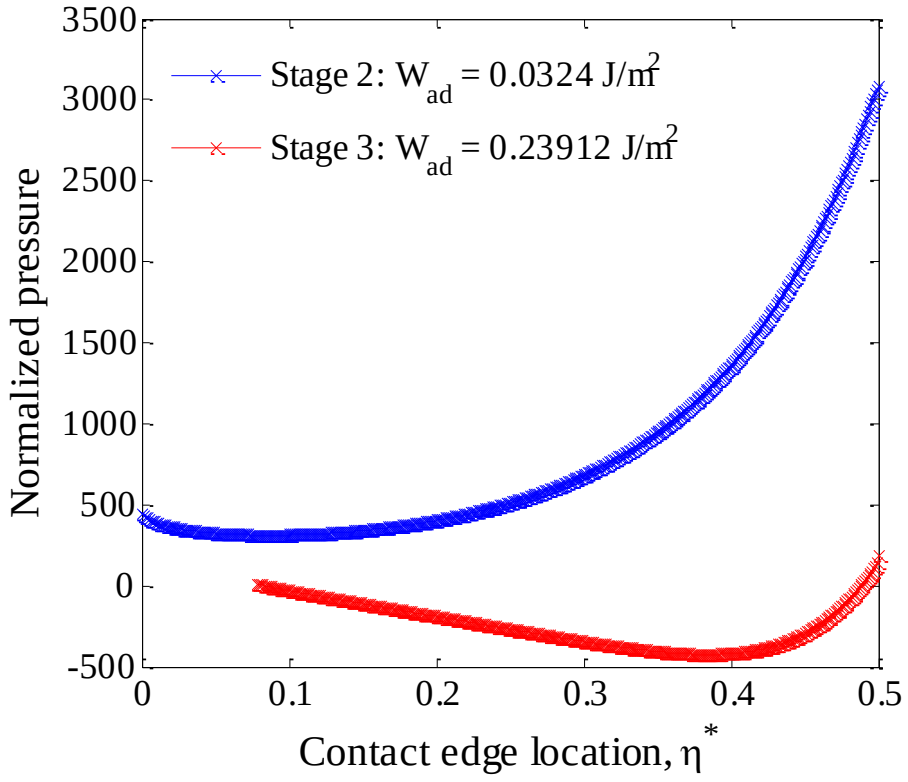


**Figure 4.22 Results for $w_0$ = 17.8 μm, $a_d$ = 110 μm with hysteresis ($W_{ad}$ in Stage 2 not equal to $W_{ad}$ in Stage 3).**

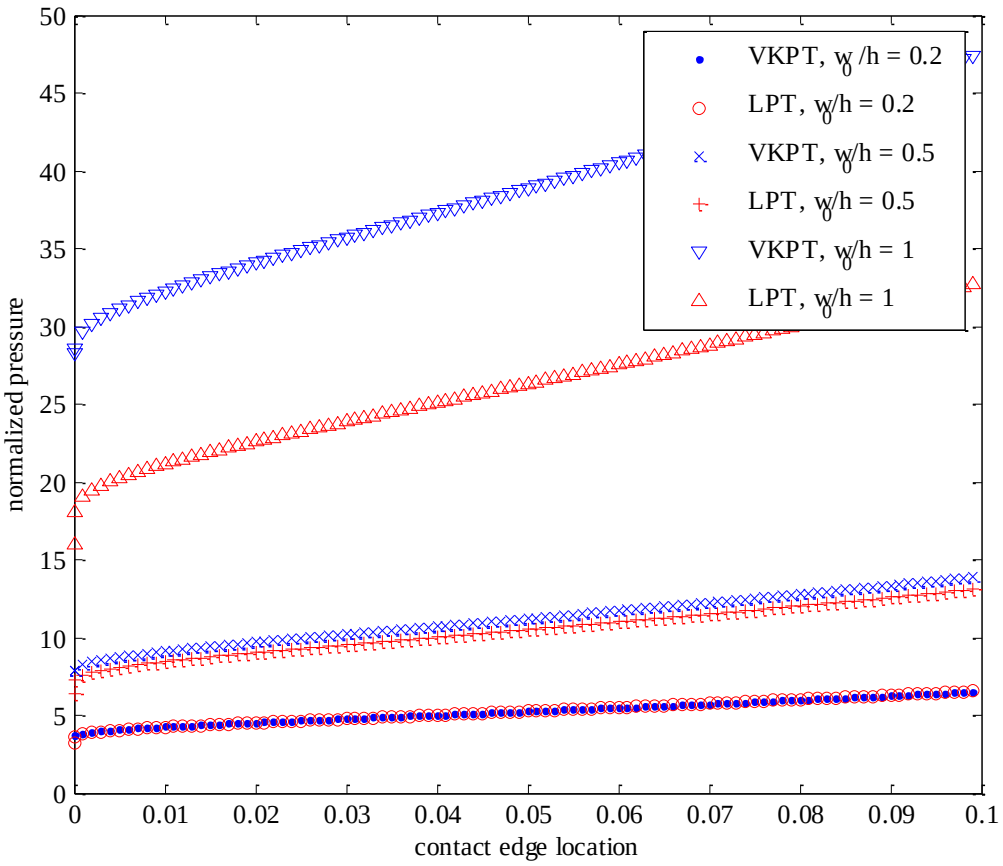


**Figure 4.23 Comparison of LPT and VKPT in stage 2 for different $w_0/h$; $W_{ad}$ = 0.**

# CHAPTER 5

*Summary and Future work*

## 5.1 Summary of Present Work

The most important contributions of the present dissertation are the development, characterization, and analysis of a switchable bioinspired adhesive. The original development and findings of the present investigation include:

1. The use of a dynamic rod model and stability analysis to define and analyze buckling of a fibril subjected to a prescribed shear displacement and a constant normal compressive force.
2. For a friction experiment with a flat indenter, assuming that the fibrils in an array are identical and the number of fibrils in contact with the indenter is constant, some findings from this analysis include:

    a. If the applied compressive $F_n$ on each fibril is less than $\pi^2 EI/L^2$ then static friction should decrease with increasing normal load.

    b. If the applied compressive $F_n$ on each fibril is greater than $\pi^2 EI/L^2$, then the friction force becomes negative if adhesion is weak resulting in the violation of shear constraint.

    c. The shear force on a fibril decreases with normal load (for $F_n > -\pi^2 EI / L^2$) suggesting that static friction should also decrease

with normal force as long as the boundary constraints on the fibrils are maintained.

3. We develop a film-terminated fibrillar interface with two metastable states. In the first state, a thin film spanning a fibrillar surface results in strongly enhanced adhesion due to crack-trapping. In the second state, the thin film collapses onto the substrate between fibrils and resembles a rough surface.
4. Indentation experiments (pull-off and adhesion hysteresis) demonstrate differences in the adhesive response of the two states. We show that the adhesive state has a pull-off load up to 70 times higher than the non-adhesive state and has up to 20 times larger adhesion hysteresis.
5. Friction experiments demonstrate the differences in the two states in shear. In the uncollapsed state there is a gradual transition from static to sliding friction. Sliding friction on the non-adhesive state is a quarter to a third of the control as contact is limited by the bumpy surface.
6. We determined the pressure-to-collapse the surface in order to switch from the adhesive to the non-adhesive state using hydrostatic pressure experiments.
7. To understand the behavior of the thin film in the film-terminated fibrillar architecture, we presented two models representing the thin film between four posts as a circular plate clamped at the edge.
    a. In CHAPTER 3 we first develop a linear plate theory that identifies a dimensionless combination of materials and geometrical parameters including $W_{ad}$, $w_0$, $h$, $E$, and $a$, such that bistability is possible only

when this parameter is sufficiently large. We find that the model captures the experimental findings reasonably well.

b. As we are dealing with large deflections, in CHAPTER 4 we present a von Kärman plate adhesive contact mechanics model. We find that it more accurately captures the pressure required to initiate collapse of the thin film onto the substrate. It also is better at describing the nonlinear dependence of bistability on $w_0$ as interfibrillar spacing grows.

c. We model the rate dependence in the hydrostatic pressure experiments using Fick's law. We see that the pressurization and diffusion of gas through the thin film of the sample reduces the dependence on interfibrillar spacing.

## 5.2 Suggestions for Future Work

### *5.2.1 Theoretical Work*

The models presented to describe the switching mechanism could be improved upon. While von Kärman plate theory captures the large deflections experienced by the thin film, it would be important to look at models that can account for the membrane behaviors, particularly for longer fibrils.

We modeled the thin film between four fibrils as a plate clamped at the edge in order to simplify the model. However, as the thin film can deflect in the experiments between the fibrils, this boundary condition may be too strict. A model with more realistic boundary conditions might suggest a lower PTC.

Also, modeling the PTC as well as bistability would be aided by accounting for the bending or buckling of longer fibrils during collapse.

### *5.2.2 Practical Applications*

While there are several methods that can be used to switch the adhesive between the highly adhesive and non-adhesive states, including displacing the thin film manually and changing the pressure on the thin film from either above or below, developing a device in which the switching can be done while in contact with another surface would be very useful. With this set-up, the switchable adhesive would have a great deal of uses, including in robots, as a micromanipulator, and more. Additionally, the switchable adhesive presents a possible route to self-cleaning. Based on the qualitative behavior of the test in Figure 3.4, if the surface is dirtied in the adhesive state and then switched into the non-adhesive state, cleaning the surface would be much easier (assuming the foulants are not smaller than the distance between bumps).

REFERENCES


[1] Ruibal, R., and Ernst, V. *J Morphol* 117 (1965): 271-294.

[2] Autumn, K., Liang, Y.A., Hsieh, S.T., Zesch, W., Chan, W.P., Kenny, T.W., Fearing, R., and Full, R.J. *Nature* 405 (2000).

[3] Hiller, U.J. *J. Bombay Nat. Hist. Soc.* 73 (1975): 278-282.

[4] Huber, G., Mantz, H., Spolenak, R., Mecke, K., Jacobs, K., Gorb, S.N., and Arzt, E. *PNAS USA* 102 (2005): 16293-16296.

[5] Jagota, A., and Hui, C.-Y. *Material Science and Engineering: R: Reports* 72.12 (2011): 253–292.

[6] Greiner, C., del Campo, A., and Arzt, E. *Langmuir* (2007): 495-502.

[7] Glassmaker, N.J., Jagota, A., Hui, C.Y., and Kim, J. *J R Soc Interface* (2004).

[8] Northen, M. and Turner, K. *Nanotechnology* 16 (2005): 1159-1166.

[9] Glassmaker, N.J., Jagota, A., Hui, C.-Y., Noderer, W.L., and Chaudhury, M.K. *Proc Natl Acad Sci U S A.* 104.26 (2007): 10786-91.

[10] Peressadko, A., and Gorb, S.N. *J Adhes* 80 (2004): 247-261.

[11] Ge, L., Sethi, S., Ci, L., Ajayan, P.M., and Dhinojwala, A. *PNAS* (2007): 10792-10795.

[12] Gorb, S., Varenberg, M., Peressadko, A., Tuma, J. *J R Soc Interface* (2006).

[13] Kim, S., and Sitti, M. *Appl Phys Lett* 89 (2006).

[14] Noderer, W.L., Shen, L., Vajpayee, S., Glassmaker, N.J., Jagota, A., and Hui, C.-Y. *Proc Royal Soc A* 463 (2007): 2631-2654.

[15] Autumn, K., Buehler, M., Cutkosky, M., Fearing, R., Full, R.J., Goldman, D., Groff, R., Provancher, W., Rizzi, A.E., Saranli, U., Saunders, A., and Koditscheck, D. Proc. SPIE. 5804.291 (2005).

[16] Pain, S. *New Science* 168.62 (2000).

[17] Decuzzi, P. and Srolovitz, D.J. *J. Microelectromech. Syst.* 13.377 (2004).

[18] Chung, S.T., Ucar, A.B., Swindlehurst, G.R., Bradley IV, R.O., Renk, F.J., and Velev, O.D. *Adv. Mater.* 21 (2009): 2807-2813.

[19] Chuang, Y.-J., Tseng, F.-G., Cheng, J.-H., and Lin, W.-K. *Sensors and Actuators* 103 (2003): 64-69.

[20] Murphy, M.P., Aksak, B., and Sitti, M. *Small* 5 (2008): 170-175.

[21] Menon, D. Sameoto and C. *Smart Mater. Struct.* 19 (2010): 103001.

[22] Krahn, J., Sameoto, D., and Menon, C. *Smart. Mater. Struct* 20 (2011): 015014-015022.

[23] Northen, M.T., Greiner, C., Arzt, E., and Turner, K.L. *Adv. Mater.* 20 (2008): 3905-3909.

[24] Reddy, S., Arzt, E., and del Campo, A. *Adv. Mater* 19 (2007): 3833-3837.

[25] Kim, S., Sitti, M., Xie, T., and Xiao, X. *Soft Matter* 5 (2009): 3689-3693.

[26] Kim, T.-I., Pang, C., and Suh, K.Y. *Langmuir* (2009).

[27] Jeong, H.E., Kwak, M.K., and Suh, K.Y. *Langmuir* 26.4 (2010): 2223–2226.

[28] Lin, P.-C., Vajpayee, S., Jagota, A., Hui, C.-Y., and Yang, S. *Soft Matter* 4 (2008): 1830-1835.

[29] Paretkar, D., Kamperman, M., Schneider, A.S., Martina, D., Creton, C., and Arzt, E. *Mater. Sci. Eng: C* 31 (2011): 1152-1159.

[30] Aksak, B., Sitti, M. Casell, A., Li, J., Meyyappan, M., and Callen, P. *Appl Phys Lett* 91 (2007).

[31] del Campo, A., Greiner, C., and Arzt, E. *Langmuir* 23.20 (2007): 10235-10243.

[32] Parsaiyana, H., Barazandeha, S., Rezaeia, M., Parsaiyanb, M., and Safdaria, M. *Int. J. Adhes. Adhes.* 29 (2009): 444-450.

[33] Schubert, C., Majidi, C., Groff, R.E.,Baek, S., Bush, B., Maboudian, R., and Fearing, R.S. *J. Adhes. Sci. Tech.* 21.12-13 (2007): 1297-1315.

[34] Bhushan, B. and Sayer, R.A. *Microsystem Technologies* 13 (2007): 71-78.

[35] Gravish, N., Wilkinson, M., Spongberg, S., Parness, A., Esparza, N., Soto, D., Yamaguchi, T., Broide, M., Cutkosky, M., Creton, C., and Autumn, K. *J R Soc Interface* (2009).

[36] Kim, S., Aksak, B., and Sitti, M. *Appl. Phys. Lett.* 91 (2007).

[37] Majidi, C., Groff, R.E., Maeno, Y., Schubert, B., Baek, S., Bush, B., Maboudian, R., Gravish, N. Wilkinson, M., Autumn, K. and Fearing R.S. *Phys. Rev. Lett.* 97 (2006).

[38] Murphy, M.P, Kim, S., and Sitti, M. *Appl. Mater. Interfaces.*(2009).

[39] Vajpayee, S., Long, R., Shen, L., Jagota, A., and Hui, C.-Y. *Langmuir* 25 (2009): 2765-2771.

[40] Varenberg, M. and Gorb, S. *J R Soc Interface* (2007).

[41] Shen, L., Jagota, A., Hui, C.-Y. *Langmuir* 25.5 (2009): 2772-2780.

[42] Chateauminois, A. and Fretigny, C. *Eur Phys J E* 27 (2008): 221-227.

[43] Yao, H., Rocca, G.D., Guduru, P.R., and Gao, H. *J R Soc Interface* (2007).

[44] Zhao, B., Pesika, N., Rosenberg, K., Tian, Y., Zeng, H., McGuiggan, P., Autumn, K., and Israelachvili, J. *Langmuir* 24 (2008): 1517-1524.

[45] Autumn, K., Dittmore, A., Santos, D., Spenko, D., and Cutkosky, M. *The J. Exp. Biol.* 209 (2006): 3569-3579.

[46] Hui, C.-Y., Jagota, A., Shen, L., Rajan, A., Glassmaker, N., and Tang, T. *J. Adhes. Sci. Tech.* 21.12-13 (2007): 1259-1280.

[47] Glassmaker, N.J., Jagota, A., Hui, C.Y., and Kim, J. *J R Soc Interface* (2004).

[48] Liu, J., Hui, C.-Y., and Jagota, A. *Polym Sci Pol Phys* 47.23 (2009): 2368-2384.

[49] Goyal, S., Perkins, N.C., and Lee, C.L. *J. Comp. Phys.* 209 (2005): 371-389.

[50] Keller, H.B. New York : Academic Press, 1971.

[51] Shen, L., Glassmaker, N.J., Jagota, A., and Hui, C.-Y. *Soft Matter* 4 (2008): 618-625.

[52] Nadermann, N., Kumar, A., Goyal, S., and Hui, C.-Y. *J R Soc Interface* (2010).

[53] Kumar, A., and Healey, T.J. Computer Methods in Applied Mechanics and Engineering (2010).

[54] Alling, H.J. *Geology* 51.4 (1943): 259-269.

[55] Crosby, A.J., Hageman, M., and Duncan, A. *Langmuir* 21 (2005): 11738-11743.

[56] Matthew, A., Zhul, Z.T., Kumar, V., Lee, K.J., Feng, X., Huang, Y.Y., Adesida, I., Nuzzo, R.G., and Rogers, J.A. *Nat. Mat.* 5 (2006): 33-38.

[57] Long, R., Hui, C.-Y., Kim, S., and Sitti, M. *J. of Appl. Phys.* 104 (2008): 44301-44309.

[58] Liu, J., Hui, C.-Y., Jagota, A., and Shen, L. *J. of Appl. Phys.* (2009).

[59] Vajpayee, S., Jagota, A., Hui, C.-Y. *J. Adhesion* 86.1 (2010): 39-61.

[60] Wan, K.-T. *J Appl Mech* 76.5 (2009).

[61] Julien, S.E., Wan, K.-T. *J Appl Mech* 76.5 (2009).

[62] Woinowsky-Krieger, S. Timoshenko and S. *Theory of Plates and Shells*. Mcgraw-Hill College, 1959.

[63] Liu, J. *PhD Dissertation*. Cornell University, 2009.

[64] Nadermann, N., Ning, J., Jagota, A. and Hui, C.-Y. *Langmuir* 26.19 (2010): 15464-15471.

[65] Schargott, M., Popov, V.L., and Gorb, S. "Spring model of biological attachment pads." *J Theor Biol* 243.1 (2006): 48-53.

[66] Vajpayee, S., Hui, C.-Y., and Jagota, A. *Langmuir* 24.17 (2008): 9401-9409.

[67] Long, R., Shull, K.R., and C.-Y. Hui. *J Mech Phys Solids.* 58 (2010): 1225-1242.

[68] Merkel, T.C., Bondar, V.I., Nagai, K., Freeman, B.D., and Pinnau, I. *J Polym Sci Pol Phys*. 38 (2000): 415-434

[69] Enns, T., Scholander, P.F., and Bradstreet, F.D. *J Phys Chem.* 69 (1965): 389-391.